VULNERABILITY ASSESSMENT OF POWER TRANSFORMERS AND POWER SYSTEMS TO GEOMAGNETIC DISTURBANCES

MOHAMADREZA ARIANNIK

A DISSERTATION SUBMITTED TO
THE FACULTY OF GRADUATE STUDIES
IN PARTIAL FULFILLMENT OF THE REQUIREMENTS
FOR THE DEGREE OF
DOCTOR OF PHILOSOPHY

GRADUATE PROGRAM IN ELECTRICAL
ENGINEERING AND COMPUTER SCIENCE
YORK UNIVERSITY
TORONTO, ONTARIO

November 2022

Abstract

Powerful solar storms emit plasma that may travel towards the earth. Interactions between the plasma and the earth magnetic field cause geomagnetic disturbances (GMDs), which in turn induce quasi-dc voltage along long conductors in power systems. Assessing the power system resiliency against GMDs requires accurately calculating the induced electric fields and the resultant geomagnetically induced currents (GICs). Offline and online wide-area geomagnetic field monitoring systems are established in this research to estimate GIC flows in power systems accurately.

The proposed monitoring systems process the magnetic field signals that are measured at several observatories worldwide. In the offline monitoring system, the magnetic field signals are denoised, and spikes are detected and replaced. The time derivative of the signal is taken by a continuous wavelet transform to prevent amplification of the noises. GICs in a modified IEEE 118-bus benchmark power system are calculated concerning a realistic geomagnetic storm to demonstrate the effectiveness of the proposed signal processing methods. A sliding window is applied in the online monitoring system, and its size is optimized to lower processing time while increasing the signal-to-noise ratio.

High amplitude GICs can cause a sharp increase in the hottest-spot temperature of the power transformers. The high temperature allows the formation of gaseous bubbles in the oil-paper insulation and endangers the integrity of the transformer's insulation system. The bubbles include mainly water vapor and emerge in the cavities on the surface of the paper insulation. In the experimental phase of this research, a test setup is created to detect bubbling inception temperature (BIT) for Kraft and thermally upgraded papers (TUPs). The paper samples are dried, prepared at six different moisture levels, and immersed in synthetic ester oil for the experiments. The paper strips are wound around a cartridge heater, and a controller unit raises its temperature at 3 ºC/min and 20 ºC/min rates to detect BIT. The BITs are considered the operational limit on the hottest-spot temperature of the transformers.

To my mother Marzieh

Acknowledgement

I would like to sincerely thank my supervisor Prof. Afshin Rezaei-Zare for his continuous support and guidance throughout my Ph.D. program. His advice on the roadmap of my research and how to overcome obstacles through engaging, inspiring, and interesting discussions significantly helped me in achieving tangible results.

I would like to express my gratitude to my supervisory committee, Prof. Hany Farag and Prof. John Lam. I appreciate their thoughtful comments during my qualifying and oral examination. I would like to extend my gratitude to my internal and external examiners Prof. Paul G. O'Brien and Prof. Mona Ghassemi for their constructive feedbacks.

I wish to show appreciation to Prof. Peter Werle, who hosted me at Schering Institute at Leibniz University Hannover for four months. I am incredibly grateful for letting me access the laboratory equipment and providing me with all the required materials for the oil-paper insulation experiments. I also thank my colleagues at the institute and Moritz Kuhnke as the co-author of one of my papers as a result of the collaboration.

I want to acknowledge the financial support from Mitacs Globalink and the Faculty of Graduate Studies at York University for supporting my research stay in Germany.

Another pleasure for me at York University was to work alongside my sincere colleagues and friends Milad Akbari, Iman Babaei-Yazdi, and Babak Ahmadzadeh. Lastly, I thank my mother for her unconditional love, believing in me my entire life, and encouraging me to be ambitious and not to believe in my limits.

Table of Contents

Abstract ii

Dedication iv

Acknowledgement v

Table of Contents vii

List of Tables x

List of Figures xii

List of Acronyms xvi

Chapter 1 Introduction 1

1.1 Solar Activities 1

1.2 Monitoring GMDs on Earth's Surface 2

1.3 Effects of GMDs on Electrical Power Systems 3

1.4 History of Critical GMD Events 4

1.5 Road Map and Novel Contributions 5

1.6 Organization of the Dissertation 7

Chapter 2 Processing Magnetometer Signals for Accurate Wide-Area Geomagnetic Disturbance Monitoring 9

2.1 Introduction 9
2.2 Noise Reduction and Spike Elimination 11
2.2.1 Denoising B Signals 12
2.2.2 Despiking B Signals 14
2.2.2.1 Median Filtering 14
2.2.2.2 Replacement at Peak of Differences (RPD) 15
2.2.2.3 Wavelet Decomposition Method 17
2.3 Time-Frequency Analysis of Magnetic Field Signals 20
2.3.1 A Review on Time-Frequency Analysis Methods 22
2.3.2 Investigating Time-Frequency Decompositions 25
2.3.2.1 Frequency Components of dBx/dt Signal 26
2.3.2.2 Frequency Components of Bx Signal 31
2.3.3 Extracting Frequency Components from Filtered $\boldsymbol{Bx}$ Signal 33
2.4 Taking Derivative of *B* signal 36
2.4.1 A Discussion on the Sampling Frequency 41
2.5 Results 45
2.6 Conclusion 50
Chapter 3 Online Monitoring of Magnetometer Signals for Estimating Induced Electric Fields in Power Systems 51
3.1 INTRODUCTION 51
3.2 Denoising Magnetic Field Signals 53
3.2.1 Properties of Wavelet Denoising Method 55
3.3 Derivative of Magnetic Field Signals 57
3.3.1 Induced Electric Field 61
3.4 Updating Historical Data Points 62

3.5 Processing Speed 68

3.6 Conclusion 69

Chapter 4 Bubble Formation in Oil-Paper Insulation of Power Transformers 71

4.1 INTRODUCTION 71

4.2 Fundamentals of Bubble Formation 74

4.3 Experimental Test Setup 77

4.3.1 Moisture in Paper Insulations 80

4.4 Results and Observations 84

4.4.1 BIT in Kraft Paper 84

4.4.2 BIT in Upgraded Papers 86

4.5 Discussion 88

4.5.1 Kraft Paper 88

4.5.2 Upgraded Papers 90

4.6 Bubble Generation at High Temperate Rise Rates 92

4.7 Conclusion 96

Chapter 5 Summary and Future Directions 97

5.1 Summary 97

5.2 Future Directions 98

References 100

List of Tables

Table 2-1: Denoising effect on Bx signal and its derivative. 13

Table 2-2: Evaluating effect of the scale parameter on dBx/dt signal; DPA values are in percent. 39

Table 2-3: Correlation coefficients between the main and modified signals. 40

Table 2-4: Effect of sampling frequency on preserving peaks of dy/dt............. 44

Table 2-5: Effect of the scale parameter on preserving peaks of dy/dt. 45

Table 3-1: Denoising the Bx signal recorded at Yellowknife station. 57

Table 3-2: Evaluating changes in the SNR due to an increased window width. . 58

Table 3-3: A comparison among SNR of unprocessed, online processed and offline processed magnetic field signals. 61

Table 3-4: Comparing wavelet denoising and moving average filter. 69

Table 4-1: Interfacial Tension (IFT) for New and Aged Oils [91]......................... 76

Table 4-2: Properties of Midel 7131 [94] oil compared with requirements in IEC 61099 [96]... 78

Table 4-3: Moisture absorption by Kraft paper and TUP from air. 85

Table 4-4: Comparing bubbling in Kraft paper and TUP at a 20 ºC/min TRR. 94

List of Figures

Figure 1-1: Map of geomagnetic field observatory stations [16]. 3

Figure 1-2: Steps in analyzing a GMD event. 7

Figure 2-1: Spikes in the Bx signal recorded at Fort Churchill station; (a) Bx signal; (b) zoomed view on a spike; (c) spikes in dBx/dt signal......................... 15

Figure 2-2: Difference signal $D = Bx - Bx$, obtained by RPD method. 16

Figure 2-3: Comparing median filtering and RPD methods in smoothing a spike in the signal recorded at Fort Churchill station on 2015/08/15. 18

Figure 2-4: Despiking using RPD method; (a) Bx signal; vertical lines indicate the missed spikes; (b) dBx/dt; ovals surround the missed spikes. 19

Figure 2-5: Spikes in the detail coefficients of SWT of Bx signal recorded at Fort Churchill station; ovals show spikes that are not detected by RPD method. 21

Figure 2-6: Five resistivity zones of Ontario [35].. 22

Figure 2-7: Amplitude of earth's transfer functions for Ontario [35]. 23

Figure 2-8: Magnetic field signal recorded at Ottawa observatory on 1989/03/13; (a) Bx signal; (b) dBx/dt signal. 27

Figure 2-9: Time-frequency analysis of the Bx signal recorded on 1989/03/13; (a) CWT scalogram; (b) STFT spectrogram; (c) SPWV distribution. 28

Figure 2-10: Instantaneous frequency of dBx/dt during March 13-14, 1989. 29

Figure 2-11: Instantaneous frequency of denoised dBx/dt during March 13-14, 1989; (a) unmodified frequencies (b) despiked frequencies. 30

Figure 2-12: Despiked frequency ridge of the modified Bx signal recorded during March 13-14, 1989. 32

Figure 2-13: $x(t)$ versus its instantaneous frequencies. 34

Figure 2-14: Filtered Bx signal versus its modified instantaneous frequencies during March 13-14, 1989. 35

Figure 2-15: dBx/dt signal versus instantaneous frequencies of the filtered Bx during peak of the GMD event on March 13 and 14, 1989. 36

Figure 2-16: Effect of the scale parameter on smoothing dBx/dt. 41

Figure 2-17: Performance of the proposed signal processing method on the time derivative of Bx signal recorded at Yellowknife station. 42

Figure 2-18: Electric field components calculated for Yellowknife station; (a) Ex; (b) Ey. 47

Figure 2-19: Wide-area GIC calculation algorithm. 48

Figure 2-20: GIC amplitude on bus 24 associated with the Yellowknife B data. . 49

Figure 3-1: Original and denoised Bx signal recorded at Yellowknife station. 59

Figure 3-2: Progressive reduction of noises in dBx/dt due to denoising and applying WBD method. 62

Figure 3-3: Schematic of GIC flows in a power system during a GMD event. 63

Figure 3-4: Improvement in quality of the induced electric field data due to denoising B signal and choosing WBD over FDM in calculating dB/dt. 64

Figure 3-5: Updating and replacing previously processed data points. 65

Figure 3-6: Variations in SNR of dBx/dt due to updating previously processed data points. 66

Figure 3-7: Improvements in the induced electric field signal due to: (a) online processing (b) updating historical data points. 67

Figure 4-1: A schematic of a three-phase transformer 72

Figure 4-2: Internal pressure $Pint$ inside a bubble; (a) $r = 0.1\ mm$, (b) $r = 0.5\ mm$. 77

Figure 4-3: Cartridge heater. 79

Figure 4-4: Cartridge heater with test and sample papers. 80

Figure 4-5: Glass vessel with the cartridge heater immersed in the oil. 81

Figure 4-6: Schematic of the test setup. 81

Figure 4-7: Control unit box. 82

Figure 4-8: A paper sample on the scale. 83

Figure 4-9: Increase in the moisture content of the paper insulations. 84

Figure 4-10: BITs for Kraft paper. 86

Figure 4-11: BIT for TUP, aramid paper, and Kraft paper ($N2$ saturated). 87

Figure 4-12: Bubbles in junction areas of Kraft paper insulation. 89

Figure 4-13: Bubble accumulation on Kraft paper. 90

Figure 4-14: Comparing CBGT for TUP with BIT for Kraft paper and TUP; the data pertain to the experimental results from this research. 93

Figure 4-15: Bubble generation in Kraft paper and TUP at 20 ºC/min; (a) Kraft paper at 133 ºC, (b) TUP at 133 ºC, (c) kraft paper at 177 ºC, (d) TUP at 177 ºC. 95

List of Acronyms

B

BIT bubbling inception temperature ... 73

C

CBGT continuous bubbling generation temperature ... 92

CIM Complex image method ... 20

CME coronal mass ejections ... 1

CWT continuous wavelet transform ... 23

D

DL decomposition level ... 56

DP Degree of polymerization ... 99

DPA deviation in the peaks' amplitude ... 39

DWT Discrete wavelet transform ... 18

F

FDM finite difference methods ... 57

FIR finite impulse response ... 33

G

GIC geomagnetically induced current ... 3

GMD geomagnetic disturbances ... 2

GPS global positioning system ... 2

H

HST hottest-spot temperature ... 72

I

IFT interfacial tension 75

IIR infinite impulse response......... 13

N

NCC Normalized correlation coefficient.................................. 39

R

RPD Replacement at Peak of Differences............................... 15

S

SPWV smoothed pseudo-Wigner-Ville 25

STFT short time Fourier transform 23

SWT stationary wavelet transform 20

T

TRR temperature rise rate 92

TUP thermally upgraded paper 73

W

WBD wavelet-based derivative 59

WDM wavelet decomposition method 20

WVD Wigner-Ville distribution 25

WW window width......................... 56

Chapter 1

Introduction

1.1 Solar Activities

Solar coronal holes and coronal mass ejections (CME) cause the most powerful eruptions on the sun's surface [1]. CME releases clouds of high energy plasma from the Sun's corona. In case the CME faces earth, the plasma can travel to earth in 14.6 hours based on the historical records of solar flares [2]. However, the delay for the plasma to reach earth is distinct for different solar flares.

High amplitude currents flow at a height of approximately 100 km above earth's surface that are known as auroral and equatorial electrojets [3, 4]. Geomagnetic storms cause a chain of processes within magnetosphere, ionosphere, and thermosphere regions, which leads to formation of an either positive or negative ionospheric storms [5]. As a result, amplitude of the currents flowing in auroral ionosphere increases significantly. Moreover, center of the eastward electrojet moves equatorward [6]. The change in the intensity and direction of the electrojets are dominated by both ionospheric disturbance dynamo and penetration of plasma that is erupted from the Sun [7]. The reader may refer to [8-12] for a detailed discussion on the dynamics of electrojets during solar storms.

The auroral electrojet causes fluctuations in earth's magnetic field [13]. This time-varying magnetic field induces an electric field on earth's surface. It comes as no surprise that the changes in earth's magnetic field as well as the induced electric field affect equipment that are relying on either of these two fields. Satellites including global positioning system (GPS), power systems, gas and oil pipelines, and railway systems [14] are among equipment affected by geomagnetic disturbances (GMD). However, this research focuses on effects of GMDs on power systems.

1.2 Monitoring GMDs on Earth's Surface

Solar flares and changes in intensity of the auroral electrojets can be detected by measuring magnetic field on earth's surface [15]. There are several observatory stations span over different regions of earth that are equipped with magnetometers. Intermagnet [16] is one of the observatory networks that constitutes international groups who collaborate on promoting magnetic measurement standards. Fluxgate magnetometers measure the magnetic flux density at 1 Hz at the Intermagnet observatories [17].

The magnetic field is measured in X, Y, and Z directions continuously at all the Intermagnet observatories. Red circles in Figure 1-1 indicate location of the observatories on a map that is extracted from the Intermagnet website [16]. The recorded data from all the observatories are available in the Intermagnet database in [16]. However, analyzing the magnetic field data recorded even on the same day reveal significant differences in the signal quality. High noise levels in the signals hinders numerical analysis of GMD events for the purpose of calculating the induced electric fields in power systems.

1.3 Effects of GMDs on Electrical Power Systems

Transmission lines in a power system span over a considerably large area. The induced geoelectric field due to a GMD event imposes a potential difference between the two ends of a transmission line. This induced voltage drives a quasi-dc current into the line in case a return pass is available for the current. This quasi-dc current is known as geomagnetically induced current (GIC). This closed loop is formed by power transformers with a grounded neutral. GIC endangers the power transformers by introducing a dc flux offset into the core that leads to half-cycle saturation [18, 19]. Moreover, it causes protective relays to interrupt a part of the grid as a reaction to the harmonics generated

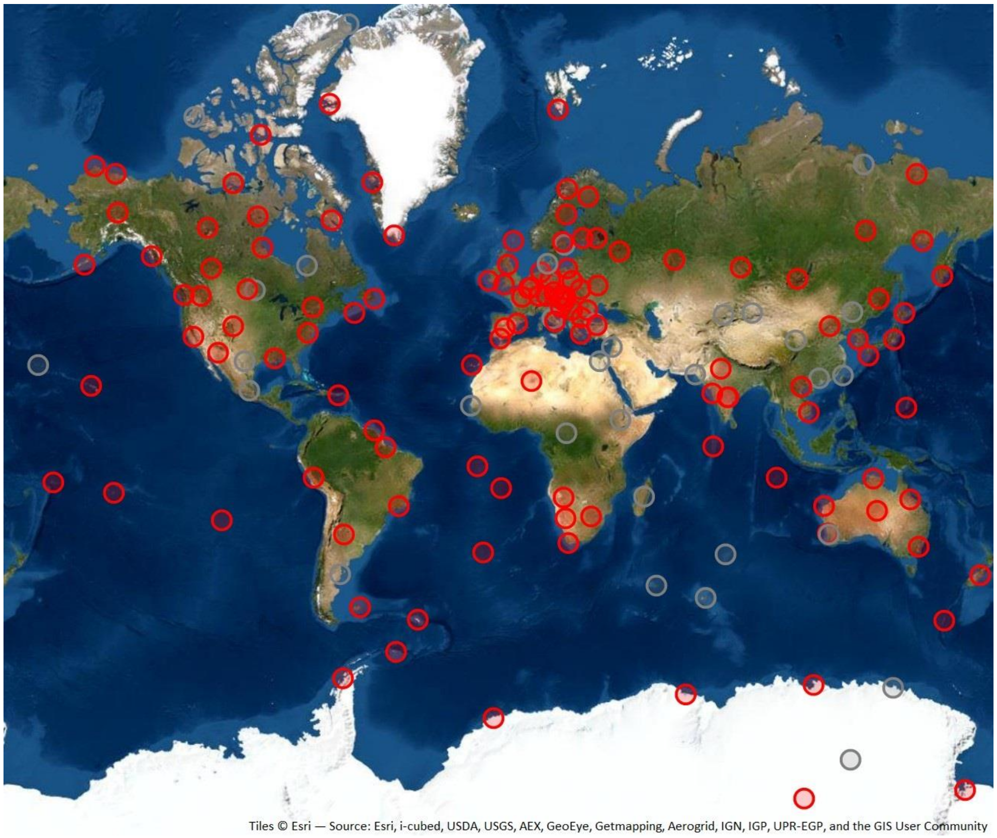

Figure 1-1: Map of geomagnetic field observatory stations [16].

due to the transformer saturation.

The saturation of the transformer leads to three major problems including overheating, generation of harmonics [20], and an increased reactive power consumption [21, 22]. Depending on direction of the GIC, saturation curve of the transformer's core is offset in one half of the cycles. The operating point of the transformer shifts towards saturation region during the half cycle with higher flux magnitude. A large amount of reactive power is consumed by the transformer due to the 90 degrees difference in phase angle of the exciting current and the voltage. Transformer's insulation overheating and voltage drop on the buses are among the significant problems caused by the half-cycle saturation.

1.4 History of Critical GMD Events

There are several incidents in the recorded history regarding impacts of powerful geomagnetic storms. These incidents are described in the following [23].

- Between Aug. 28 and Sept. 2, 1859 one of the most powerful storms in the recorded history known as Carrington event occurred and travelled the earth path in 17 hrs. This storm caused damage to telegraph systems in North America and Europe.
- Compasses deflected by about 2 degrees during a GMD event on Nov. 18, 1882.
- East-west telegraph systems were disrupted in northeastern of North America on Jun. 17,1915.
- Some infrastructure in New York such as railroad switching and signaling systems were damaged due to a GMD during May 13-15, 1921. Moreover, undersea cables and some of the telephone and telegraph systems were

damaged.

- On Mar. 24, 1940 Philadelphia's electric grid experienced voltage surges and reactive power swing. Telephone and telegraph lines were disrupted in a length more than 185,000 miles in Canada and the US.
- On Aug. 4, 1972, Bell experienced service outage at some locations. AT&T and Canadian Overseas Telecommunications Corporation reported voltage surges that led to a damage to their equipment.
- On Mar. 13, 1989, a blackout occurred in Hydro-Quebec power grid, which caused about six million customers to lose power for more than nine hours. Moreover, several transformer failures were reported in North America's power system. Note that the cost of the undelivered power in such cases goes beyond the cost of replacing the transformer itself.
- Transformers failures along with blackouts in South Africa in addition to loss of a satellite were results of a fast transit storm on Oct. 29, 2003.
- On Jul. 23, 2012, a solar storm as powerful as the Carrington event occurred. Thankfully, this storm did not travel the earth's path and missed it by one week. The economic burden of such a storm would be trillions of dollars if it had affected earth's magnetic field.

1.5 Road Map and Novel Contributions

Fundamentals of the relationship between the magnetic field and induced electric fields are established in [24, 25]. The IEEE-118 bus benchmark power system is modified in [26] to include additional parameters required for calculating GIC in power systems based on the amplitude of the induced electric fields over the transmission lines. If a noise-free magnetic field signal is fed as the input to the above-mentioned models, the GIC flows can be obtained accurately on each bus of the power system. These calculations eliminate the need for equipping the power system with numerous measuring devices to obtain GIC flows.

Magnetic field signals recorded at the observatory stations are affected by significant noise levels. The high noise levels become more problematic considering time-derivative of the signals are required for the induced electric field calculations. An offline geomagnetic field monitoring system is developed in this research to reduce noises in the magnetic field signals. The monitoring system constitutes a set of signal processing methods to obtain reliable and accurate induced electric field data from the recorded noisy magnetic field signals. Furthermore, an online geomagnetic field monitoring system is developed as well. The online monitoring system addresses challenges regarding noise reduction while relying only on previous data points in the magnetic field signals.

The proposed signal processing methods enable power system operators to obtain accurate estimates of the GIC flows. This additional current flowing through windings of power transformers causes a sudden increase in the oil-paper insulation temperate. As a result, gaseous bubbles may form on surface of the paper insulation and endanger the integrity of the insulation system [27-30]. A test setup is created as a part of this research to evaluate bubble formation in oil-paper insulations. The experimental results provide valuable information on bubbling inception temperatures and dangers of high amplitude GIC flows during severe GMD events. The block diagram in Figure 1-2 shows the steps in analyzing a GMD event. The highlighted blocks indicate contributions of this research.

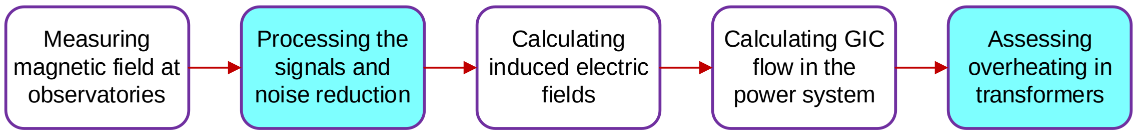

Figure 1-2: Steps in analyzing a GMD event.

1.6 Organization of the Dissertation

Main body of this dissertation is based on previous publications of the author in IEEE and IET journals. The offline geomagnetic field monitoring system is presented in Chapter 2. This chapter includes contributions from the two following papers:

[1] **M. Ariannik**, A. Rezaei-Zare and P. Werle, "Processing Magnetometer Signals for Accurate Wide-Area Geomagnetic Disturbance Monitoring and Resilience Analysis," in *IEEE Transactions on Power Delivery*, vol. 36, no. 4, pp. 2550-2558, Aug. 2021.

[2] M. Rezaei-Zare, **M. Ariannik**, and A. Rezaei-Zare, “Real-time detection of vulnerable power system areas to geomagnetic disturbance,” *IET Generation, Transmission & Distribution*, vol. 14, no. 18, pp. 3838-3845, 2020.

Chapter 3 covers the methods proposed for online monitoring of geomagnetic fields on earth’s surface. This chapter is based on the following published journal paper:

[3] **M. Ariannik** and A. Rezaei-Zare, "Online Monitoring of Magnetometer Signals for Estimating Induced Electric Fields in Power Systems," in *IEEE Transactions on Power Delivery*, 2022.

In Chapter 4, the test setup for evaluating bubble formation in oil-paper insulation of power transformers is demonstrated. The experimental results on excessive heating in the insulation system at two temperature rise rates are presented. The following publication is to be submitted that incorporates the experimental results:

[4] **M. Ariannik**, A. Rezaei-Zare, M. Kuhnke, and P. Werle, “A Comparison Between Bubble Formation on Kraft and Thermally Upgraded Papers in Synthetic Ester Oil,” *IEEE Transactions on Dielectrics and Electrical Insulations, (to be submitted).*

Finally, the dissertation concludes with Chapter 5. In this chapter, achievements of this research are summarized and an elaborative discussion is provided to enlighten the researchers on the future works toward increasing reliability of power systems during GMD events.

Chapter 2

Processing Magnetometer Signals for Accurate Wide-Area Geomagnetic Disturbance Monitoring

2.1 Introduction

Two types of solar activities cause the most powerful eruptions on the sun's surface including solar coronal holes and coronal mass ejections [1]. These eruptions release clouds of high energy plasma that can travel earth's path in 14.6 hrs [2]. The plasma causes disturbances in earth's magnetic field, and high amplitude currents are formed in an altitude of about 100 km above earth's surface that are known as auroral electrojets [4]. As a result, low frequency voltages are induced in the ground, which in turn drive a quasi-dc current into transmission lines of power system that is known as geomagnetically induced currents (GICs) [31-33].

GICs flow through grounded neutral of power transformers over a vast area of the power system. GIC endangers power transformers by introducing a dc flux offset into the core that leads to half-cycle saturation [18, 19]. The saturation of the transformer leads to three major problems including overheating, generation of harmonics [20], and an increased reactive power consumption [1, 21, 22].

Geomagnetic disturbances (GMDs) impacts on the power system are not localized, but span over several regions of the grid instead. Severe GMD events can cause blackouts similar to extreme weather conditions that lead to large scale power outages [34]. To cite an instance, the GMD event in March 1989 caused a nine-hour blackout within Hydro Quebec grid along with several transformer failures across North America [23]. Although GMD events are less common compared to meteorological disasters, their damage to the power system is significantly worse, because GMDs can cause failure of power transformers in particular as the expensive key components of power systems. This gives rise to the importance of enhancing resiliency of power systems against GMD events, which requires an accurate calculation of GICs flowing through power transformer's windings.

Earlier studies have developed geomagnetic earth models to calculate GICs in a power system [35, 36]. Input of the earth models is magnetic flux density signal B, that is measured on earth's surface by magnetometers, and they output induced electric field near earth's surface. Modified benchmark power systems have been proposed in [26, 37, 38] to calculate GIC based on induced electric fields across transmission lines. However, the benchmark systems are evaluated by a uniform electric field rather than actual measured magnetic field signals.

This chapter aims to construct a link between the earth models [35, 36] and the power system analysis [26, 37, 38] by proposing signal processing methods for wide-area monitoring of magnetic field signals. The processing methods are based on wavelet transform and are developed specifically for magnetic field signals B, considering their intrinsic features and impacts on power systems. The methods proposed in this chapter can be implemented to calculate GICs accurately, which is crucial for power system resiliency analysis when several power transformers experience half-cycle saturation due to a severe GMD event.

Several observatory stations around the world measure magnetic field *B*, on the earth's surface. Analyzing the offline data provided by the global network of observatories INTERMAGNET [16] revealed that some of the recorded *B* signals are affected by a significant noise level as well as several spikes. The noises and spikes are amplified in dB/dt signal, which is the input of the earth models. Consequently, the fluctuations manifest themselves in the calculated GIC amplitudes.

In this chapter, a method is introduced in Section 2.2 to denoise and despike the *B* signals prior to the differentiation. An instantaneous time-frequency analysis is presented in Section 2.3. Choosing an appropriate method to take the derivative of the *B* signal is of great importance due to the significant effect that it has on the signal to noise ratio (SNR) of dB/dt. In this regard, different methods of differentiation are assessed, and the most robust method among them is introduced in Section 2.4. Although the *B* signal can be sampled at 1 s intervals, practical limitations regarding transmitting the data may prevent processing the *B* signal at the same rate. This problem is addressed in Section 2.4.1, and the minimum required sampling rate is determined by a quantitative analysis. Finally, necessity of processing the *B* signals and effectiveness of the proposed methods are illustrated by calculating GICs in a modified IEEE 118-bus test case in Section 2.5.

2.2 Noise Reduction and Spike Elimination

Magnetic flux density *B* is measured continuously on earth's surface at several observatories around the world. The *B* signal is measured in *x*, *y*, and *z* directions at a maximum frequency of 1 Hz. The recorded magnetic flux density data for different observatories have been extracted from the global network of observatories INTERMAGNET. The *B* signals analyzed in this chapter pertain to a GMD event on 2015/08/15. In this section, specific features of the *B* signals are addressed in detail, and an approach is introduced towards a denoised and despiked signal.

2.2.1 Denoising B Signals

Magnetic field measurements are accompanied by noises similar to other parameters that are measured by sensors [39]. The noises in magnetometer measurements originate from white background noise [40], electrical circuit components and auxiliary circuits such as amplifiers [41, 42], and intrinsic sensor noises. The intrinsic noises are caused by the inner structure of the magnetometer and its measurement mechanism such as Barkhausen noises in magneto-impedance sensors [43], and low frequency noises known as $1/f$, i.e., inversely proportional to frequency, that are available in magnetoimpedance sensors [40, 44, 45] as well as in fluxgate sensors [42].

Importance of mitigating the noises in the *B* signal is more noticed considering that its time derivative dB/dt is used to calculate the induced electric field and the resultant GIC. Taking derivate amplifies the noises [46] and therefore, the noises in the *B* signal have to be reduced to an acceptable level prior to the differentiation.

Two orthogonal wavelet families including Daubechies and Symlet are considered to denoise B signals. Applying different mother wavelets from these two families revealed that sym4 wavelet removes sharp edges from the signal while preserves peaks amplitude as far as possible. Therefore, the magnetic field signals are decomposed down to fourth level using sym4 wavelet. Decomposing the signal down to a higher level increases the computational burden followed by a negligible improvement in terms of noise level.

Ultimately, the wavelet coefficients are shrunk, and the signal is reconstructed afterwards.

SNR is considered as a criterion to evaluate effectiveness of the denoising method. A recorded B signal can be written as

$$B_{recorded} = B_{main} + B_{noise} \tag{2.1}$$

where B_{main} can be separated from the noise B_{noise} by a lowpass filter. Earlier studies in [47] demonstrated that main frequency content of the recorded magnetic field signals during a severe GMD event in March 1989 is about 1.2 mHz. An infinite impulse response (IIR) Butterworth filter of order 10 is designed to remove the noises from the recorded signal. Cutoff frequency of the filter is set to 20 mHz considering a marginal distance from the main frequency content. Ratio of $B_{recorded}$ power to B_{noise} power yields SNR value.

SNR is calculated for both B_x and its numerical derivative dB_x/dt signal recorded at three observatory stations, and the results are compared in

Table 2-1. The data for the *B* components that have been recorded on 2015/08/15 are available in the INTERMAGNET database. Although SNR value is slightly improved in the denoised B_x, a noticeable reduction in the noise level is evident for the derivative signal obtained from the denoised B_x.

Table 2-1: Denoising effect on B_x signal and its derivative.

Station	SNR of B_x		SNR of dB_x/dt	
	Original	Denoised	Original	Denoised
Yellowknife	54.31	54.41	0.05	8.83
St John's	79.68	79.69	0.37	1.33
Sitka	58.63	58.65	0.17	1.04

2.2.2 Despiking B Signals

Analyzing the *B* data recorded by the magnetometers revealed that abrupt changes occur at random times with distinct amplitudes that do not follow a specific pattern. These spikes have a duration of either one or two seconds. The B_x signal that has been measured at Fort Churchill station is shown in Figure 2-1(a) along with a zoomed view on a spike in Figure 2-1(b). Time derivative of the B_x signal is calculated by numerical differentiation and is depicted in Figure 2-1(c) to give an insight on how spikes are introduced to the derivative signal. These spikes lead to an overestimated induced electric field; therefore, they are required to be eliminated from the signal. In the following subsection, a method is introduced to locate and replace the spikes.

2.2.2.1 Median Filtering

Median filtering is a rather straightforward method that can be applied for noise and spike suppression [48]. In this method, a sliding window comprised of an odd number of samples is shifted across the signal, and the midpoint is replaced by the median of the samples that lie inside the window. The major drawback of this method is that the spikes are smoothed rather than flattened. Moreover, not only the spikes, but all the samples are manipulated. In response to this drawback, an alternative approach is proposed, and the steps are described as follows.

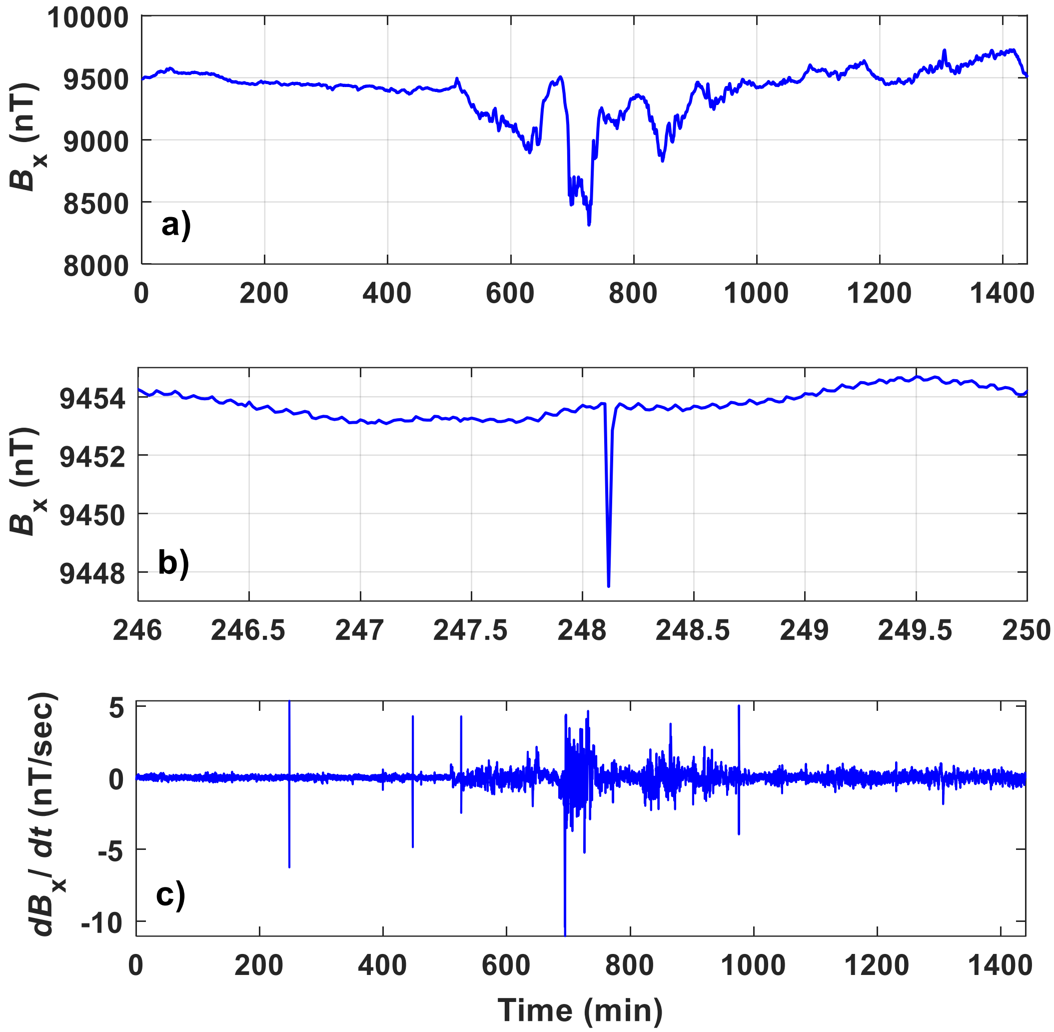

Figure 2-1: Spikes in the B_x signal recorded at Fort Churchill station; (a) B_x signal; (b) zoomed view on a spike; (c) spikes in dB_x/dt signal.

2.2.2.2 Replacement at Peak of Differences (RPD)

A window encompassing 7 samples is defined and shifted through the B_x signal. The center point of the window is replaced in accordance to the median filtering method. This filtered signal $\tilde{B}_x$, is then subtracted from the main signal B_x to generate a difference signal

D. As it can be seen in Figure 2-2, the spikes are more evident in this difference signal and can be detected by defining a prominence threshold. The threshold should be set with respect to sampling frequency of the B signals. A threshold of 0.5 and 100 proved to be suitable for sampling frequencies of 1 and 1/60 Hz, respectively. The thresholds for different sampling frequencies can be obtained by a linear interpolation. Note that the thresholds are determined after analyzing several magnetic field signals that are recorded during severe GMD events from March 1989 to August 2015.

The spikes are required to be replaced by an updated value in RPD method, since eliminating them shortens the signal and causes an inconsistent time step among the data points. A feature of the *B* signal is that the spikes in the signal are not of the same width. Furthermore, at some spikes, the sample located either before or after the spike's peak in the emerging or fading transition is of high magnitude compared with the neighborhood samples. In response to this, three samples with the center point at the

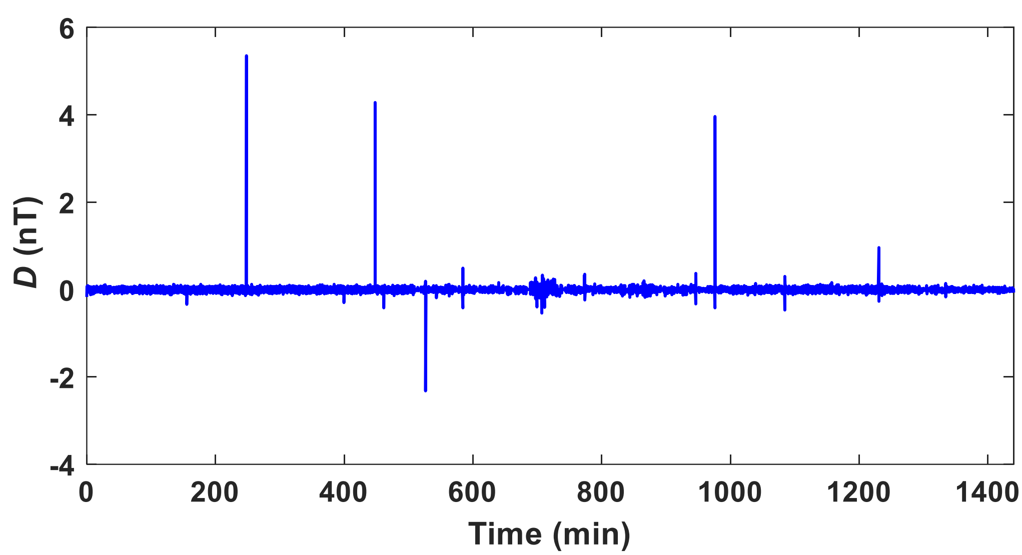

Figure 2-2: Difference signal $D = \tilde{B}_x - B_x$, obtained by RPD method.

spike's peak are replaced. Assuming peak of a spike occurs at sample x_p, this center point is replaced by a weighted average of six nearby samples excluding the samples recorded immediately before and after x_p. The samples nearer to the spike's peak are of a higher weight. The updated value of x_p is given by

$$x'_p = \sum_{k=1}^{3} \frac{k\left(x_{p+k-5} + x_{p+5-k}\right)}{12} \tag{2.2}$$

The marginal data points are then replaced by the following equations

$$x'_{p+1} = \frac{3x'_p + x_{p-2} + \sum_{k=1}^{3} k \times x_{p+5-k}}{10} \tag{2.3}$$

$$x'_{p-1} = \frac{3x'_p + x_{p+2} + \sum_{k=1}^{3} k \times x_{p+k-5}}{10} \tag{2.4}$$

The updated center point x'_p, is included in replacement of the marginal samples; however, the value of the center point x_p is updated in (2.2) independently of the updated marginal samples. As a result, six samples are included in (2.2), whereas only five datapoints are considered in (2.3) and (2.4) to calculate x'_{p+1} and x'_{p-1}, respectively.

Unlike the median filtering method where all of the samples of a signal are modified, spikes are the only datapoints that are detected and then replaced in RPD method. Hence, the remining data points are remained unchanged in RPD method. The two methods of despiking including median filtering and RPD are compared in Figure 2-3 for the signal recorded at Fort Churchill station on 2015/08/15. It can be seen that the RPD method has smoothed the spike completely unlike the median filtering method.

2.2.2.3 Wavelet Decomposition Method

The drawback of the RPD method is that it can only smooth the spikes under steady state conditions. In case of a spike during a severe GMD event, where the spike falls within the steep region of the *B* signal, the RPD method is unable to detect the spike. Furthermore, the spikes occurring within oscillatory regions of *B* are hardly detectable by the RPD method. Figure 2-4 illustrates an example of cases where the spikes are not detected by RPD method. In this figure, the B_x signal recorded at Fort Churchill station along with time derivative of the modified signal using RPD method is shown. The two dashed vertical lines show the location of the spikes that are not detected by RPD method. The first spike in Figure 2-4(b) has a high magnitude that leads to an incorrect detection of a high amplitude GIC. Since this spike has occurred during oscillatory region of dB_x/dt signal, it can be easily misinterpreted as a high amplitude GIC. Therefore, an alternative approach is presented to detect the spikes with a higher precision.

Discrete wavelet transform (DWT) decomposes a signal to detail and approximation coefficients that represent high and low frequency components of the signal, respectively.

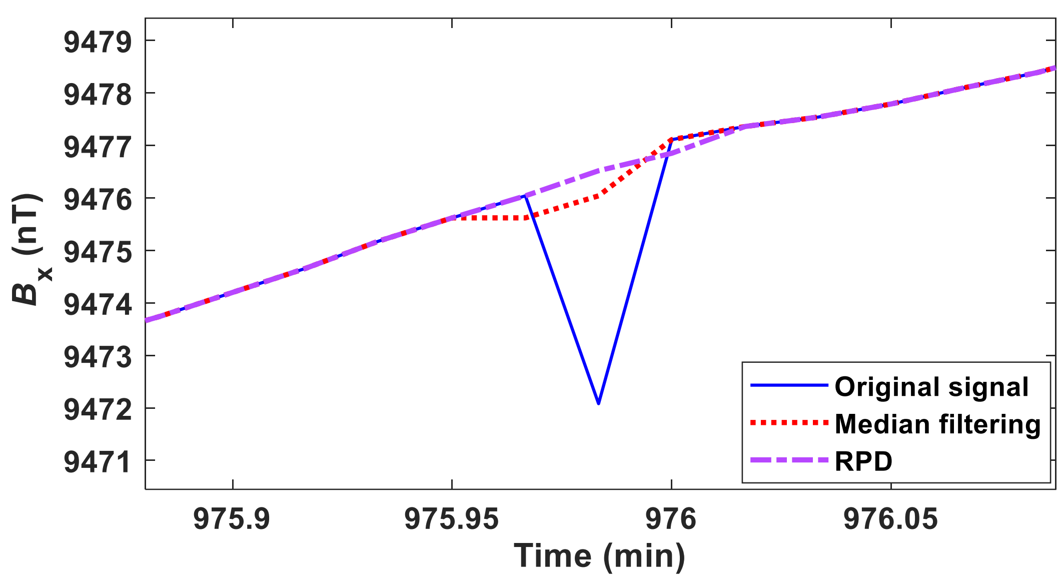

Figure 2-3: Comparing median filtering and RPD methods in smoothing a spike in the signal recorded at Fort Churchill station on 2015/08/15.

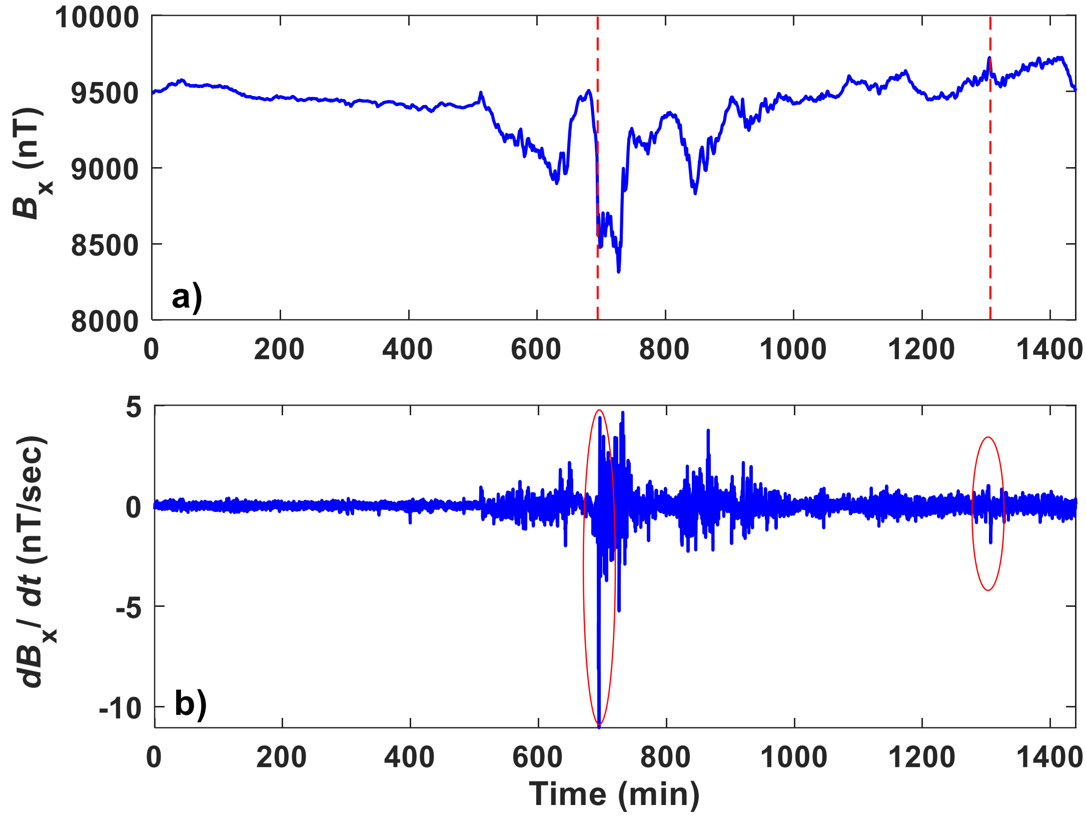

Figure 2-4: Despiking using RPD method; (a) B_x signal; vertical lines indicate the missed spikes; (b) dB_x/dt; ovals surround the missed spikes.

Since spikes emerge suddenly in a signal, their frequency content is significantly higher than the main frequency of the signal. Hence, the spikes are noticeable in the detail signal and can be located by the same approach defined in RPD method, i.e., setting a prominence threshold.

DWT is implemented by applying the signal to a set of low- and high-pass filters followed by a downsampling that reduces the signal length to one half. If the spikes are detected in this reduced length signal, an erroneous detection may occur. The reason is that the spike may be located at a data point that has been eliminated due to the downsampling. In response to this difficulty, stationary wavelet transform (SWT) also known as undecimated wavelet transform is used instead of DWT. Since the signal is not downsampled in SWT, the spikes can be located accurately in the detail signal.

The first step towards despiking in the wavelet decomposition method (WDM) is to calculate SWT of the *B* signal using sym4 wavelet at a decomposition level of one. In the second step, the spikes in the *B* signal are detected by locating the peaks of the detail signal that is obtained by SWT as shown in Figure 2-5. A comparison between Figure 2-2 and Figure 2-5 reveals that WDM has detected all the spikes and two of them are missed by RPD, which are surrounded by ovals in Figure 2-5. This implies the superiority of WDM over RPD method, particularly at regions where the spike occurs during an abrupt change in the *B* signal as shown by the first oval.

The last step of despiking is comprised of replacing the data point at the spikes and at the adjacent samples similar to the approach presented in RPD method using (2)-(4). This ensures all the spikes in the signal are detected and flattened.

2.3 Time-Frequency Analysis of Magnetic Field Signals

The induced geoelectric field on earth's surface due to a GMD can be calculated by plane wave, line current, and three-dimensional current system models depending on the desired accuracy [25]. Complex image method (CIM) was introduced to cope with complexity of the calculations [49]. The horizontally one-dimensional model assumed in CIM limits its application to small geographical areas. Multizone earth models allow a more accurate modeling of the earth over large scale geographical regions [35, 36]. In this method, the earth is divided into several multilayer regions each of which has a specific transfer function. To cite an instance, Figure 2-6 illustrates a map of the province

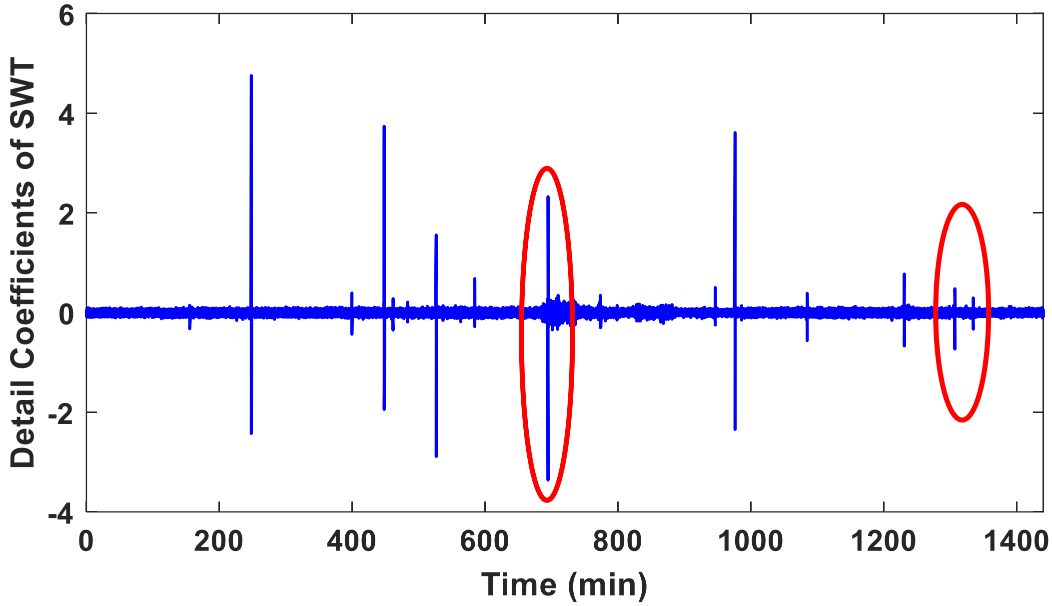

Figure 2-5: Spikes in the detail coefficients of SWT of B_x signal recorded at Fort Churchill station; ovals show spikes that are not detected by RPD method.

of Ontario with five resistivity zones, and amplitude of the earth's transfer function for each zone is shown in Figure 2-7. The time derivative of the magnetic flux density signal B that is measured by magnetometers is the input of the earth model, and it outputs the induced geoelectric field near the earth's surface.

The B signal that is measured on earth's surface changes with a variable frequency during a GMD event. On the other hand, amplitude of earth's transfer functions is inversely proportional to the frequency according to Figure 2-7. Consequently, amplitude of GIC is affected by variations in frequency of the B signals. It is worthwhile to mention that earlier studies [24] have assumed the magnetic field to oscillate with a constant

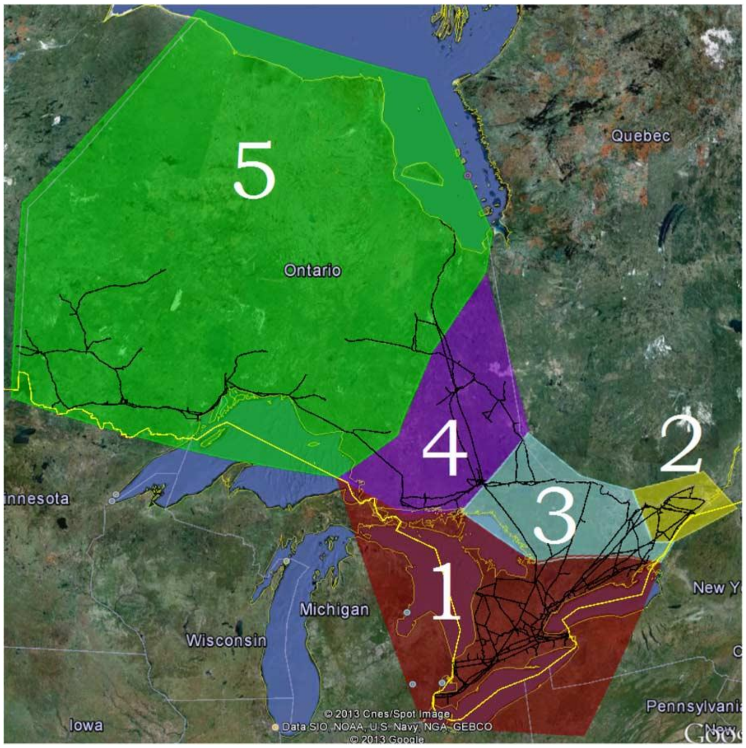

Figure 2-6: Five resistivity zones of Ontario [35].

frequency during a GMD event.

In this chapter, a detailed discussion is presented on the methods available for an instantaneous time-frequency analysis of signals, and their effectiveness on the B signals are compared by implementing them in MATLAB. Finally, an instantaneous time-frequency analysis is performed particularly during peak of a GMD event, when amplitude of dB/dt is at its peak.

2.3.1 A Review on Time-Frequency Analysis Methods

Several methods are available for the time-frequency analysis among which short time

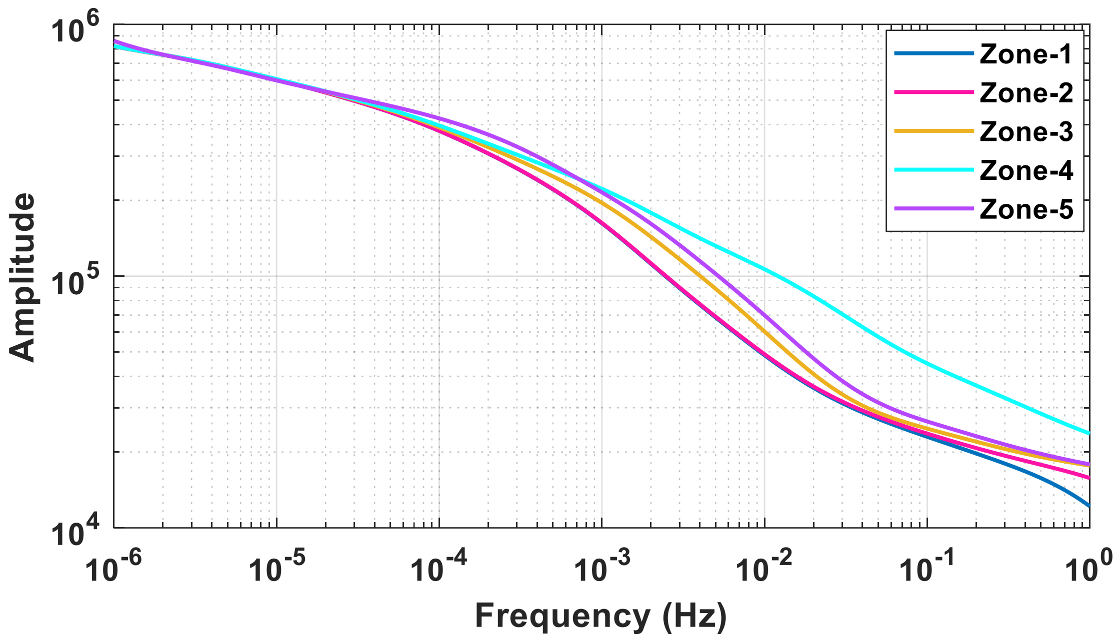

Figure 2-7: Amplitude of earth's transfer functions for Ontario [35].

Fourier transform (STFT) and continuous wavelet transform (CWT) are the fundamental methods. In STFT method, a symmetric sliding window $g(t)$ is defined and shifted across the signal. The Fourier transform of samples within each window yields a localized frequency decomposition that corresponds to the time when the midpoint sample inside the window is recorded. STFT of a function $x(t) \in L^2(\mathbb{R})$is calculated as follows [50]

$$STFT\ x(\tau, f) = \langle x, g_{t,f} \rangle = \int_{-\infty}^{+\infty} x(t)\ g(t-\tau)\ e^{-j2\pi f t}\ dt \qquad (2.5)$$

where τ and f denote the time shift in the window, and frequency components, respectively. Accuracy of the frequency spectrum depends on the type of the window and the overlapping distance, whereas its resolution is dominated by length of the window. Hence, choosing a window and determining its properties is a challenging task in this method.

A high resolution in both time and frequency domains cannot be obtained. The optimum combination of the resolutions is obtained based on the importance of the features that are to be extracted from the time or frequency domain. A constant time-frequency resolution is obtained in STFT method, since the same window is shifted through the signal. In this regard, CWT is proposed as an alternate method that provides a transform with different resolutions.

CWT of a function $x(t)$, is calculated by projecting it on a set of wavelets $\psi_{\tau,a}$ that are scaled and translated by a and τ, respectively and is given by [50]

$$W\,x(\tau,a) = \langle x, \psi_{\tau,a} \rangle = \int_{-\infty}^{+\infty} x(t) \frac{1}{\sqrt{a}} \psi^* \left(\frac{t-\tau}{a} \right) dt \tag{2.6}$$

The wavelets are constructed by scaling and translating a mother wavelet ψ. Complex conjugate of mother wavelets ψ^* are incorporated in the CWT. The scaling parameter enables CWT to yield a variable time-frequency resolution, unlike the STFT method. An increase in the scale a, leads to an expanded wavelet, which provides a higher time resolution and a lower frequency resolution. Each scale corresponds to a pseudo-frequency f_p by [51]

$$f_p = \frac{f_s f_c}{a} \tag{2.7}$$

where f_s and f_c denote sampling frequency and mother wavelet center frequency in Hz, respectively. The center frequency is frequency of a periodic sine wave that resembles the center of the mother wavelet the most and corresponds to its dominant frequency component.

Wigner-Ville distribution (WVD) is the third instantaneous time-frequency analysis method that is applied in this study. WVD has been introduced before the CWT and is more similar to STFT than to CWT. In WVD method, Fourier transform of a function $x(t)$ is calculated as follows [50]

$$WV\ x(\tau, f) = \int_{-\infty}^{+\infty} x\left(\tau + \frac{t}{2}\right)\ x^*\left(\tau - \frac{t}{2}\right) e^{-j2\pi f t}\ dt \tag{2.8}$$

This distribution maps the energy concentration in a time-frequency plot. If energy of $x(t)$ is concentrated at a specific coordinate on the time-frequency plot, WVD has a corresponding concentration at the same coordinate. Nevertheless, WVD lacks a fundamental property required for an appropriate time-frequency analysis tool that is positivity. Moreover, when a signal is comprised of different components, interference terms are generated [50] due to the quadratic nature of WVD. A smoothed pseudo-Wigner-Ville (SPWV) distribution is proposed to cope with the aforementioned difficulties by applying two windows, *g* and *h* [51]

$$SPWV\ x(\tau, f) = \int_{-\infty}^{+\infty} \int_{-\infty}^{+\infty} g(t-\tau)\ h(t)\ x\left(\tau + \frac{t}{2}\right) x^*\left(\tau - \frac{t}{2}\right) e^{-j2\pi f t}\ dt\ d\tau \tag{2.9}$$

Applying the first window *h*, decreases the interference terms and provides a pseudo WVD, whereas the latter window *g*, causes an improvement in the resolution and smooths the distribution in time.

2.3.2 Investigating Time-Frequency Decompositions

B_x data that is measured on 1989/03/13 at Ottawa observatory is considered for an instantaneous time-frequency analysis. The B_x signal along with its numerical derivative are depicted in Figure 2-8(a) and (b), respectively. This specific B_X signal is considered for the time-frequency analysis because of the high amplitude oscillations in the corresponding dB_x/dt signal. Note that the GMD event that occurred on 1989/03/13 caused a nine-hour blackout in Quebec power grid.

CWT, STFT, and SPWV distribution methods are implemented on the Ottawa B_x signal and the corresponding time-frequency spectrums are depicted in Figure 2-9. Although an accurate frequency decomposition is provided by the scalogram of CWT in Figure 2-9(a), a poor decomposition is observed in the spectrogram of both STFT and SPWV distribution in Figure 2-9(b) and Figure 2-9(c), respectively. To cite an instance, in Figure 2-9(b) and Figure 2-9(c) the components with the highest power all have a frequency below 0.1 mHz during the 24 hrs period, whereas some of the components with the highest power have a frequency higher than 0.1 mHz in the CWT scalogram. CWT method has provided a frequency decomposition with a higher resolution compared to the other two methods. Moreover, a comparison between Figure 2-8(b) and Figure 2-9 reveals superiority of the energy distribution accuracy of CWT scalogram over the STFT spectrogram and SPWV distribution. In other words, the high frequency oscillations in Figure 2-8(b) correspond to the energy distribution shown in Figure 2-9(b).

2.3.2.1 Frequency Components of dB_x/dt Signal

The induced geoelectric field is calculated based on time derivative of B signal, dB/dt. Therefore, CWT of dB_x/dt signal recorded during March 13-14, 1989 is computed using a synchrosqueezed wavelet transform to sharpen the time-frequency resolution. The reader may refer to [52, 53] for a detailed discussion on the synchrosqueezed transforms. Several frequency components with diverse magnitudes are available in the dB_x/dt

signal at each moment. Frequency of the signal samples that correspond to a specific order of power are called ridges and represented in a time-frequency plot. The ridge with the highest power is extracted from the CWT scalogram of dB_x/dt signal and plotted in Figure 2-10. This frequency ridge is not capable of providing an accurate instantaneous frequency due to the severe disturbances that are introduced to the ridge.

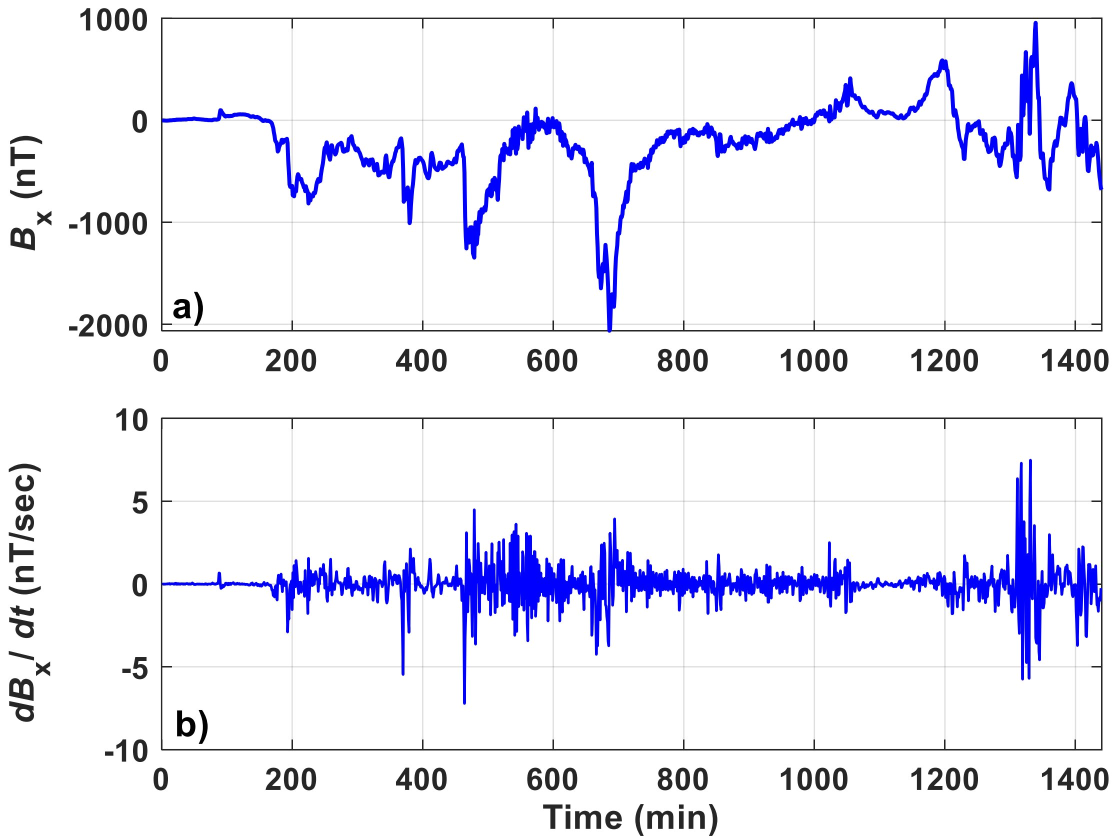

Figure 2-8: Magnetic field signal recorded at Ottawa observatory on 1989/03/13; (a) B_x signal; (b) dB_x/dt signal.

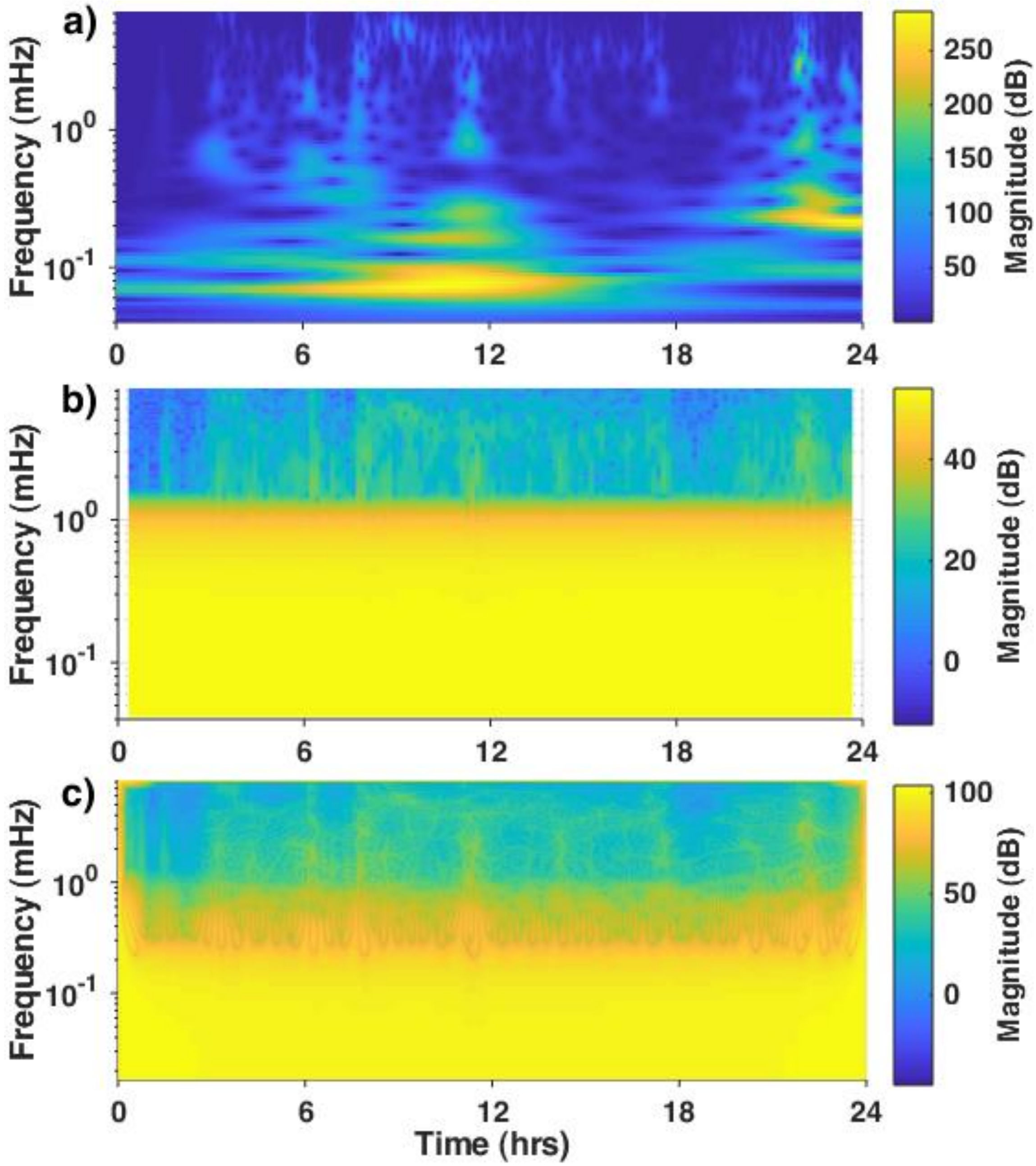

Figure 2-9: Time-frequency analysis of the B_x signal recorded on 1989/03/13; (a) CWT scalogram; (b) STFT spectrogram; (c) SPWV distribution.

In the second approach to the frequency analysis, the B_x signal is first denoised and despiked with respect to the methods presented in Section 2.2.2. The numerical derivative of the modified signal is then applied to extract the frequency ridge using synchrosqueezed wavelet transform. The dB_x/dt signal is plotted in Figure 2-11(a) together with the corresponding frequency ridge. Note that the intercept for B_x and its derivative is compensated in the plots shown in this contribution. Several spikes with a duration of one minute, i.e., one sample, are visible in this ridge that originate from a corresponding abrupt change in the dB_x/dt signal. These spikes are detected by defining a threshold limit equal to 1 mHz and then replaced by the mean value of two adjacent samples. The despiked ridge depicted in Figure 2-11(b) represents a smoother and more accurate pattern compared with that of shown in Figure 2-11(a). To cite an instance, Figure 2-11 reveals that the dB_x/dt is approximately maintained at the same level after

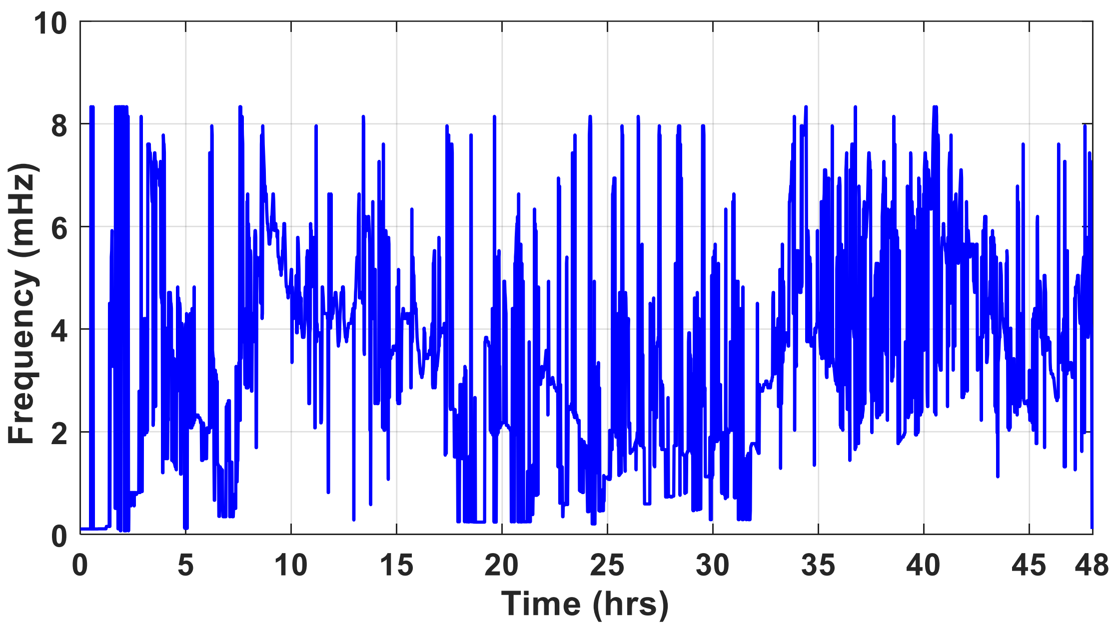

Figure 2-10: Instantaneous frequency of dB_x/dt during March 13-14, 1989.

35 hrs up to 40 hrs and therefore, low frequency oscillations are expected around that time. Nevertheless, a comparison between Figure 2-11(a) and Figure 2-11(b) demonstrates that the frequencies represented by the unmodified ridge in the first figure include high amplitude fluctuations in the abovementioned steady state period, which

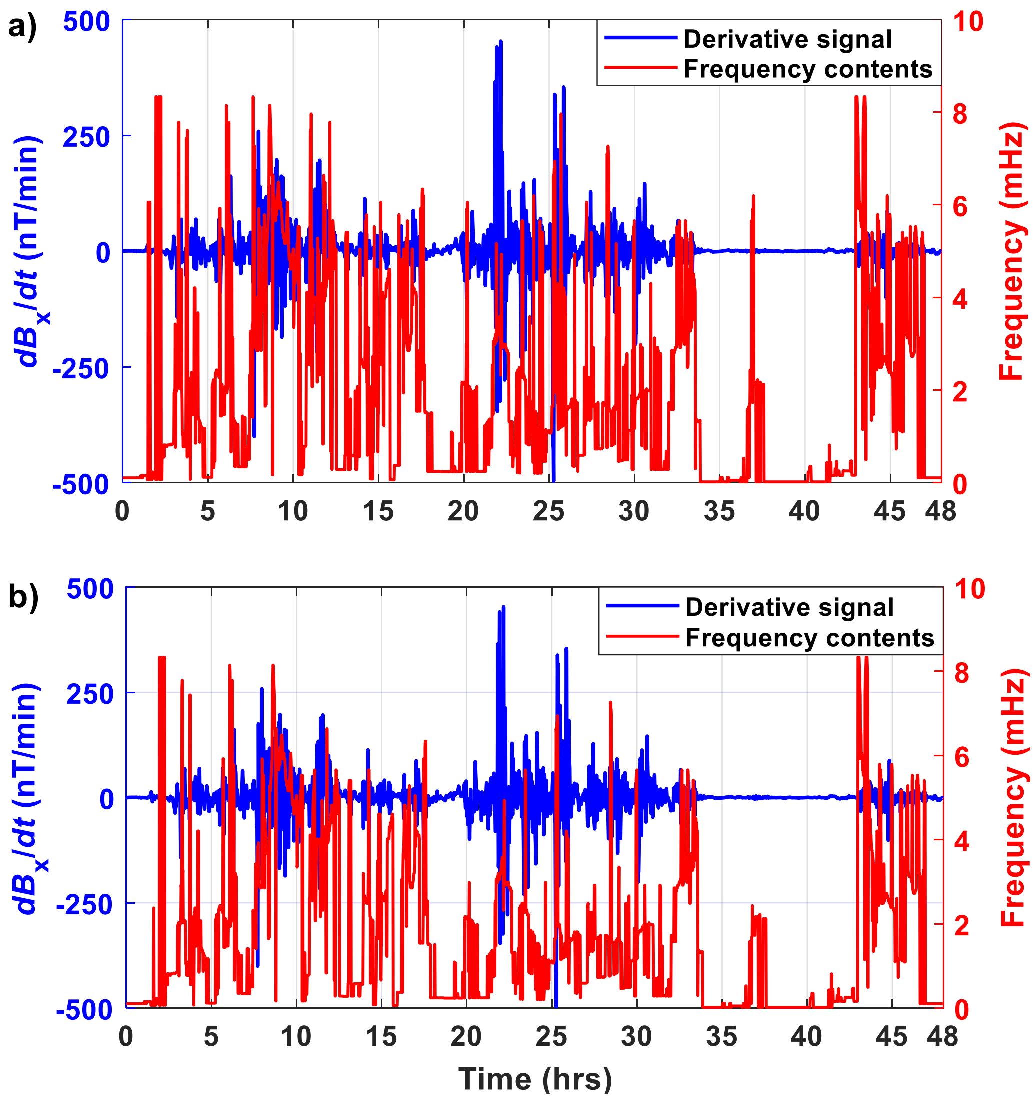

Figure 2-11: Instantaneous frequency of denoised dB_x/dt during March 13-14, 1989; (a) unmodified frequencies (b) despiked frequencies.

implies an erroneous frequency detection.

2.3.2.2 Frequency Components of B_x Signal

It was shown that denoising and despiking the B signal prior to the differentiation leads to a more accurate frequency decomposition. However, differentiation amplifies the noises in the signal and introduces high frequency components to the frequency ridge. Time derivative of a signal includes the same frequency contents as the main signal except for the dc component. Even though dB/dt is the input of the earth models for calculating the induced geoelectric field, B signal can be applied for the time-frequency analysis, and it yields the same frequency contents as that of dB/dt. Replacing dB/dt with B signal for the time-frequency analysis eliminates the high frequency components in the frequency ridge that are associated with the amplified noises in dB/dt. In this regard, the frequency ridge of B signal is obtained and compared with that of dB/dt in the next step.

The B_x signal captured during March 13-14, 1989 is first denoised and despiked by implementing the corresponding methods presented in this regard in Section 2.2. The frequency ridge is then extracted from the synchrosqueezed wavelet transform of B_x. The spikes in the ridge are flattened by replacing them with mean of two adjacent data points.

The instantaneous frequencies are plotted in Figure 2-12 together with the B_x signal. The fluctuations in the frequency ridge as well as the spikes are significantly reduced compared with the frequency ridge depicted in Figure 2-11(b). Although amplitude of the B_x signal varies in the first twenty hours, frequency of the variations is remained below 0.5 mHz. However, the ridge obtained based on dB_x/dt in Figure 2-11(b) represents high amplitude fluctuations in the same period. Hence, a more accurate approach to the instantaneous time-frequency analysis of dB/dt signal is required to extract the frequency ridge from the main signal prior to the differentiation. This ensures avoiding excessive noise in the frequency ridge.

As it can be seen in Figure 2-12, frequency of the B_x signal jumps to a few millihertz at several instants within the time span of the GMD event. To cite an instance, the frequency ridge has fluctuations after about 22 hrs. This period is of the highest importance due to the high amplitude GICs driven in the power system during this time period. A third approach is proposed in the following subsection to increase the accuracy of the frequency detection during the peak of a GMD event by preventing sudden changes in the amplitude of the frequency ridge. Note that a small deviation in the frequency leads to a significant change in the amplitude of the earth transfer function as depicted in Figure 2-7. This implies the importance of an accurate instantaneous frequency detection

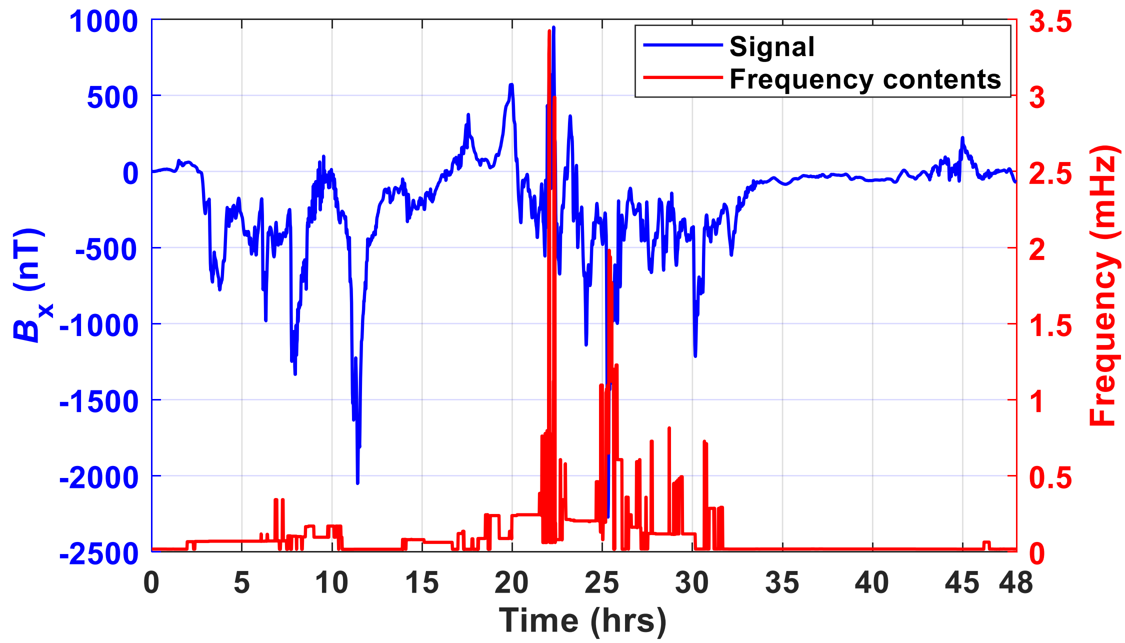

Figure 2-12: Despiked frequency ridge of the modified B_x signal recorded during March 13-14, 1989.

considering the earth transfer function.

2.3.3 Extracting Frequency Components from Filtered B_x Signal

A tool more powerful than the wavelet denoising is required to smooth the B_x signal efficiently. A low-pass finite impulse response (FIR) filter is designed as an alternative to the wavelet denoising to filter out high frequency contents pertained to fluctuations. Various filters can be adopted for this purpose among which a Savitzky-Golay filter [54] of order 3 is selected. The reason is that this filter decreases the peak's magnitude of the B_x signal less compared with the other filtering methods while smooths the signal considerably. In this approach, although high frequency components of the B_x signal are filtered by the Savitzky-Golay filter, the extracted frequency ridge is processed in two stages. First, the frequency ridge is despiked using the same method that is applied for despiking B_x signal. In the latter stage, the frequency ridge is passed through a median filter of order 13th to flatten the peaks that have a low width. The principle of a median filter is to slide a window along the signal and replace the midpoint with the median value of samples that lie inside the window [48].

The proposed signal processing method for the time-frequency analysis is applied to a combination of sinusoidal signals, where the reference frequencies are available for verification. A function $x(t)$ is defined as follows:

$$x(t) = \begin{cases} 10\sin(2\pi(f)t) + wn & 0 < t \leq 0.15\text{s} \\ 10\sin(2\pi(f)t) + 30\cos(2\pi(5f)t) + wn & 0.15\text{s} < t \leq 0.3\text{s} \\ 10\sin(2\pi(f)t) + 30\cos(2\pi(5f)t) + 90\sin(2\pi(10f)t) + wn & t > 0.3\text{ s} \end{cases} \tag{2.10}$$

where f is the frequency, and wn indicates white noise. The base frequency f equals 10 Hz, and power of the white noise is 20 dBW. Function $x(t)$ is plotted versus its instantaneous frequencies in Figure 2-13. The dominant frequencies are identified correctly and illustrated by the frequency ridge. Although the first segment of $x(t)$ with a frequency of 10 Hz is highly distorted by the white noise, the corresponding frequency ridge is stable and detected accurately. Since the frequency detection method is validated, it is applied to the B_x signal in the next step.

The filtered B_x signal that is recorded during March 13-14, 1989 is plotted against the associated frequency ridge in Figure 2-14. Note that the frequency ridge is despiked and passed through a median filter. The instantaneous frequencies in Figure 2-14 are more stable compared with the frequency ridge shown in Figure 2-12. Moreover, a reduction in the value of the instantaneous frequencies is evident, since the high frequency

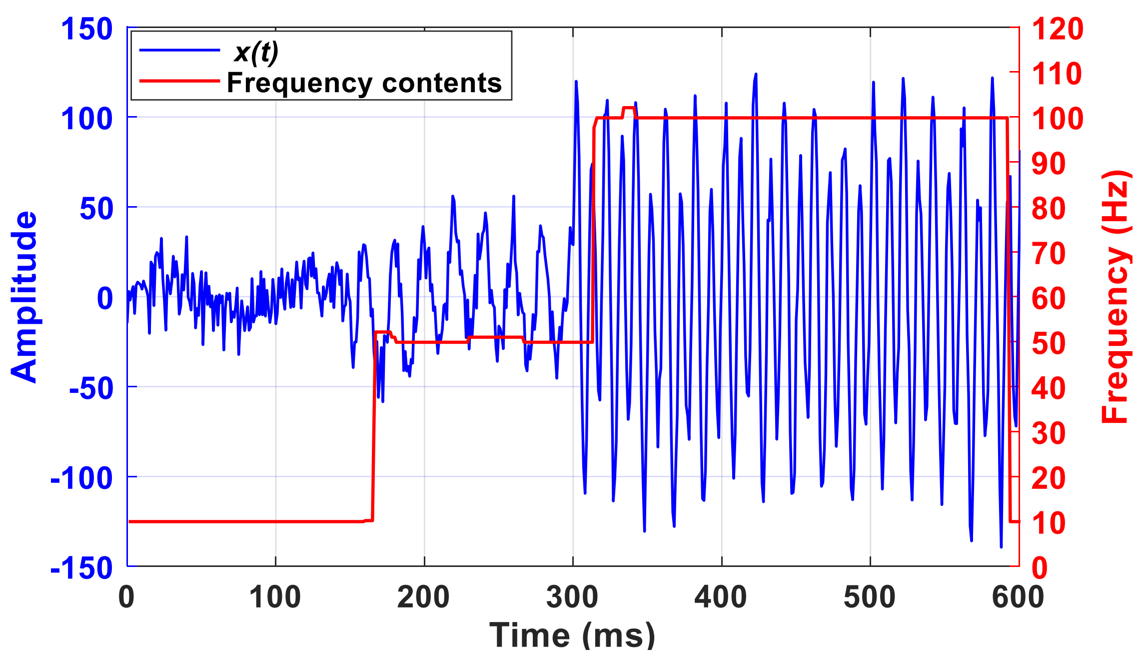

Figure 2-13: $x(t)$ versus its instantaneous frequencies.

components of B_x are shrunk more by the Savitzky-Golay filter than by the wavelet denoising method. As the third comparison, the global peak of the frequency ridge coincides with the peak of the GMD event for the signal pairs depicted in Figure 2-14, unlike the non-filtered signals in Figure 2-12.

The correlation between the frequency ridge and dB_x/dt signal is investigated near their global peak that is indicated by an oval in Figure 2-15, since this region is of the highest interest from the GIC point of view. As it can be seen in Figure 2-15, the frequency ridge follows the abrupt changes in dB_x/dt that are occurred after 25 hrs. Moreover, this figure reveals that the high amplitude changes in the dB_x/dt are of a higher frequency. Based on the earth transfer functions in Figure 2-7, amplitude of the earth's transfer functions and therefore, amplitude of the induced geoelectric field are inversely

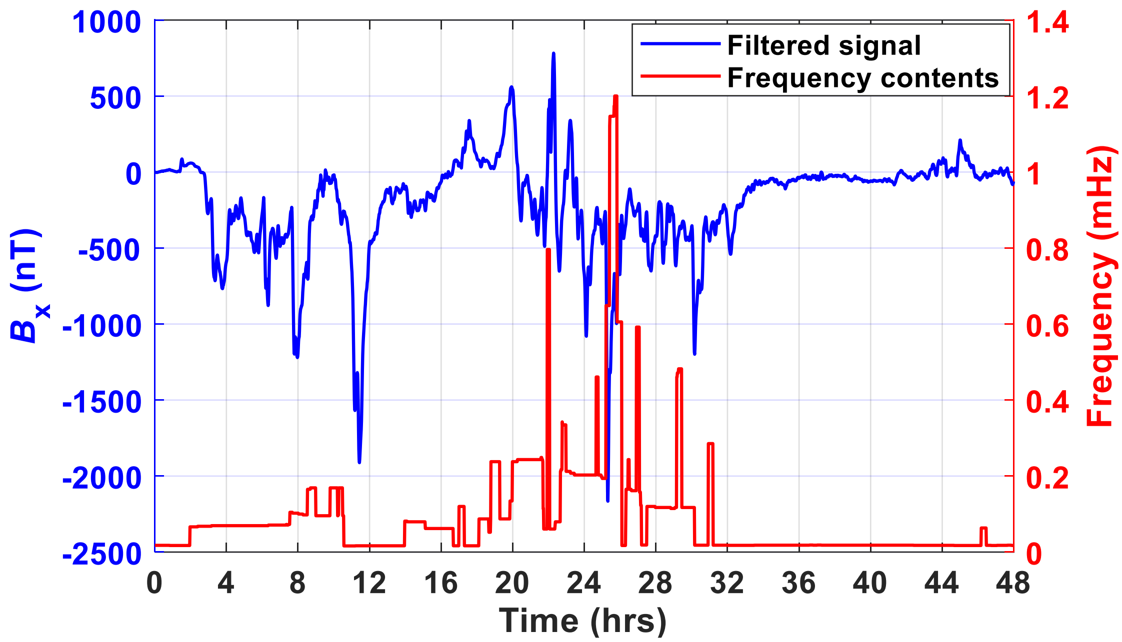

Figure 2-14: Filtered B_x signal versus its modified instantaneous frequencies during March 13-14, 1989.

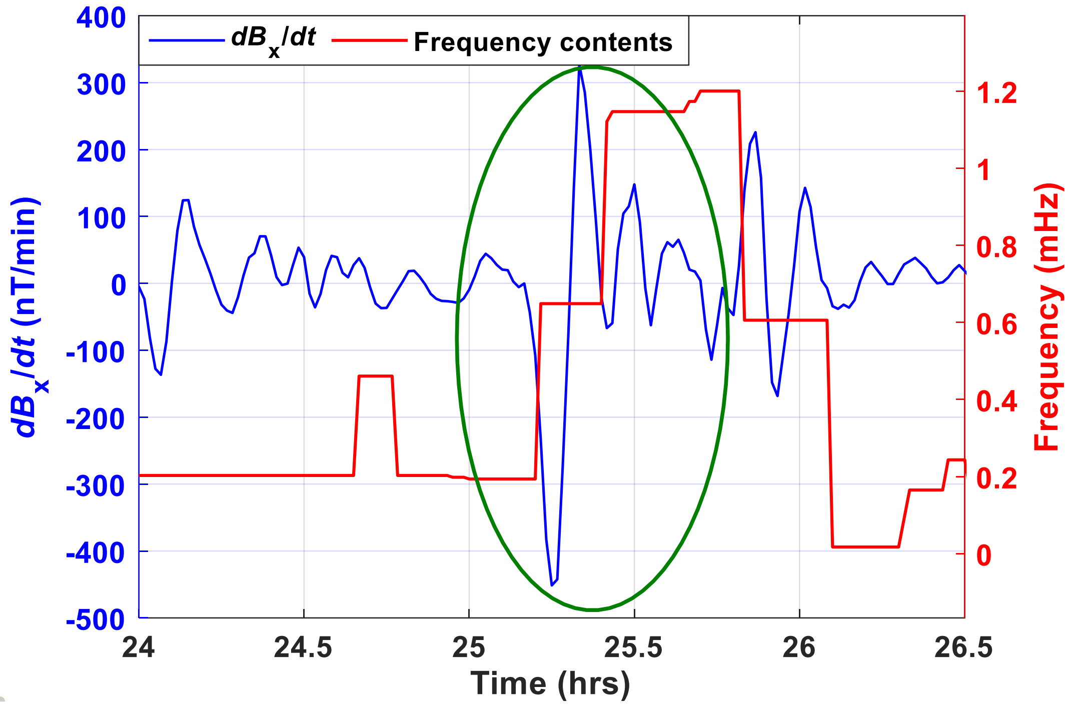

Figure 2-15: dB_x/dt signal versus instantaneous frequencies of the filtered B_x during peak of the GMD event on March 13 and 14, 1989.

proportional to the frequency. Hence, in case of oscillations in dB_x/dt with identical amplitudes but distinct frequencies, the oscillations that are of a higher frequency result in induced geoelectric fields with lower amplitudes.

2.4 Taking Derivative of *B* signal

Denoising the B signal and eliminating its spikes prepares the signal for further steps towards calculating the induced electric field. In this section, different methods for taking derivative of a signal are compared, and the best method among them is introduced.

The straightforward method to take derivative of a signal is to apply numerical differentiation, where the difference between two successive samples is divided by the time step. Although simplicity and computational speed are the two advantages of this method, the noise in the signal is amplified in its derivative. Finite differences methods such as backward Euler method suffer from the same disadvantage since the noises are not considered in the approximations applied in these methods. If fundamental of the system that generates the signal is known, Kalman filter [55], sliding mode[56], and super twisting [57] methods could be useful for the derivate calculation. Although two GMD system models are introduced in the literature[58], the simplifications made in these models cause a decrease in the accuracy if the above-mentioned differentiation methods are applied.

FIR filters can be designed to take the derivative as well. Applying them on the *B* signals revealed two major drawbacks of this method. First, a high filter order is required to achieve a smooth derivative signal, which leads to a longer delay in the filtered signal in addition to the introduced transient. The latter drawback is that peaks of the derivative signal, which represent the corresponding peaks in the GIC signal, are modified significantly at higher filter orders. Consequently, a less known method is applied in this research to take derivative of noisy B signals considering the drawbacks of the conventional methods.

Wavelet transform has been previously applied to approximate derivative of a noisy signal in analytical chemistry [59] and biomedical studies [60] as well as in detecting faults in satellite systems [61]. The principles of the wavelet-based differentiation are represented in the following.

CWT of a function f is obtained by [62]

$$W\,f(u,s) = \int_{-\infty}^{+\infty} f(t)\frac{1}{\sqrt{s}}\psi^*\left(\frac{t-u}{s}\right)dt \qquad (2.11)$$

where ψ is a mother wavelet, and u and s are translation and dilation parameters, respectively. A fast decaying wavelet with a single vanishing moment can be defined by

$$\psi(t) = -\frac{d\theta(t)}{dt} \tag{2.12}$$

The wavelet transform of f can be written as

$$W\,f(u,s) = s\frac{d}{du}(f * \bar{\theta}_s)(u) \tag{2.13}$$

where $\bar{\theta}_s(u) = \frac{1}{\sqrt{s}}\theta(-\frac{u}{s})$. The term $f * \bar{\theta}_s$ represents a weighted average of f, and therefore, the resulting wavelet transform yields derivate of the smoothed f. If the fast decaying θ has a nonzero integral as

$$K = \int_{-\infty}^{+\infty} \theta(t)dt \tag{2.14}$$

the derivative of f can be calculated as follows according to (7)

$$\lim_{s \to 0} \frac{W\,f(u,s)}{s^{3/2}} = Kf^{(1)}(u) \tag{2.15}$$

Advantage of this method over the above-mentioned methods is that smoothing is incorporated into the differentiation process. The degree of smoothing is controlled by the scale parameter s. Choosing a large value for the scale parameter leads to a smoother derivate signal, whereas decreases accuracy of the approximation in (9).

Mother wavelet and value of the scale parameter are the two factors that are required to be determined before implementing the wavelet differentiation method. The search for the appropriate mother wavelet is limited to those with one vanishing moments. Except the gaussian wavelet, other wavelets provide the same results. For a specific scale value, Gaus1 wavelet modifies the peaks more and introduces a longer transient compared to the other wavelets. In response to this, sym1 wavelet is applied for taking time derivative of the *B* signals.

Three signals with a sampling frequency of 1 Hz and high amplitude oscillations are considered to evaluate efficiency of the differentiation method. SNR and deviation in the peaks' amplitude (DPA) of the derivative signals are reported in Table 2-2. DPA is percentage of the change in the peak's amplitude with respect to the numerical differentiation of B signal as the reference signal and is calculated by

$$DPA = \frac{\max(x_n) - \max(x_w)}{\max(x_n)} \times 100 \tag{2.16}$$

where x_w and x_n denote the derivative signals obtained by the wavelet and numerical differentiation methods, respectively. Normalized correlation coefficient (NCC) is applied as another criterion to measure the degree of correlation between x_w and x_n [63]:

$$\mathrm{NCC_D} = \frac{\sum_{k=1}^{N} x_n(k).\, x_w(k)}{\sqrt{\left(\sum_{k=1}^{N} x_n^2(k)\right).\left(\sum_{k=1}^{N} x_w^2(k)\right)}} \tag{2.17}$$

NCCM is calculated as well to evaluate the correlation between the main and the denoised and despiked B_x signal. Value of NCC ranges from -1 to +1, where the upper limit represents the highest correlation. Both NCCM and NCCD are listed in Table 2-3. The aim is to increase SNR value of dB_x/dt while the peak values are remained

Table 2-2: Evaluating effect of the scale parameter on dB_x/dt signal; DPA values are in percent.

Station	Scale 4		Scale 8		Scale 16	
	DPA	SNR	DPA	SNR	DPA	SNR
Fort Churchill	-1.64	7.57	-5.74	8.13	-12.45	9.57
Yellowknife	-1.32	9.04	-3.02	9.51	-6.03	10.71
Iqaluit	-1.53	8.02	-4.82	8.56	-10.79	9.86

unmodified.

As it can be seen in Table 2-2, SNR and DPA are updated in opposite direction with increased scale value. The same behavior is seen between value of the scale parameter and NCCD in Table 2-3. Scales greater than 8 affect the peaks of dB_x/dt significantly and therefore, they are ignored for the further analyses. Note that the low NCCD for Yellowknife station is because of highly distorted B_x signal recorded at this station. Hence, the search for the appropriate scale is limited to two values, i.e., four and eight.

The B_x signal received by Fort Churchill station on 2015/08/15 is denoised and despiked, and its derivative is depicted in Figure 2-16 for a short period of time in vicinity of the global minimum. The three signals plotted in this figure represent the derivatives obtained by numerical differentiation and by the wavelet-based method with scale values of 4 and 8. The high frequency oscillation that is encompassed by the oval in Figure 2-16 is smoothed by a scale value of 8. The *B* signals recorded by different stations were analyzed, and a scale of 8 was capable of smoothing multiple oscillations through the dB/dt signals. Consequently, sym1 wavelet with a scale value of 8 is considered to approximate the derivative of B signals by (9).

Table 2-3: Correlation coefficients between the main and modified signals.

Station	Scale 4		Scale 8		Scale 16	
	NCC_M	NCC_D	NCC_M	NCC_D	NCC_M	NCC_D
Fort Churchill	1.00	0.99	1.00	0.98	1.00	0.12
Yellowknife	1.00	0.11	1.00	0.11	1.00	0.01
Iqaluit	1.00	1.00	1.00	0.99	1.00	0.13

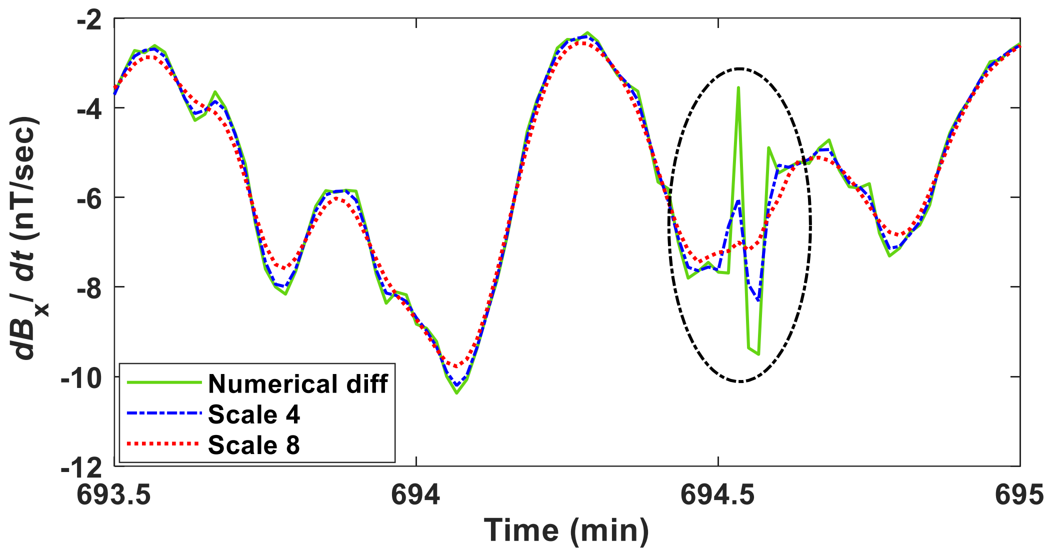

Figure 2-16: Effect of the scale parameter on smoothing dB_x/dt.

According to Table 2-2, the B_x signal captured by the magnetometer at Yellowknife station includes significant noises. Time derivate of the processed B_x signal that is obtained by the wavelet differentiation method is plotted versus numerical derivative of the original B_x signal in Figure 2-17. The derivative of the original signal is not interpretable due to the amplified noise, whereas the noises are considerably mitigated in the derivate of the processed B_x signal. This implies the importance of processing the *B* signals prior to the implementation of the GIC calculation method.

2.4.1 A Discussion on the Sampling Frequency

Both numerical and wavelet differentiation methods approximate the time derivative of the signal. Accuracy of this approximation is dominated by the sampling frequency or the time difference between two successive samples Δt. Sampling frequency is required to be a sufficient high multiple of the highest frequency component of the signal to ensure the accuracy of the approximation. A Fourier analysis reveals that main frequency

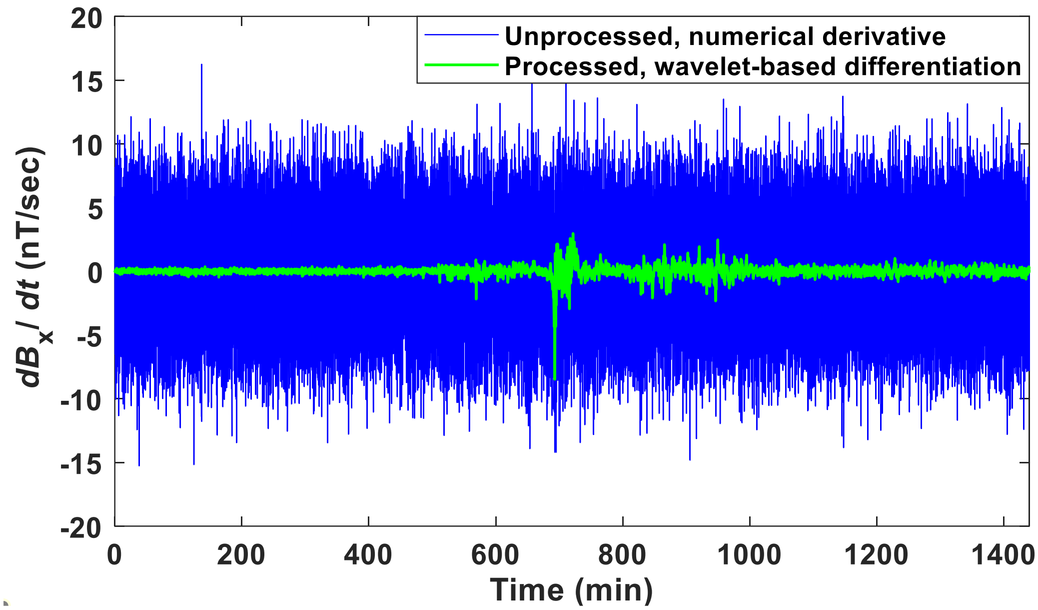

Figure 2-17: Performance of the proposed signal processing method on the time derivative of B_x signal recorded at Yellowknife station.

components of the *B* signals recorded on 2015/08/15 are less than 1 mHz. On the other hand, sampling frequency F_s of 1 Hz for the B components is not always available due to practical limitations concerned with transmitting the measured B data. Therefore, the relationship between the sampling frequency and accuracy of the differentiation is assessed in detail in this subsection. It is worthwhile to mention that accuracy of the differentiation is defined as deviation in the peaks' amplitude from the reference values, since GIC is directly proportional to the peaks' amplitude of the dB/dt signal. According to the Nyquist sampling rate theorem, sampling frequency F_s should be at least twice f_{max}, i.e., highest frequency component available in the signal, to avoid aliasing. Nevertheless, this criterion does not satisfy accuracy of the differentiation methods. A quantitative analysis is presented in the following to evaluate the relationship between F_s and f_{max}.

A simple noise free sine function is defined as $y(t) = 10\sin(2\pi f t)$ where f is the frequency of *y* signal. Unlike the *B* signal where its reference derivative signal is not available, the reference values for time derivative of y signal are simply obtained by taking derivative of *y* function as dy/dt.

The peaks of dy/dt are compared with peaks of $\Delta y/\Delta t$, i.e., numerical derivative of *y*, in terms of DPA percentages in Table 2-4 for different ratios of $R = F_s/f$. Based on the results reported in Table 2-4, DPA is less than or equal to 2% for *R* values greater than 18. Having this value of DPA as the limit, sampling frequency of the *B* signal should be at least 18 times higher than its main frequency component, i.e., 1 mHz. This limitation ensures that the peaks' amplitude is preserved in the derivative signal. Therefore, the minimum acceptable sampling frequency for the *B* signals is approximately 18× 1 mHz. Assuming $1/60$ Hz as the base sampling rate, the minimum sampling frequency can be rewritten as $1/60 \times 1.1$ Hz.

The *B* signal has two major differences with the simple *y* signal. First, the *B* signal contains various frequency components, and the latter is the presence of noises in the *B*. As mentioned earlier, the maximum frequency component of the *B* signals is less than 1 mHz. According to Table 2-4, lower frequency components affect DPA less given a constant sampling rate. In this regard, DPA reaches a value less than the 2% limit if the major frequency component equals 1 mHz or less. The latter difference, which is the noises in the *B* signal, is controlled by the scale parameter of CWT that is applied for the differentiation. As mentioned earlier, an increased scale value mitigates the noises, whereas affects the peaks by increasing DPA. Sampling frequency plays a significant role in the DPA improvement. This role is analyzed quantitatively in the following.

The derivative of *y* signal with *f* equals 1 mHz is obtained by both the CWT method and by dy/dt for different sampling frequencies, and the corresponding DPAs are listed in Table 2-5. Note that DPA in this case is calculated by (10) where x_n denotes dy/dt. As it can be inferred from Table 2-5, DPA is directly proportional to the scale parameter of CWT for a given sampling frequency. On the other hand, oversampling prevents the differentiation to cause a noticeable DPA. According to Tables II and III, a scale of 8 is the optimum condition for denoising the *B* signal to an acceptable level. This requires the sampling rate to be at least $1/60 \times 4$ Hz to ensure DPA becomes less than the predetermined value of 2%.

The sampling frequency needs to be determined with respect to the dominant frequency component of the *B* signal as well as the scale parameter of CWT. These two factors impose a minimum F_s requirement equal to $1/60 \times 1.1$ Hz and $1/60 \times 4$ Hz, respectively. The maximum of these two values yields the minimum acceptable F_s. Consequently, the magnetometers are required to take samples of *B* signal at least at 15 s intervals. It is worthwhile to mention that the dominant factor limiting the sampling frequency is the scale of CWT. Therefore, GMDs with higher frequencies such as the one

Table 2-4: Effect of sampling frequency on preserving peaks of dy/dt.

Case	*R*=F_s/f	DPA (%)
1	8	9.97
2	12	4.51
3	14	3.32
4	16	2.55
5	18	2.02
6	20	1.64

occurred in March 1989 with a frequency of 1.2 mHz [47] can be accurately modeled by sampling B signal at a rate of 1/15 Hz.

As a comparison between the numerical and the wavelet differentiation methods, case number 4 in Table 2-4 has a frequency ratio approximately the same as the first three cases in Table 2-5 with $F_s/f = (1/60)/(1 \times 10^{-3})$. The numerical differentiation method, however, yields a DPA of 2.55%, whereas DPAs for the wavelet differentiation method range from 0.79% to 17.24% depending on the scale parameter. This implies superiority of the wavelet differentiation method over the numerical differentiation in case an appropriate value for the scale parameter is chosen.

2.5 Results

A noise and spike free dB/dt signal allows accurate calculation of the GIC flowing through the power grid. An earth model as well as details of the power grid are required to obtain

Table 2-5: Effect of the scale parameter on preserving peaks of dy/dt.

Case	F_s (Hz)	Scale	DPA (%)
1	$1/60$	2	0.79
2	$1/60$	4	4.27
3	$1/60$	8	17.24
4	$1/60 \times 2$	2	0.22
5	$1/60 \times 2$	4	1.49
6	$1/60 \times 2$	8	6.45
7	$1/60 \times 4$	2	0.05
8	$1/60 \times 4$	4	0.27
9	$1/60 \times 4$	8	1.15

the GIC amplitude. The processed dB/dt signal can be applied to the earth models for different geographical zones to obtain the induced geoelectric field on the earth's surface in the corresponding regions. Given a multi-layer earth model and the earth transfer function $C(\omega)$, the induced geoelectric field is calculated as follows in time domain [24]:

$$E_x(t) = c(t) * \left(\frac{dB_y(t)}{dt}\right) \tag{2.18}$$

$$E_y(t) = -c(t) * \left(\frac{dB_x(t)}{dt}\right) \tag{2.19}$$

where E_x and E_y represent the northward and eastward components of the geoelectric field, respectively. These two components are calculated based on both the processed and unprocessed *B* data that have been recorded at the Yellowknife station, and the results are compared in Figure 2-18. As expected, the noises and spikes in the B_x and B_y signals are reflected in the geoelectric field components. Nevertheless, effectiveness of the proposed signal processing methods is verified in Figure 2-18 by a significant reduction in the noises as well as preserving the peaks' amplitude.

The usual IEEE test cases are not suitable for the GIC calculations, since they lack necessary data required to model GIC in the grid. A modified IEEE 118-bus system is introduced in [26] that incorporates additional data into the usual IEEE test case including lines length, tower configuration, conductor type and its zero-sequence impedance, transformer data, updated generator data, and GPS coordinates as well as grounding impedance of the substations. These data allow calculating semi-dc current flowing in the power grid through the ground connections.

In this research, the modified 118-bus benchmark system is applied to verify the effectiveness and accuracy of the proposed signal processing method. The block diagram in Figure 2-19 shows processing of the *B* signal step by step followed by a power system analysis. The *B* signal recorded at Yellowknife station on 2015/08/15 is considered for the GIC calculation verification. The geoelectric fields induced by both the processed and unprocessed *B* signals are obtained, and the corresponding GICs in the power grid are calculated. The GICs in the neutral connection of the grid's power transformers are ranked based on their magnitude. The simulation results revealed that the highest GIC

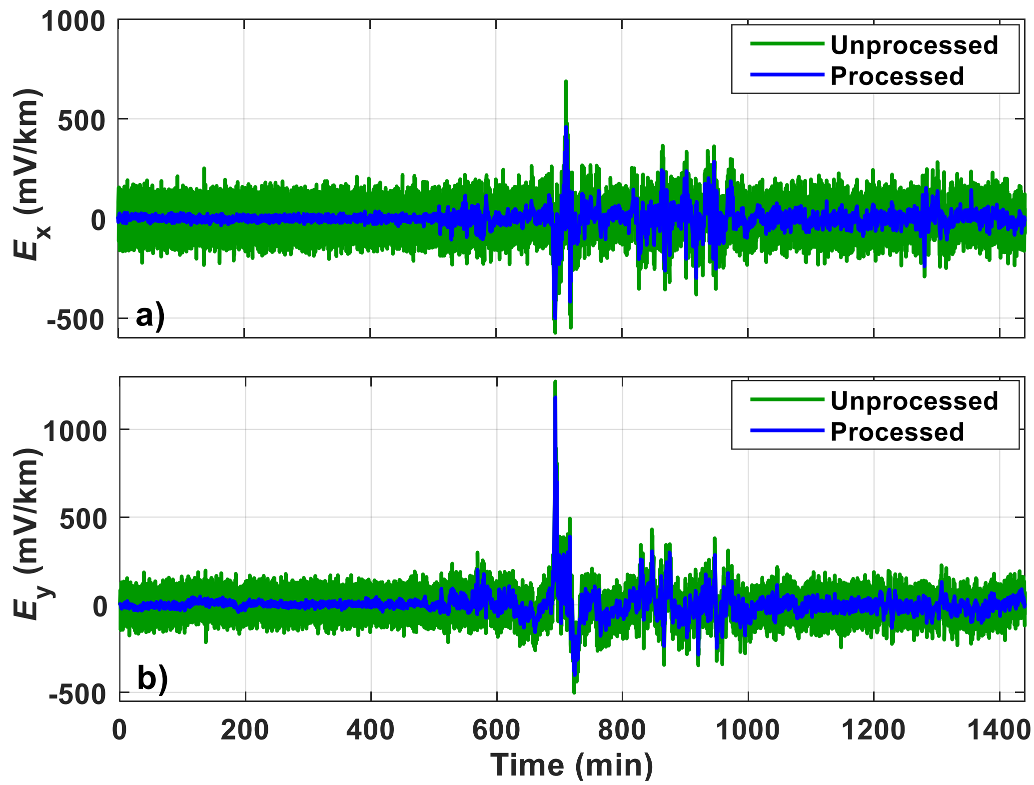

Figure 2-18: Electric field components calculated for Yellowknife station; (a) E_x; (b) E_y.

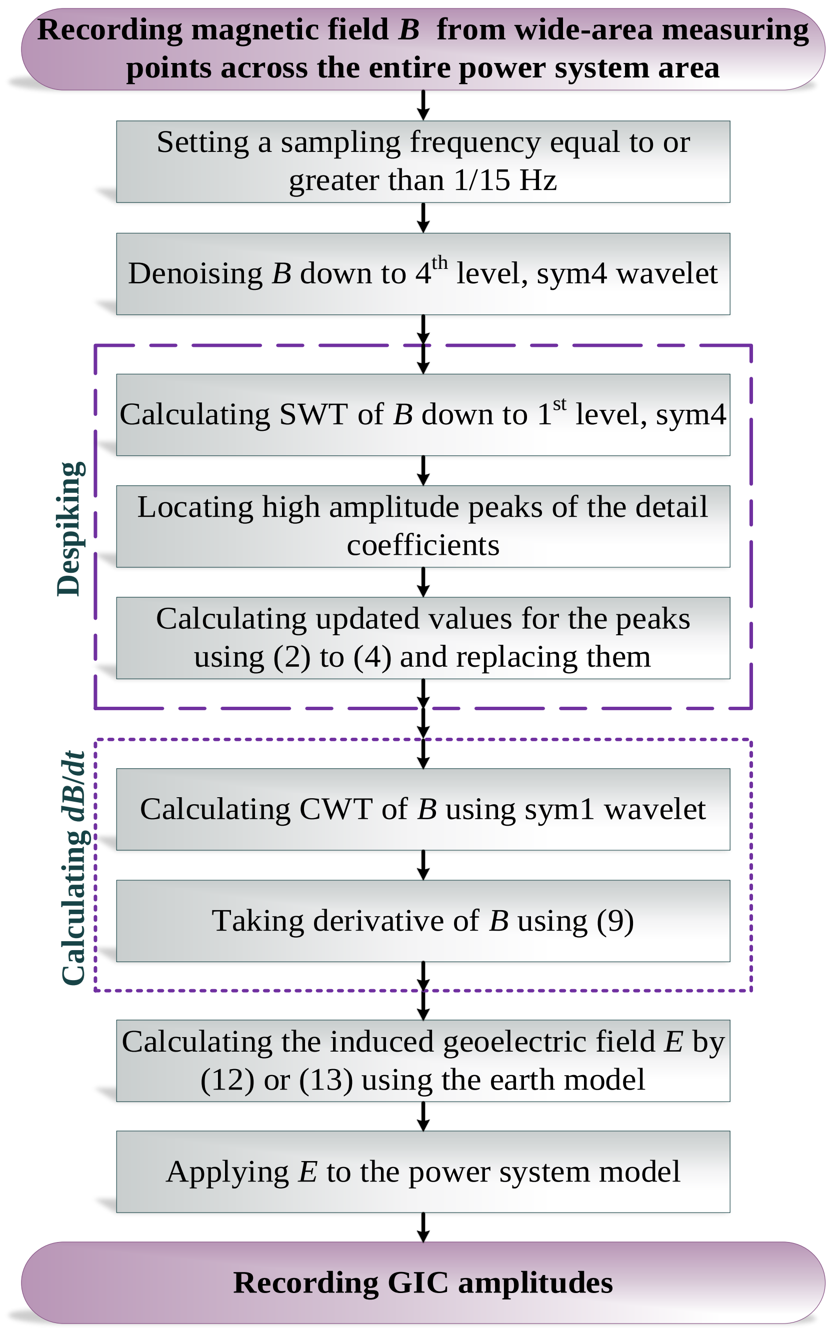

Figure 2-19: Wide-area GIC calculation algorithm.

magnitude appears on the transformer installed on bus number 24. The simulated GICs on this bus are depicted in Figure 2-20. As it can be seen, processing the *B* signal has caused a significant improvement in the accuracy of the obtained GICs by mitigating the noises and the spikes. To cite an instance, magnitude of the first and the second ranked peaks in the unprocessed GIC signal is decreased by 13% and 42% respectively, compared with the corresponding peaks in the processed GIC signal.

GIC can cause half-cycle saturation of the power transformers. Unprocessed B signals overestimate the GIC amplitude as it can be seen in Figure 2-20. This leads to a false diagnosis of half-cycle saturation in several power transformers. The inevitable countermeasures taken in response to the saturation leads to a cascade outage of several transformers and finally a blackout. This implies the importance of accurate GIC calculation in power system resiliency analysis during a GMD event.

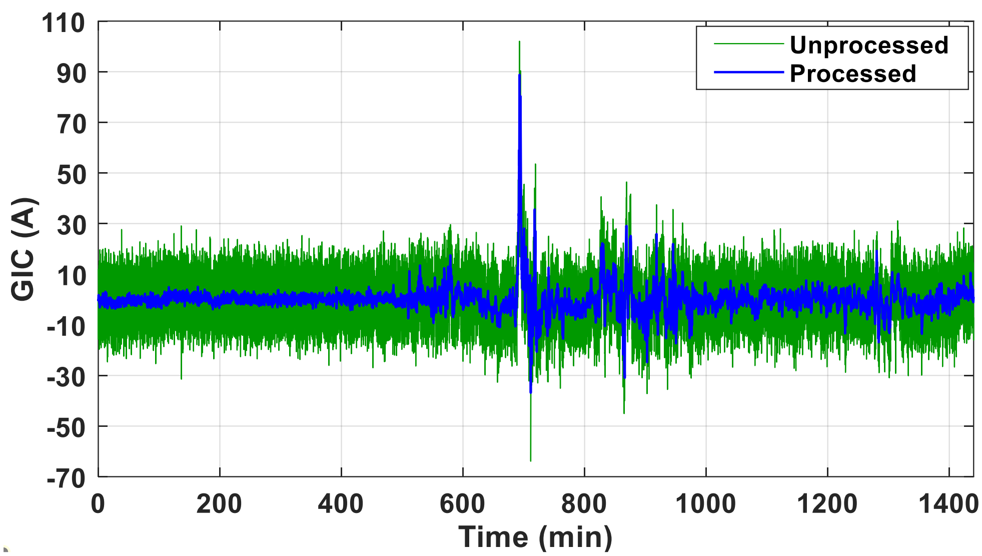

Figure 2-20: GIC amplitude on bus 24 associated with the Yellowknife *B* data.

2.6 Conclusion

An acceptable level of noise reduction is achieved by decomposing the *B* signal down to 4^{th} level using sym4 wavelet and shrinking the coefficients that are associated with the noises. The detail coefficients that are obtained in the first level of the decomposition are outstanding indicators of the spikes in the signal. In the proposed despiking method, only the spike's peak and the adjacent samples are replaced, and the remaining data points are remained unchanged.

CWT is proposed as a method to calculate time derivative of the *B* signal. The major advantage of the wavelet-based differentiation method is that a noise mitigation process is incorporated into the differentiation. The noise mitigation is controlled by the scale parameter of the CWT. Even though a scale value of 8 satisfies the noise reduction, the *B* signal is required to be sampled at a maximum interval of 15 s to ensure that the modification in the peaks' amplitude of dB/dt is negligible.

The proposed signal processing methods are applicable to the *B* signals recorded at different observatories. Therefore, the processing methods can be incorporated into an integrated wide-area magnetic field monitoring system. Monitoring the magnetic field yields dB/dt for accurate calculation of GICs. This allows resiliency analysis of the power system when several power transformers are prone to half-cycle saturation due to the quasi-dc GICs.

Chapter 3

Online Monitoring of Magnetometer Signals for Estimating Induced Electric Fields in Power Systems

3.1 INTRODUCTION

Powerful solar activities that are followed by CME cause a change in space weather. If the erupted plasma takes the earth's path, it interacts with the earth's magnetic field and leads to a GMD. As a result, quasi-dc currents with an amplitude in the order of millions of amperes known as auroral electrojets are formed in the ionosphere layer at an altitude about 100 km above the earth's surface [4, 64]. These time-varying high amplitude currents induce a magnetic field that interacts with the earth's magnetic field. Ultimately, an electric field is induced near the earth's surface.

The induced electric field causes a quasi-dc current known as GIC to flow through a closed loop in a power system [31-33]. This closed loop is comprised of power system transmission lines, grounded neutral of transformers, and earth layers. GICs affect power transformers by introducing a dc flux that can cause half-cycle saturation of the transformer core [18, 19]. The detrimental effects of the half-cycle saturation include the generation of harmonic components [20], overheating and bubble formation in oil insulation, and an increase in reactive power consumption [1, 21, 22]. An accurate calculation of the induced electric field, and therefore, the GIC flow in a power system is required to prevent the damages caused by a GMD event. The first step in calculating the induced electric field signal E is to gather magnetic field data measured near earth's surface.

INTERMAGNET, US Geological Survey, SuperMAG, and IMAGE are among the prominent networks that monitor earth's magnetic field at various observatories [65]. The INTERMAGNET observatories are equipped with fluxgate magnetometers that record magnetic flux density B signals at 1 Hz [17]. The fluxgate magnetometers are designed to either have orthogonal or parallel excitation [66] and can work either in fundamental- or second-harmonic mode [67]. Reviewing the data in INTERMAGNET database in [16] reveals a diversity in quality of the B signals recorded by the fluxgate magnetometers. The noises in the magnetic field data and therefore, the estimated GICs hinders a reliable online assessment of power system during a geomagnetic storm. A study in [65] has developed a setup to stream and visualize the magnetic field data; however, the processing of the measured signals is not discussed in [65].

An algorithm is proposed in an earlier study in [68] for offline processing of B signals measured at the observatory stations. However, online monitoring of the magnetic field, which is crucial to protect the power system against severe GMD events, requires online analysis of B signals. This eliminates the need to measure dc current at the neutral connection of power transformers to monitor geomagnetic disturbances [69]. Noise reduction in magnetic field signals while preserving the peak's amplitude of main frequency component with minimum possible computational burden is the novelty of the study in this chapter. This results in an accurate calculation of the induced electric field, and therefore, the GIC in the power system. To cite an instance, the quasi-dc GIC can be adopted into power transformer hot-spot temperature estimations. An accurate GIC amplitude allows determining whether the transformer is operating under emergency loading conditions [70] or approaching the critical level of bubble generation [71] and failure.

In this chapter, a set of signal processing methods are integrated to develop an online monitoring system for the magnetic field signals. Denoising the B signals is studied in Section 3.2, followed by estimating dB/dt in Section 3.3. A procedure is presented in Section 3.4 to enhance the SNR by updating the processed data points followed by a discussion on the processing times in Section 3.5. The sample magnetic field signals analyzed in this study are derived from the INTERMAGNET database [16].

3.2 Denoising Magnetic Field Signals

Several observatory stations worldwide are equipped with magnetometers to measure three magnetic field components, B_x, B_y, and B_z. Parameters measured by sensors and transferred by electrical circuits are not immune to noises. It also applies to sensitive magnetometers that measure low amplitude magnetic flux density. The noises can be categorized into three sections, including ambient, external, and internal noises. The ambient noises originate from temperature changes [72] and nearby magnetic or large electric fields [73]. The external noises arise from auxiliary circuit components, e.g., amplifiers [41, 42]. The measurement mechanism of magnetometers leads to the third category of the noises, i.e., internal noises. Low frequency noises that are inversely proportional to frequency in magnetoimpedance [40, 44, 45] and fluxgate sensors [42] and Barkhausen noises in magneto-impedance sensors [43] are among the prominent sources of the internal noises. The importance of noise reduction is more noticed considering that the time derivative of magnetic field signals dB/dt is incorporated in the E signal calculations.

The online and offline magnetic field monitoring systems are distinct because of the pivot role of a sliding window in the online monitoring. A sliding window of a particular width is considered for each step of processing the magnetic field signals B. The window's width is kept constant, but once a new sample is received, the sliding window is shifted to include the most recent data and form an updated B signal. Note that only the data points that are encompassed in the sliding window are processed.

The first step towards processing the data within each window is to denoise the B signal using a discrete wavelet transform. The B signal is projected onto a mother wavelet and then decomposed down to a specific level. The coefficients associated with noises are shrunk, and the signal is reconstructed afterward. The reader may refer to [74] for details of a wavelet transform. It is worthwhile to mention that the signal within each window is extended by three samples using linear extrapolation. The extended length of the signal enhances the effectiveness of an online wavelet denoising method by adding to the right margin of the window.

Three parameters, including mother wavelet, decomposition level, and window size, dominate the denoising process. It becomes complicated if the impacts of all three parameters are evaluated simultaneously. Hence, the window size and wavelet denoising parameters are analyzed in two separate categories. The optimum combination of these three parameters is expected to extract the most noise components from the B signal. Different combinations are compared with each other in terms of SNR in dB by:

$$\mathrm{SNR} = 10 \log_{10}\left(\frac{P_{signal}}{P_{noise}}\right) \tag{3.1}$$

The measured B signal contains magnetic field data together with noises as follows:

$$B_{measured} = B_{noise} + B_{main} \tag{3.2}$$

P_{signal} in (1) is the power of B_{main} that is obtained by denoising the measured signal. $B_{measured}$ is applied to a low-pass filter to extract B_{noise} by deducting the filter's output, i.e, B_{main}, from the measured signal. A low-pass Butterworth filter with a cutoff frequency of 20 mHz is designed to filter $B_{measured}$. The rationale behind this cutoff frequency is that earlier studies in [35, 47] detected the primary frequency component of severe GMD events in a range of 1 to 3 mHz. In conclusion, SNR can be calculated by replacing P_{signal} and P_{noise} in (1), which are obtained by wavelet denoising and the low-pass filter, respectively. Note that the designed low-pass filter and SNR calculations are not elements of the online monitoring system. SNR is only calculated to detect the best approach toward denoising the magnetic field signals and evaluate their efficacy.

3.2.1 Properties of Wavelet Denoising Method

The proposed signal processing methods are required to be evaluated by applying them to several measured B signals. GMDs cause a more severe GIC in regions located at high latitudes including North America and Nordic countries [75]. In this regard, five observatory stations that span from the east to west coast in North America are considered to evaluate the online monitoring system in this chapter. The magnetometers installed at each observatory record the B signals with distinct qualities, which allows creating a diverse database.

In this subsection, the proposed signal processing methods are implemented on a B

signal recorded at Yellowknife station on 2015/08/15 during a GMD event. All components of B signals, i.e., B_x, B_y, and B_z, are available in the INTERMAGNET database [16]. The Yellowknife station is the center of focus in this subsection as the worst-case scenario due to its poor signal quality among others as discussed later.

Symlet and Daubechies wavelet families are widely used for denoising signals. The window size is set to 128 samples to denoise the B_x signal online with mother wavelets from different members of these two families. The decomposition level for the wavelet denoising ranges from 2 to 5. SNR values for both B_x and dB_x/dt signals are listed in Table 3-1 for a few cases. Note that the induced electric field due to a GMD is calculated based on dB/dt instead of B signal. Hence, it is desirable to maximize SNR for dB/dt signal. As it can be seen in Table 3-1, denoising B signals with *db4* wavelet at a decomposition level of 4 results in the highest SNR for dB_x/dt signal. This condition is consistent for dB_y/dt and dB_z/dt signals as well. The mother wavelet and decomposition level of the wavelet denoising method were determined assuming the sliding window encompasses 128 samples. The next step is to evaluate SNR for different window sizes to detect the optimum window width for the online denoising of B signals.

Minimum window width (WW) is dominated by the decomposition level (DL) of the wavelet transform such that [50]:

$$\mathrm{DL} \leq floor(\log_2(\mathrm{ww})) \tag{3.3}$$

This limitation on the window width is due to downsampling after the signal decomposition. Since the B signal is decomposed down to level 4, the minimum window width equals 16. On the other hand, optimizing the calculation speed requires the window

Table 3-1: Denoising the B_x signal recorded at Yellowknife station.

Wavelet	Level	SNR of B_x (dB)	SNR of dB_x/dt (dB)
Non denoised signal		54.31	-19.05
db2	4	54.29	-7.53
db3	4	54.32	-6.35
db4	3	54.31	-6.92
db4	4	54.31	-5.52
db4	5	54.31	-6.46
sym3	4	54.32	-6.35
sym4	4	54.34	-5.91
sym4	5	54.38	-6.69

size to be a power of two. In this regard, the B signal recorded at the Yellowknife station is denoised with *db4* wavelet at a decomposition level of 4 with various window widths. The corresponding SNRs are listed in Table 3-2. Although SNR of B signal is kept almost at the same level with an increased window width, SNR of db_x/dt has improved significantly. However, increasing window width beyond 128 results in a slight improvement in SNR. On the other hand, the calculation burden is increased with widening the window. Therefore, a window width of 128 is the optimum size for the online wavelet denoising. The effect of the wavelet denoising method is illustrated in Figure 3-1 for the B_x signal recorded at the Yellowknife station.

3.3 Derivative of Magnetic Field Signals

Earlier studies in [35, 76] applied finite difference methods (FDM) to calculate dB/dt

Table 3-2: Evaluating changes in the SNR due to an increased window width.

Window width	SNR of $B_{x,denoised}$ (dB)	SNR of $dB_{x,denoised}/dt$ (dB)
16	54.32	-10.00
32	54.27	-7.32
64	54.29	-6.01
128	54.29	-5.52
256	54.29	-5.36
512	54.29	-5.31

signal. The difference between the amplitude of two consecutive samples is multiplied by the sampling frequency in these methods. Although the finite difference methods are simple to implement and require minimum computation, the noises are significantly amplified in the derivative signal. An alternative approach based on CWT is applied for offline studies in [68] to mitigate amplified noises in dB/dt signal. This method yielded promising results, and therefore is adopted for online estimation of dB/dt as well. However, this method requires modifications to be adapted for the online signal processing. Moreover, the severe detrimental effects of GICs in a power transformer occur during the storm maxima. Therefore, the aim is to improve SNR of dB/dt while preserving the peak's amplitudes.

The first step in estimating dB/dt signal is to calculate CWT of all samples of B signal within each window by (2.11) followed by calculating *K* constant using (2.12) and (2.13). Finally, derivative of B signal can be estimated by (2.15). It is demonstrated in [68] that a dilation parameter of 8 can mitigate the noises in the derivative signal while preserves peaks amplitude throughout the signal.

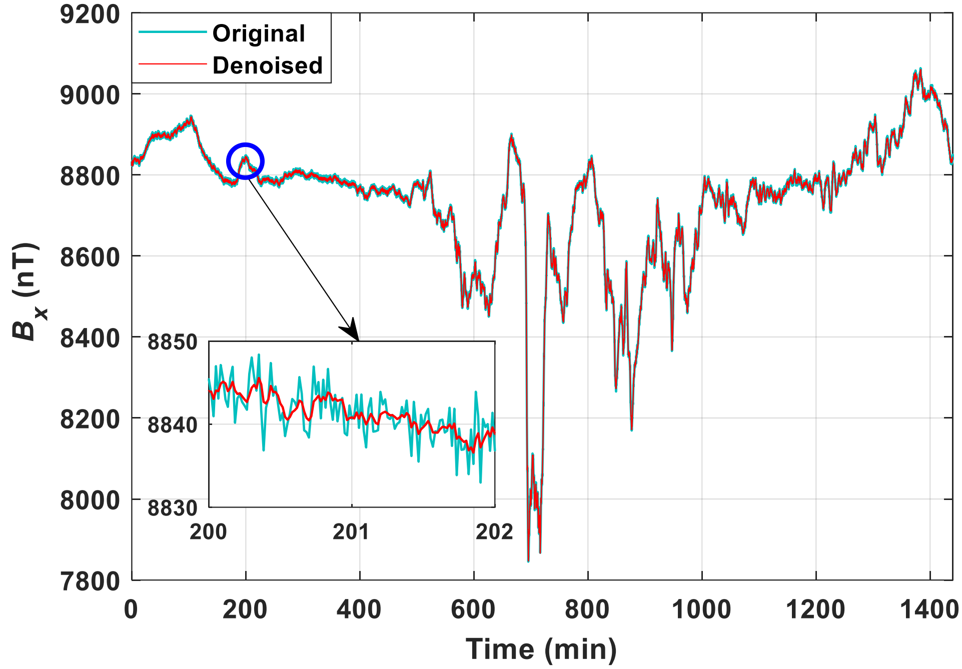

Figure 3-1: Original and denoised B_x signal recorded at Yellowknife station.

The wavelet-based derivative (WBD) method applied for offline studies in [68] needs to be modified for online calculation of dB/dt signal. It is demonstrated in Section 3.2 that the Daubechies wavelet family is more effective in the SNR improvement compared with the Symlet wavelet family. Therefore, the sym1 wavelet used for offline studies in [68] is replaced with db1 wavelet to estimate dB/dt online. Furthermore, two factors including the width of the sliding window and transients that are introduced to the dB/dt signal due to the CWT are required to be analyzed. Denoising and taking derivative of B signals are two separate processes, and a sliding window with a distinct width can be applied for each method.

A minimum of four B signal samples is sufficient to estimate dB/dt by a CWT as represented in (7). Nevertheless, the window width is required to be extended by at least three samples on the right side to compensate for the transients introduced by the CWT.

On the other hand, a power of two number of data points ensures an optimized computational speed. Therefore, the sliding window for estimating dB/dt encompasses eight samples in total. The first five samples are measured magnetic field data, and a linear extrapolation obtains the three remaining data points.

B_x signals recorded at five stations on 2015/08/15 are considered to compare efficacy of the online and offline processing methods. Three sets of $(B_x, dB_x/dt)$ signals are created for each station. These three signal sets represent unprocessed, online processed, and offline processed [68] signals. Derivative of the unprocessed B_x signals are estimated by [77] forward FDM:

$$\left.\frac{dB_x}{dt}\right|_i = \frac{B_x[i+1] - B_x[i]}{h} \tag{3.4}$$

and central FDM:

$$\left.\frac{dB_x}{dt}\right|_i = \frac{B_x[i+1] - B_x[i-1]}{2h} \tag{3.5}$$

where h denotes the time step. SNRs are calculated for each signal set, and the results are listed in Table 3-3. It can be inferred from Table 3-3 that both online and offline processing methods improve SNR of dB_x/dt signal significantly. Although the online method provides a lower SNR in dB_x/dt in general compared with the offline method, the difference in the SNRs is negligible in most cases. Moreover, The FDMs fall behind the wavelet-based method in noise reduction capabilities. The improvement in the SNR is illustrated in Figure 3-2 for the magnetic field signal recorded at the Yellowknife station. It can be seen in this figure that how online denoising of the B_x signal prior to the differentiation and choosing WBD over the FDM cause a significant reduction in the noises.

3.3.1 Induced Electric Field

A schematic of the series of events that lead to generation of GICs in a power system is shown in Figure 3-3. Powerful solar storms emit plasma from the sun's surface. If the plasma takes the earth's path, electrojets are formed in the ionosphere layer and create a time varying magnetic field, which interacts with the earth's magnetic field [4]. An electric field is induced as a result, and therefore, GIC flows in the power system through transmission lines and the ground connection of power transformers.

E_X and E_y are the two components of the induced electric field in earth layers that are calculated by (2.18) and (2.19). The reader may refer to [35] for a detailed discussion on how earth transfer function $c(t)$, is obtained by measuring the impedance of different earth layers. The magnetic field data recorded at the Yellowknife station are convolved with the impulse response of earth layers of Ontario, Canada, to calculate E_x and E_y. The electric field signals calculated based on non-denoised B and FDM methods are

Table 3-3: A comparison among SNR of unprocessed, online processed and offline processed magnetic field signals.

Station	SNR (dB)						
	B_x	B_x, offline denoised	B_x, online denoised	dB_x/dt, unprocessed, forward FDM	dB_x/dt, unprocessed, central FDM	dB_x/dt, offline, wavelet-based	dB_x/dt, online, wavelet-based
Yellowknife	54.31	54.41	54.31	-19.49	-14.24	-0.69	-0.75
St John's	81.41	81.45	81.32	-11.04	-8.38	-2.81	-3.12
Sitka	58.63	58.68	58.61	-14.32	-10.19	-3.78	-7.58
Iqaluit	52.98	52.99	52.96	-2.57	-2.55	-2.43	-2.42
Fort Churchill	54.15	54.15	54.13	-1.94	-1.86	-1.66	-1.64

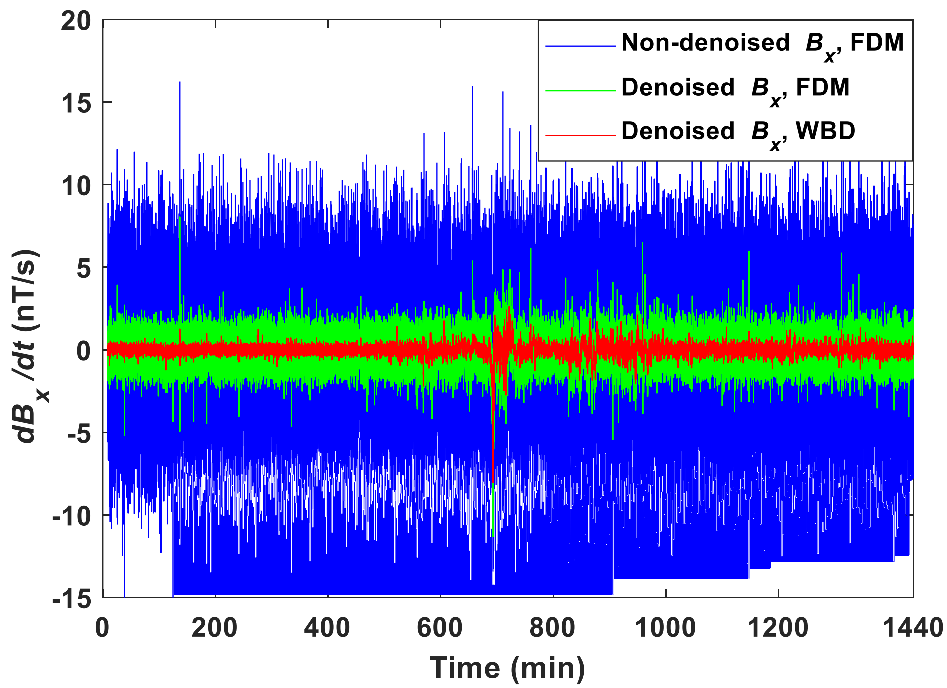

Figure 3-2: Progressive reduction of noises in dB_x/dt due to denoising and applying WBD method.

compared with those obtained by denoised B and WBD method in Figure 3-4. Decreasing the noises beyond this level in the online studies requires further analysis that is described in the following section.

3.4 Updating Historical Data Points

The data points contained in the sliding window are updated once a new sample is recorded and transferred to the processing unit. All of the data points in the window are considered in the calculations. Hence, the number of times each data point is processed equals the window width. To cite an instance, the window width for the wavelet denoising

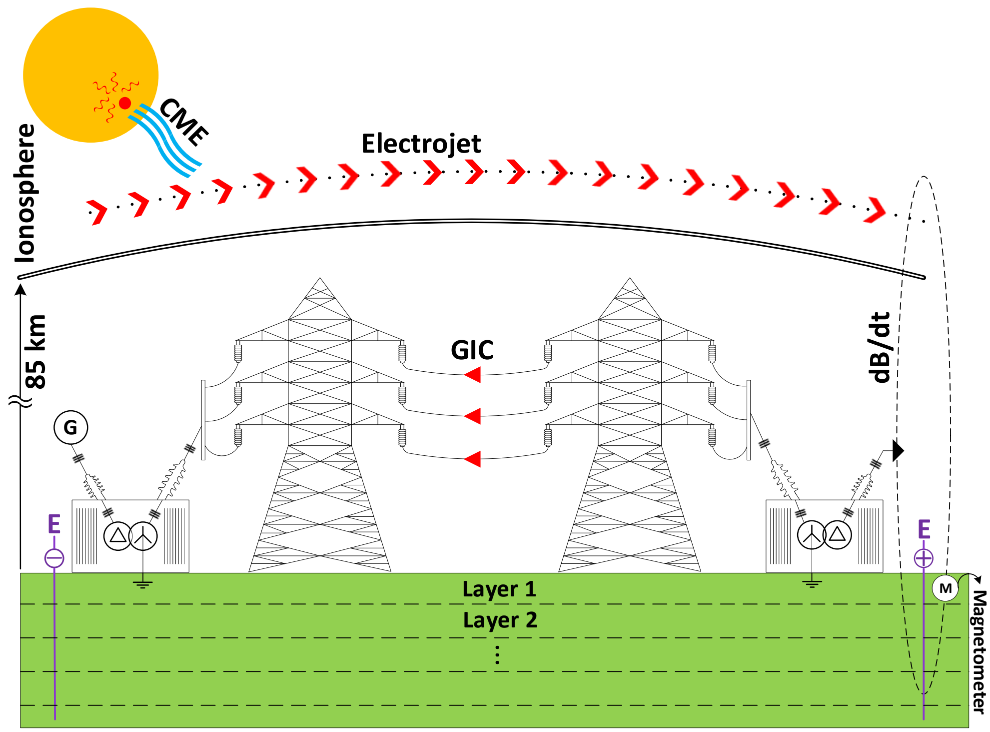

Figure 3-3: Schematic of GIC flows in a power system during a GMD event.

is 128, which implies that each sample is processed 128 times before falling behind the sliding window. In this regard, the previously processed data can be updated to enhance the noise reduction capability without an additional processing step.

When a new sample of B signal is received, it can only be compared with the previous data, which adversely affects the noise suppression and outlier data detection. In this regard, in addition to the online processing of B signals, the previously stored data are updated as well. The updating process is explained in detail as follows. Assume the sliding window has a width of 128. When a new sample is received, it is attached to the right side of the window, and one data point is removed from the left side of the window. The data points within the sliding window are denoised, and then the last denoised data

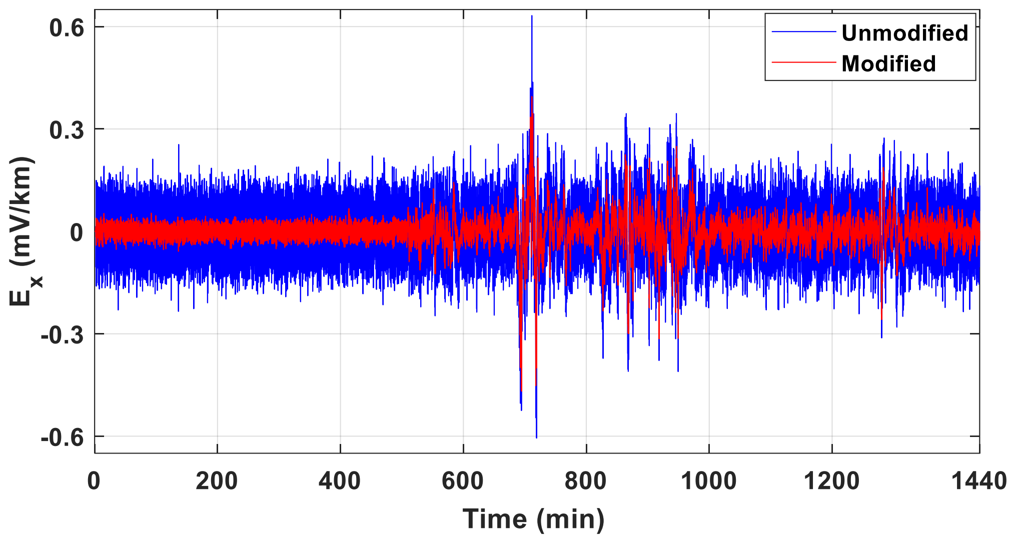

Figure 3-4: Improvement in quality of the induced electric field data due to denoising B signal and choosing WBD over FDM in calculating dB/dt.

point is stored as a result of the online processing. A number of recently processed data points referred to as lag is considered to replace the previously stored processed data. The lag indicates the processed data within the sliding window that are located in a position ranging from $window\ width - 1$ to $window\ width - lag$. Hence, the number of times each processed data point is updated equals the lag value. A schematic of the updating process is illustrated in Figure 3-5 for a window width of 128.

The improvement in SNR of the numerical derivative of denoised magnetic field signal caused by updating the historical data is investigated under different circumstances. The B signal recorded at the Yellowknife station on 2015/08/15 is denoised using four distinct sliding windows with a width of 8, 32, 64, and 128. A lag ranging from $window\ width - 1$ to $window\ width - lag$ is introduced to each sliding window, and the historical data are updated accordingly. The resultant denoised signals are passed through a low pass filter,

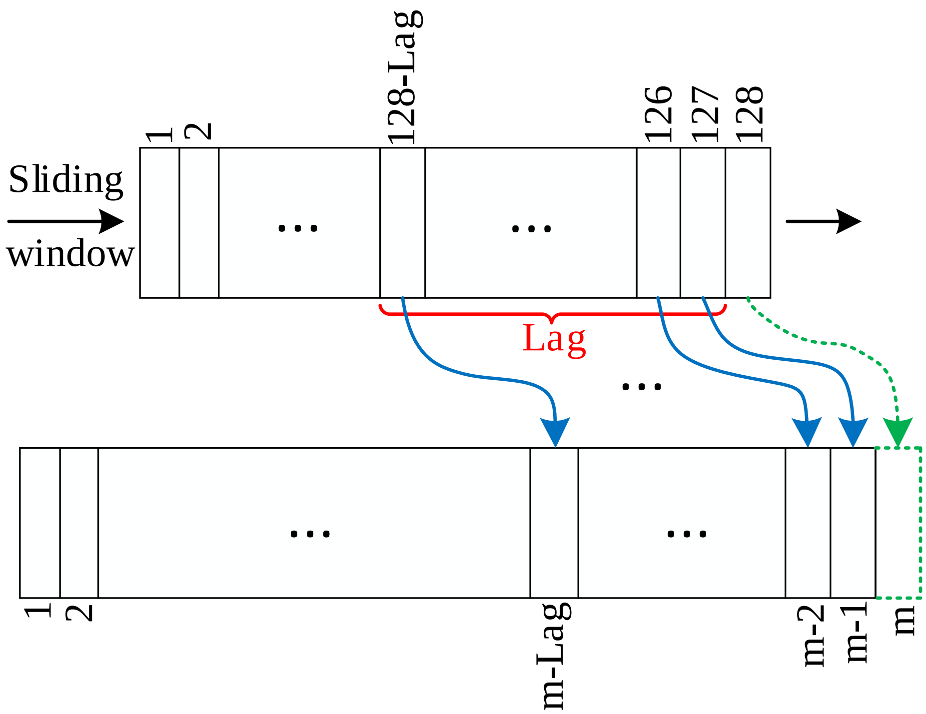

Figure 3-5: Updating and replacing previously processed data points.

as discussed in Section 3.2, to calculate the SNR. The results are shown in Figure 3-6 for different values of window widths and lags. As it can be seen in this figure, for a window width of 128, the SNR oscillates within a limited range after the transient sharp increase in the SNR settles down. This oscillatory behavior is emerged when the lag reaches about ten samples and is faded when the lag comes close to the window width. This behavior is scrutinized as follows.

As it was mentioned in Section 3.2, the part of B signal that is included in the sliding window is linearly extrapolated by three samples. These three samples are replaced by actual measured B data by introducing the lag to the sliding window. Moreover, increasing the lag value beyond three samples provides the updating process of the denoised signal with more data points. As a result, frequency contents of B signal samples within the

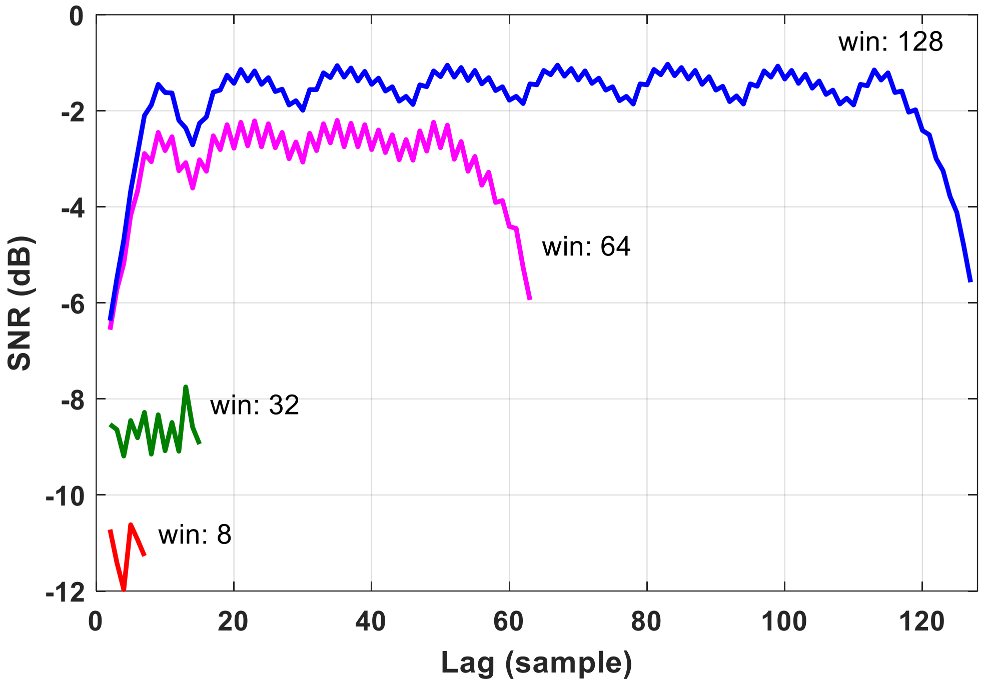

Figure 3-6: Variations in SNR of dB_x/dt due to updating previously processed data points.

sliding window are preserved. As it can be seen in Figure 3-6, when the sharp increase in the SNR decays, SNR oscillates within a limited range. The reason for this oscillatory behavior is that for a particular value of lag, some frequency components are amplified, and some are attenuated. B signals recorded at different observatories were analyzed, and it was discovered that the first peak of SNR occurs when the lag takes a value of about ten samples.

Given a lag of ten samples, the width of the sliding windows for all the processing methods needs to be long enough to allow updating the historical data. Hence, except for denoising the B signals that requires a sliding window of width 128 samples, the sliding windows for estimating dB/dt and the induced electric fields need to contain 16 samples.

Note that a width of eight samples was proven to be enough for the sliding window applied in calculating dB/dt. This width has to be increased to encompass at least ten samples. Considering that the number of data points is needed to be a power of two for an optimized computational speed, the width of the sliding window is set to sixteen samples.

The increase in the SNR of the electric field signals due to applying a lag of ten is illustrated in Figure 3-7(a). The E_x signals shown in this figure pertain to the B signals recorded at the Yellowknife station. As it can be seen in Figure 3-7(b), the noises are

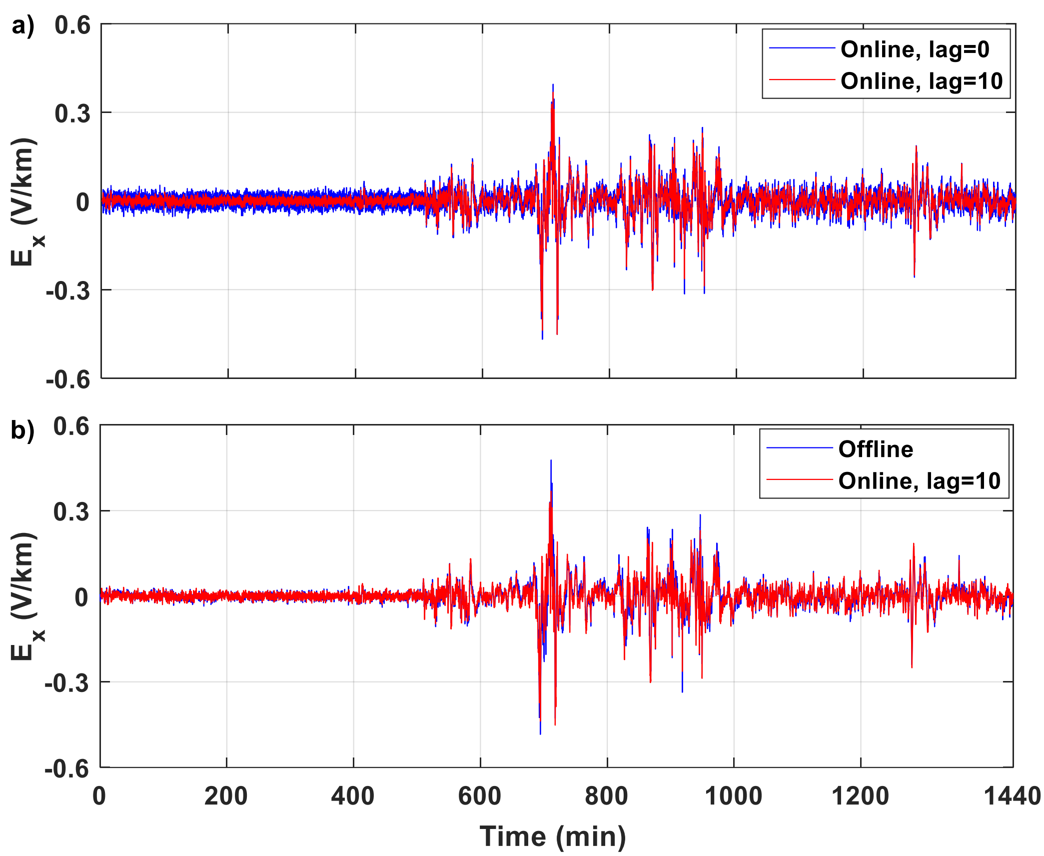

Figure 3-7: Improvements in the induced electric field signal due to: (a) online processing (b) updating historical data points.

reduced to the extent that is comparable to the E_x signal obtained by the offline method in [68].

3.5 Processing Speed

Magnetometers can sample at a rate of several kilohertz [78]; however, the observatory stations are equipped with fluxgate magnetometers that sample at 1 Hz [16]. The time required to process B signal data points and to calculate the corresponding induced electric field on a full window width is 2 ms and 6 ms, respectively. The processing times pertain to an Intel 1.6 GHz CPU. A total processing time of 8 ms for each cycle implies on practicality of the online monitoring system considering the 1 Hz sampling rate of B signals plus a latency for data transmission. On the other hand, the methods introduced in this chapter are based on well-known mathematical theorems. This allows easy implementation of the monitoring method in prominent coding languages with the help of built-in libraries for an optimized processing speed.

A prominent opponent of wavelet denoising is a moving average filter, which imposes a less computational burden and therefore, a faster processing speed. Three major advantages of the wavelet denoising method make it more suitable to worth the slower calculation speed. In the wavelet method, only coefficients below a threshold are shrunk [50], while all frequency components are averaged in the moving average filter. Therefore, unlike the moving average filter, the wavelet method retains peaks in the B signal that translate into peaks of GIC in power systems. Second, moving average filters replace the midpoint in a window, thus imposing a delay on the online monitoring system that is correlated to the window's width. Third, wavelet transforms are proven to outperform moving average filters in denoising the magnetic field signals. The performances of these two methods in improving SNR of forward finite difference dB_x/dt signals are compared in Table 3-4. This comparison is made based on the data recorded at the Yellowknife observatory as an example.

3.6 Conclusion

A sliding window is a dominant factor that differentiates the online processing of magnetic field signals from offline studies. The first step in the online processing of B signals is to slide a window of width 128 samples over the signal and denoise the encompassed data points down to level four by *db4* wavelet. The next step is to apply a CWT based on db1 wavelet to estimate dB/dt. The sliding window is required to include at least sixteen samples for this step. Convolution of the improved dB/dt signals with the earth's impulse response yields the induced electric fields.

The weakness of applying a wavelet transform to a sliding window is that transients are introduced at the end of the window. However, extending the signal length by a linear extrapolation is a straightforward method to overcome the transients. It was also demonstrated that updating the previously stored and modified data points can

Table 3-4: Comparing wavelet denoising and moving average filter.

Denoising method	Lag in the wavelet method	Moving average window width	SNR of dB_x/dt (dB)
Wavelet	1	NA	-6.39
Moving average	NA	3	-11.00
Wavelet	2	NA	-5.50
Moving average	NA	5	-7.21
Wavelet	3	NA	-4.70
Moving average	NA	7	-5.12

significantly increase the SNR. This enhancement is achieved by replacing the ten most recently processed data points in each sliding window. Processing magnetic field signals and obtaining the induced electric fields are fulfilled in 8 ms cycles. This time is short enough to run the online monitoring system with an input signal that is sampled at 1 Hz.

Chapter 4

Bubble Formation in Oil-Paper Insulation of Power Transformers

4.1 INTRODUCTION

Transformers are manufactured at different nominal ratings depending on their use in either distribution, transmission or generation-side levels. This section focuses on medium and large oil-immersed power transformers that typically have a rating of greater than 2500 KVA according to IEC 60076-7 [79]. Paper and oil insulation are crucial components of the power transformers. Operating limits and remnant lifetime of the transformers are determined based on the properties of their insulations and paper insulation in particular.

Thin layers of paper insulation with a thickness of a fraction of a millimeter are wound around windings of the power transformers. The oil-impregnated paper that is immersed in the insulating oil provides sufficient insulation strength that is known as turn insulation. In addition to the wrapping paper, pressboards that are comprised of several plies of paper are used as support, protection, or spacer elements [80]. Nevertheless, the thin layers of the wrapping paper herein referred to as paper insulation are more prone to aging and susceptible to excessive heating of the windings. A schematic of a typical power transformer with three windings that are immersed in insulating oil is shown in Figure 4-1.

Standards such as IEEE C57.91 [70] and IEC 60076-7 [79] propose transformer loading guides as to hottest-spot temperature (HST) to ensure a safe operation and longer life expectancy. The research in this chapter addresses a physical phenomenon known as bubble evolution, which is the main reason to prevent the transformer HST from increasing beyond the short-term emergency loading limits. This chapter addresses one of the detrimental effects of GIC flows in power transformers during a GMD event. The sharp increase in the HST of the transformers due to GICs allows formation of bubbles in the oil-paper insulation. Gaseous bubbles endanger the integrity of the insulation system. Partial discharge can develop inside sporadic bubbles. A flashover followed by a surge in pressure inside the transformer's tank is a significant concern in presence of a stream of bubbles. The influence of bubbles and their motion in decreasing oil breakdown voltage

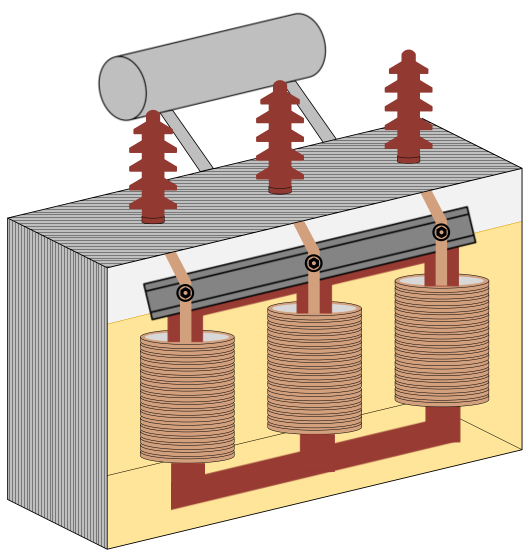

Figure 4-1: A schematic of a three-phase transformer

is studied in [30, 81].

Few recent studies in [27, 28, 82-85] developed test setups to investigate bubble formation in oil-immersed paper insulations. Results of the experiments are reflected in plots showing bubbling inception temperature (BIT) versus moisture content of the paper. Several parameters affect BITs, including the type of the paper and oil insulation, aging of the insulations, temperature rise rate, and gas content of the oil. Since the BITs are empirically derived, uncertainties are revealed by further research. To cite an instance, bubbles cannot be formed at temperature rise rates below 3 ºC/min according to [27], whereas bubbles are seen at a 2 ºC/min rate in [82]. In another instance, the researches in [82] and [27] provided contradictory results as to whether aging of the paper insulation causes reduced BITs. The reader may refer to [86] for a detailed discussion and comparison of the results reported in [27, 28, 82-85].

Besides the discrepancies among the BITs reported in [27, 28, 82-84], a lack of enough data on alternative oil and paper insulations is noticeable, as mentioned in [86]. Only two studies conducted experiments in natural ester oils [29, 83], whereas mineral oil is predominant in the other research [27, 28, 82, 84, 85]. In a similar case, only two studies considered thermally upgraded paper (TUP) [27] and aramid [85] instead of Kraft paper. A thorough search of the literature yielded that a pair of TUP-ester oil insulation is not considered in any bubble formation study.

In this chapter, three sets of experiments are conducted to investigate the bubble formation at different moisture levels and temperature rise rates in the paper insulations. The insulation pairs are Kraft paper-synthetic ester oil and TUP-synthetic ester. It is worth mentioning that these two insulation pairs are not incorporated in the BIT experiments in the literature. The experiments are conducted at two temperature rise rates including

3 ºC/min and 20 ºC/min. The results from the lower rise rate experiments are compared with those in the literature to establish reliable BITs. The results from the latter experiment at the higher rate allows assessing the condition of the oil-paper insulations at elevated temperatures due to GIC flows.

The fundamentals of bubble generation are outlined in the following section. The test setup is demonstrated in Section 4.3. Results of the experiments are presented in Section 4.4, followed by a comparison among BITs obtained in this research and those reported in the literature. A thorough discussion is presented in Section 4.5 on the differences between Kraft paper and TUP concerning bubble formation. Finally, bubble generation at high temperature rise rates are scrutinized in Section 4.6.

4.2 Fundamentals of Bubble Formation

The bubbles in oil-paper insulations are mainly formed from water vapor [28]. Water is initially available in the paper and produced as an aging byproduct inside a power transformer. Paper insulation of new transformers contains an initial moisture content of about 0.5 % [87]. The paper's aging leads to the production of water through progressive hydrolysis reactions [88, 89]. Furthermore, unsealed conservators in transformers allow ingress of moisture as well. Water molecules in the cellulose fibers of paper insulation tend to migrate to the oil as the temperature increases [90]. This migration is due to reaching an equilibrium between the oil and paper and is not necessarily detrimental to the insulation system. In this regard, the water molecules are either dissolved in the oil or settled at the bottom of the tank, depending on the water solubility of the oil. However, another condition is required for the bubbles to evolve and appear on the paper's surface.

Bubbles are known to be formed in cavities on the surface of the paper and oil container and not within the oil [28]. The bubble size grows if the internal pressure P_{int}, becomes greater than the sum of the external oil pressure P_{oil}, and surface tension σ according to [28, 91]

$$P_{int} = P_{oil} + 2\sigma/r \quad (4.1)$$

where r indicates bubble radius. The surface tension is referred to as interfacial tension (IFT) between oil and water molecules. Principles of bubble evolution are adopted to scrutinize the expected outcomes of the experiments. However, limitations of (4.1) are briefly outlined as follows. First, contaminants in the liquid, i.e., oil insulation, and surface properties such as local geometry are proven to affect tensile strength [91]. Second, this equation can only be applied to stationary bubbles on the surface of the paper insulation or free bubbles in the oil. In other words, (1) misses an important term, the interfacial tension between water and paper. The bubble is required to overcome this tension to be released into the oil. Third, the stationary bubble on the paper's surface does not have a spherical shape [92].

Ambient air pressure can be easily incorporated into (1). Thus, it is not considered a limitation herein. Nevertheless, the difference in the internal pressure of separate bubbles is not susceptible to the three previously mentioned limitations. Even though absolute values of P_{int} are not inclusive, they can be applied for comparison purposes for the same paper insulation immersed in different types of oil insulations. The effect of IFT on BIT in different oils is discussed as follows.

Shell Diala mineral oils, for example, are reported to have IFT of greater than 40 mN/m [93], which is higher than typical IFT values for ester oils. IFT values for three types of new and aged oils are measured in a study in [94] and listed in Table 4-1, along with their density. The data for aged oil is obtained after heating up the oil for 2500 hours at 115 ºC in an oven. A quantitative analysis is employed based on IFT data in Table 4-1 to compare P_{int} among different oils. Values of P_{int} are shown in Figure 4-2 for two bubble radii, 0.1 and 0.5 mm. According to Figure 4-2(a), the smaller bubble needs a higher inner pressure to grow in new mineral oil. This pressure becomes lower than that required in synthetic ester oil by an increase in depth beyond 0.3 m. Based on the calculations, synthetic ester outperforms the other two oils for a bubble radius of 0.5 mm and larger in terms of bubble evolution because a higher inner pressure is needed for the bubble to grow. Note that P_{int} can be directly related to the paper insulation BITs since the thermal energy radiated from the windings contributes to increased water vapor pressure inside the bubble.

Plots for P_{int} in the aged oils are excluded here since they follow the same trend and order as in Figure 4-2(b). Unlike the pressure lines for the new oils, the order of pressure lines does not change with increased bubble diameter for the aged oils. Synthetic ester oil ages slower than mineral and natural ester oils [95] and therefore preserves its IFT more compared with the other oils. In this regard, for the same paper insulation, a higher BIT is expected in aged synthetic oil than in aged mineral or natural ester oils.

The experiments reported in this chapter are conducted in Midel 7131 synthetic ester oil. The properties of the Midel 7131 insulation oil are listed in Table 4-2 [96] and are compared to the requirements according to IEC 61099 standard [97]. BITs are expected

Table 4-1: Interfacial Tension (IFT) for New and Aged Oils [91].

Type of oil insulation	IFT for new oil (mN/m)	IFT for aged oil (mN/m)	Density (kg/m^3)
Mineral	42	14.7	885
Midel 7131 synthetic ester	30	24	970
Midel 1204 natural ester	28	19.0	920

to be lower than those in new mineral oils for small bubbles on the surface of identical paper insulations with the same moisture content. This hypothesis is assessed later after the results of the experiments are presented.

4.3 Experimental Test Setup

The concept of the experiment is to simulate overheating in the winding of power transformers in an oil-paper insulation setting. The heating source is a 1600 W cartridge heater hanging in a glass vessel. The cartridge heater has a length and diameter of 150 mm and 16 mm, respectively. The cartridge heater used in this research is shown in

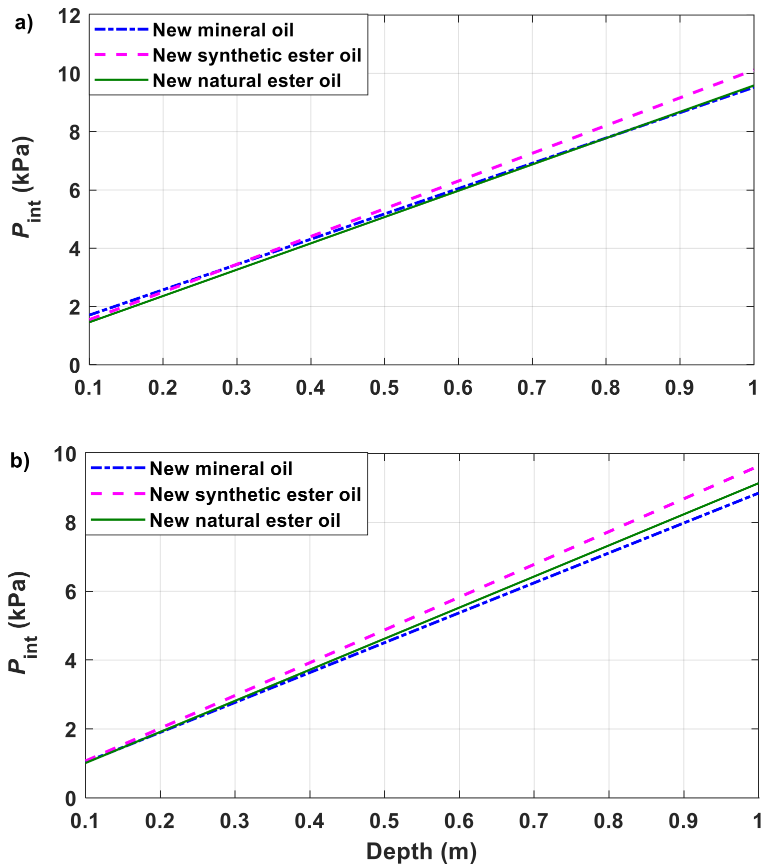

Figure 4-2: Internal pressure P_{int} inside a bubble; (a) $r = 0.1\ mm$, (b) $r = 0.5\ mm$.

Figure 4-3. The vessel is filled with 4.8 L of new Midel 7131 biodegradable synthetic oil and is not sealed. Two types of paper insulations including new Kraft paper and new TUP are used in the experiments. Dimensions of the Kraft paper and TUP strip samples are $242\ mm \times 48\ mm \times 0.2\ mm$ and $317\ mm \times 18\ mm \times 0.1\ mm$, respectively. The paper

Table 4-2: Properties of Midel 7131 [94] oil compared with requirements in IEC 61099 [96].

property	Requirements for property values based on IEC 61099	Midel 7131 property values
Density at 20˚C (kg/dm^3)	Max. 1	0.97
Kinematic viscosity (mm2/sec) at 40˚C	Max. 35	29
Kinematic viscosity (mm2/sec) at -20˚C	Max. 3000	1440
Flash point (˚C)	Min. 250	260
Fire point (˚C)	Min. 300	316
Pour point (˚C)	Max. -45	-56
Crystallization	No crystals	No crystals
Appearance	Clear, free from water and suspended matter and sediment	Clear, free from water and suspended matter and sediment
Dielectric breakdown (kV)	Min. 45	>75
Power factor at 90 ˚C	Max. 0.03	<0.008
DC resistivity at 90°C (GΩ.m)	Min. 2	>20
Water content (mg/kg)	Max. 200	50
Acidity (mg KOH/g)	Max. 0.03	<0.03
Total sludge (% mass)	Max. 0.01	<0.01

samples are wound around the cartridge heater in a single layer without overlapping. Figure 4-4 shows the sample and test papers that are wrapped around the cartridge heater.

Four thermocouples measure the temperature on the surface of the heater beneath the paper samples. The glass vessel with the heating cartridge immersed in the oil insulation is shown in Figure 4-5.The two thermometers in this figure each have two channels. Three channels are used to monitor the temperature on the heater's surface at three locations, and the fourth channel is for reading the bulk oil temperature. It is worth mentioning that a fifth thermocouple measures the temperature on the heater surface that is connected to the controller unit to limit the TRR.

A schematic of the test setup is shown in Figure 4-6. Rate of temperature rise on the heating cartridge's surface is kept at the desired level by a Jumo Itron-16 controller. The controller is installed inside a box that is powered by a three phase 381 V connection from

Figure 4-3: Cartridge heater.

the power grid. A picture of the controller unit on the box is shown in Figure 4-7. The temperature rise rate is required to be maintained over a wide range starting at the ambient temperature up to 200 ºC. A variable resistor is installed in series with the heating cartridge to limit its output power and damp the overshoots in low temperatures. In other words, the variable resistor introduces a variable gain to the controller unit. The initial resistance is set to 300 Ω and decreased in two discrete steps thereafter.

4.3.1 Moisture in Paper Insulations

The moisture content of the paper insulation can be measured directly via Karl Fischer titration. Indirect methods cannot accurately estimate the moisture content for this type of test where temperature increases constantly. To cite an instance, the moisture content of the paper insulation can be correlated to that of oil insulation via empirically obtained

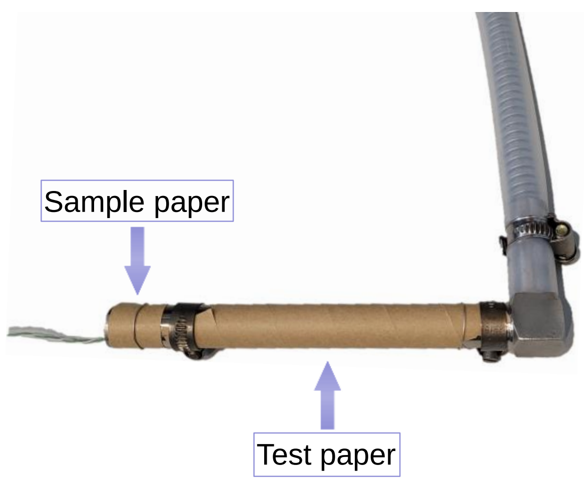

Figure 4-4: Cartridge heater with test and sample papers.

Figure 4-5: Glass vessel with the cartridge heater immersed in the oil.

curves as in [98]. The correlation is valid only if oil and paper insulations reach equilibrium, which takes a long time at low temperatures. Another study in [83] showed that applying

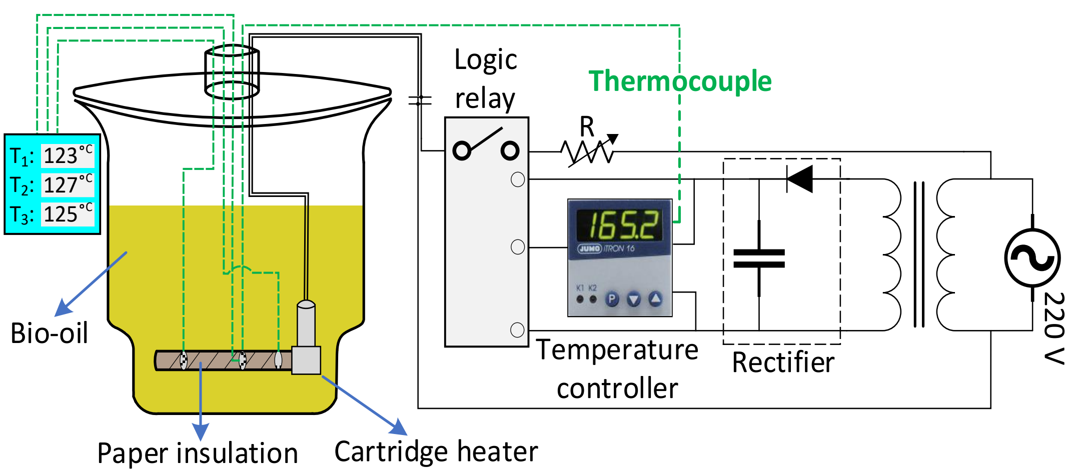

Figure 4-6: Schematic of the test setup.

an in-oil moisture sensor provides results that deviate about 1 % on average compared with the values obtained from Karl Fischer titration.

Another approach is taken in this research to measure the moisture content of the paper insulation. This approach is based on weighing the paper samples using a Kern weight with a 0.1 mg resolution. A paper sample on the scale is shown in Figure 4-8. A strip of paper insulation is wound around the cartridge heater that is in contact with the ambient air. The heater's temperature is set to 135 ºC and remains constant for 15 min. The moisture content is then derived from the difference in the weight of the paper before and immediately after drying. The amount of moisture absorbed by the paper sample is monitored by subsequent weight measurements on several occasions. The increase in moisture content of Kraft paper and TUP is plotted in Figure 4-9. It is worthwhile to mention that the initial moisture contents of the Kraft paper and TUP are 7.1 % and 6.1 %, respectively. The drying process and moisture absorption monitoring are repeated twice

Figure 4-7: Control unit box.

for each type of paper, and a curve is fitted to each dataset. The moisture content at a given time after drying the paper is calculated by averaging the corresponding data points on the fitted curves.

Five long and five short strips of kraft paper and TUP are dried on the cartridge heater and left in contact with the ambient air afterward. The samples remain in contact with the air for five different periods to absorb moisture at various levels. Once the predetermined elapsed time is reached, the short paper strip is removed from the heater and stored in a sealed glass container to verify the moisture content of the paper insulation. Subsequently, the heater with the long paper strip wound around it is immediately inserted into the oil vessel to begin the experiment. Moisture content for the five Kraft paper and five TUP samples are reported in Table 4-3.

The experiment is initiated by increasing the temperature of the cartridge heater at a

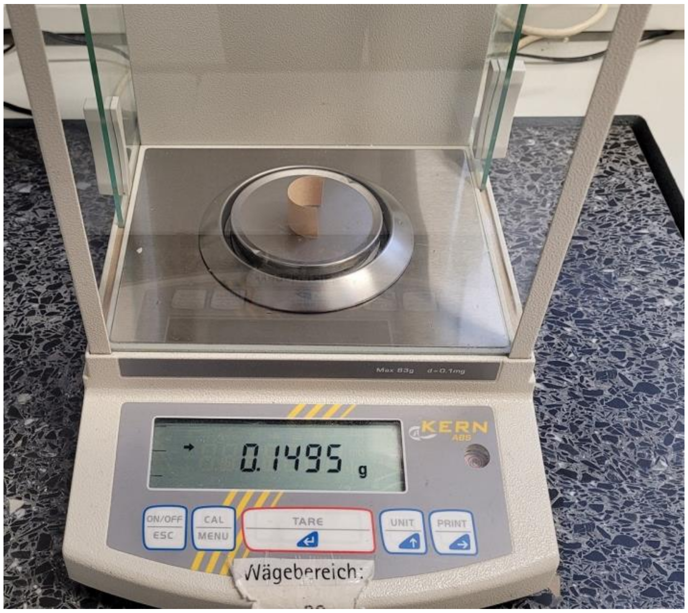

Figure 4-8: A paper sample on the scale.

3 ºC/min rate. A digital camera is set up in front of the oil glass vessel to record the experiment and readings of the thermocouples. The results of the experiments are reported in the following section.

4.4 Results and Observations

Video recordings of the experiments are reviewed to detect the first bubble, and the corresponding temperature is considered as BIT. The BITs for Kraft and TUP papers are reported and discussed in the following subsections. The results are compared with those reported in the literature as well.

4.4.1 BIT in Kraft Paper

BITs at different moisture levels in Kraft paper are plotted in Figure 4-10 along with those

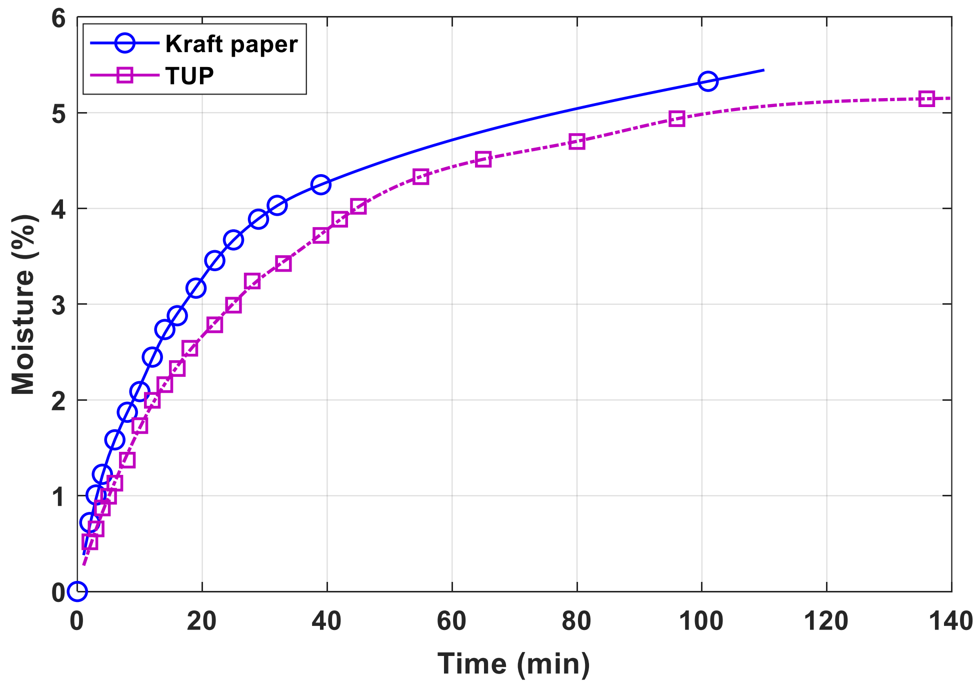

Figure 4-9: Increase in the moisture content of the paper insulations.

reported in [27, 28, 82-84]. A substantial discrepancy among the results is noticeable, especially in moisture contents in excess of 2 %. The causes of the discrepancies are outlined as follows. First and foremost, the BIT test procedures do not comply with a standard. The thermal energy is generated by a heater in this research and in [27, 82, 84], whereas step loads are applied to sectional windings in [27, 28, 82, 83]. Controlling temperature level and its rise rate is more challenging in the case of an actual winding, where high currents in the range of hundreds of amperes are required to achieve the BITs. To cite an instance, the temperature of the winding is increased by a three-step load profile in [83].

Second, the Kraft paper and oil insulation types used in the BIT experiments are distinct. The paper insulation is immersed in synthetic ester oil in this research, whereas mineral and natural ester oils are used in experiments in [27, 28, 82-84]. IFT and density

Table 4-3: Moisture absorption by Kraft paper and TUP from air.

Type of paper insulation	Post-drying resting time (min)	Moisture content (%)
Kraft	3	1.1
Kraft	6	1.6
Kraft	10	2.2
Kraft	20	3.3
Kraft	30	4.0
TUP	3	0.7
TUP	6	1.1
TUP	10	1.7
TUP	20	2.7
TUP	30	3.3

of oil insulation affect bubble growth according to (1). Third, findings in [28] demonstrated that a low gas content system has higher BIT than a nitrogen-statured system at moisture levels of approximately more than 2 %. Ultimately, visual detection of bubbles and errors in moisture measurement of the paper insulation, considering how fast they absorb moisture when in contact with ambient air, according to Figure 4-9, can be accounted for discrepancies among the BITs.

4.4.2 BIT in Upgraded Papers

Alternative paper insulations are seldom used in BIT tests. BITs for mineral oil-TUP and mineral oil-aramid paper insulation systems are evaluated in [27] and [85], respectively.

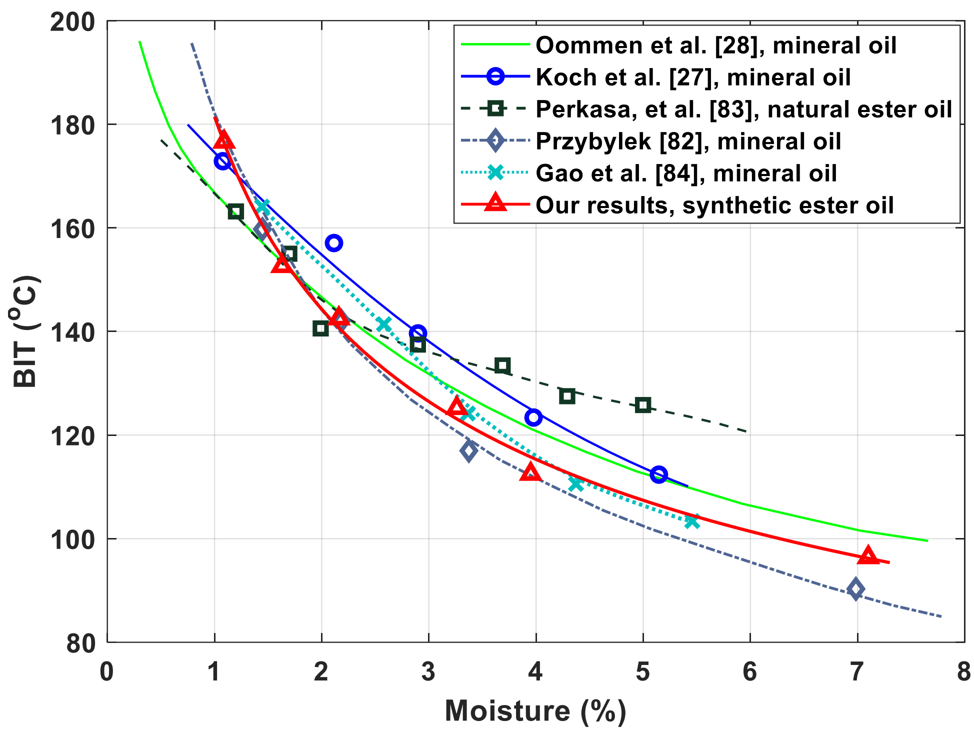

Figure 4-10: BITs for Kraft paper.

The BITs from [27] and [85] are compared in Figure 4-11 with those obtained in this research in a synthetic ester oil-TUP insulation system. Furthermore, results from another study in [28] are shown in Figure 4-11, which pertain to a nitrogen-saturated insulation system comprised of mineral oil and Kraft paper. Although Kraft paper is used in the experiments in [28], the nitrogen content can be related to TUP to provide insight into the difference in BITs between Kraft paper and TUP.

As shown in Figure 4-11, the TUP used in this research releases bubbles at significantly lower temperatures than the TUP used in [27]. Note that experiments in [27] yielded higher BITs for TUP than for Kraft paper, in contrast to this research's experimental results. A progressive divergence in the BITs of this research is noticeable compared to the results for aramid paper in [85] at moisture contents beyond 1 %. The

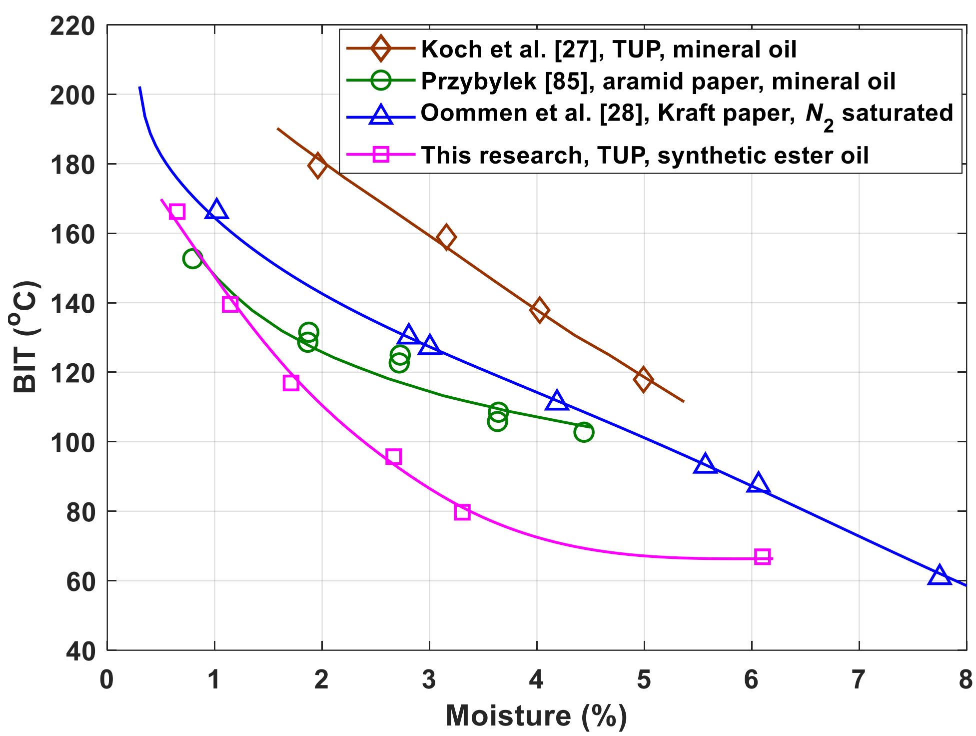

Figure 4-11: BIT for TUP, aramid paper, and Kraft paper (N_2 saturated).

TUP used in this research can be seen in Figure 4-11 to have lower BITs than Kraft paper in the nitrogen-saturated system. It is worth mentioning that the addition of nitrogen to the insulation system is shown to cause a reduction in BITs, according to the achievements in [28]. The experimental results are elaborated on in the next section, followed by discussing the reasons for significant differences in some BITs.

4.5 Discussion

Bubble formation in Kraft paper is investigated by several researchers, and the experimental results are reflected in BIT versus moisture plots. Nevertheless, a few BIT curves deviate significantly from the other data sets. The discrepancy among BITs is more noticed for alternative paper insulations and is more challenging to interpret due to fewer experimental results than for Kraft paper. This section addresses the causes of differences among the BITs reported in this research and the literature.

4.5.1 Kraft Paper

A closer look into Figure 4-10 reveals that experiments in [27, 83] resulted in noticeably higher BITs, particularly at high moisture contents. The heater in [27] and winding model in [83] are wrapped by two and four layers of Kraft paper, respectively. The innermost layer of the paper is subjected to the highest temperature. Therefore, the first bubbles are expected to emerge from beneath or on the surface of the innermost layer.

Reviewing video recordings of the experiments revealed that the first few bubbles emerge from junction areas of the paper insulation, as shown in Figure 4-12. A similar observation is reported in the experimental findings in [84]. Bubbles are small enough to be trapped in the junction of turns of paper insulation or in the overlay gaps. Hence, the bubbles can be overlooked by visual inspection of the multiple-layer insulation structure in [27, 83], which in turn resulted in higher BITs. A noticeable bubble accumulation is shown in Figure 4-13 where bubbles are attached to the paper insulation over a wide surface area. This figure is pertained to the Kraft paper with 4 % moisture content at a temperature of 198.9 ºC.

Less difference among the BITs at low moisture contents is noticeable in Figure 4-10. It can be justified considering that vapor pressure inside a bubble is directly related to the temperature. In this regard, the high kinetic energy of the bubble due to high temperature drives it to the insulation structure's surface and releases it into the oil. Consequently, there is less probability of overlooking the trapped bubbles at high temperatures. On the other hand, the aging of the paper insulation occurs first in amorphous regions at low temperatures and is expedited in crystal regions at elevated temperatures [99]. Since a less probabilistic behavior is expected in the crystal regions, fewer discrepancies among BITs at high temperatures are noticeable in Figure 4-10.

Since the experimental test setup in [27, 83] consists of multiple layers of paper insulation and a three-step load is applied in [83] as discussed in Section 4.4, their results are excluded from Figure 4-10. A curve is fitted to the average of the remaining data sets

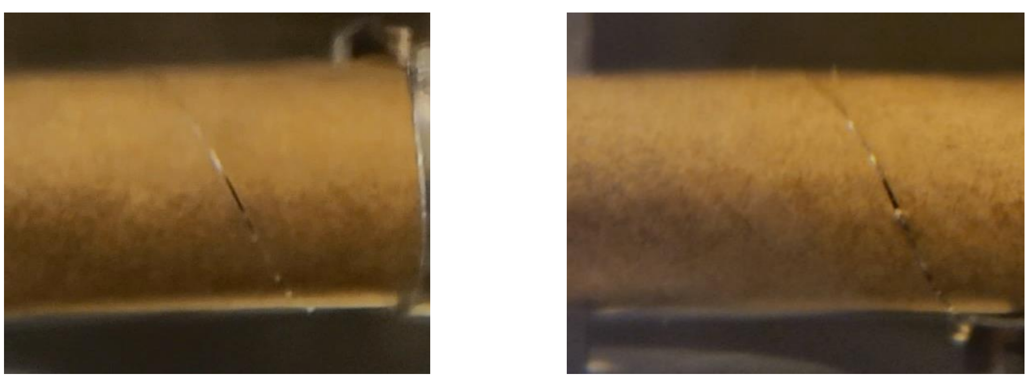

Figure 4-12: Bubbles in junction areas of Kraft paper insulation.

from this research and from [28, 82, 84] to obtain BIT from an exponential function as follows:

$$\mathrm{BIT}(m) = 94.68\, e^{-0.5733m} + 128.1\, e^{-0.04594m} \tag{4.2}$$

where m is moisture content of Kraft paper in percent. This function is only valid for values of m ranging from 1 to 7.1 %.

4.5.2 Upgraded Papers

Unlike the experimental results for Kraft paper, BITs for alternative paper insulations differ significantly, as can be seen in Figure 4-11. The differences stem from the methods and additives used to upgrade the insulation papers. Upgrading Kraft paper is typically achieved by two methods, either by modifying structure of chains in cellulose molecules or adding nitrous chemical compounds [100]. The latter is preferred from the

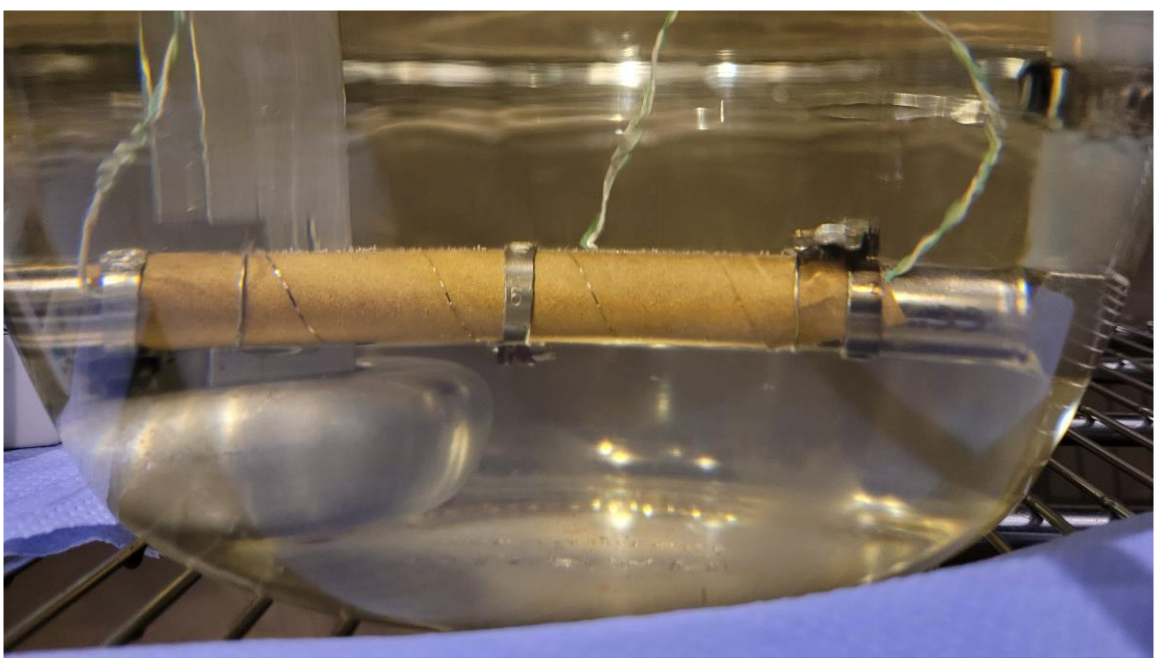

Figure 4-13: Bubble accumulation on Kraft paper.

manufacturers' perspective due to the simplicity of adding the chemical compounds compared to the alteration of OH groups in the cellulose chains [100]. However, the paper treatment is not standardized, and the nitrogen content can typically vary between 0.5 and 4 % [80]. The difference in the possible concentration of the nitrogen content, as well as manufacturing procedures, can justify the huge differences among BITs reported in this research and in [27]. Note that the paper insulation used in [27] is referred to as TUP, and no further details are provided.

BITs are evaluated in low gas content, and nitrogen saturated insulation systems in [28]. The reader may find the BIT curves obtained in [28] in Figure 4-10 and Figure 4-11, respectively. Although the same Kraft paper is used, lower BITs in the nitrogen saturated system are noticeable at moisture contents beyond 1 %. This implies the contribution of the nitrogen content in the bubble formation. These findings in [28] correspond to the reduced BITs observed in this research for TUP. The observations in [85] revealed lower BITs for aramid paper than for Kraft paper as well.

Nevertheless, experimental results from this research are in contrast to the results from [27], where elevated BITs are reported for TUP. The primary cause of significant differences in the BITs is related to the manufacturing process of producing TUPs. This implies the need for further experiments on TUPs from various manufacturers.

Bubble generation in the oil-paper insulations is only evaluated by the BIT criterion in the literature. The observations during the experiments of this research demonstrated a different rate for bubble formation in Kraft paper and TUP. In the case of a Kraft paper, a progressive bubble formation is observed by an increase in the temperature beyond the BIT. When the first bubble emerges, the rate of bubble generation increases by a rise in temperature until a continuous stream of bubbles is seen. However, TUP has a transient state between the BIT and the temperature beyond which bubbles are generated continuously. The temperature range of the transient region varies depending on the moisture content of the TUP. A criterion is defined to map the continuous bubbling generation temperature (CBGT) in TUP on BIT in Kraft paper. CBGT is reached if at least one bubble is seen each minute, considering the 3 ºC/min temperature rise rate. CBGT of TUP is compared to the BIT of kraft paper and TUP in Figure 4-14.

Comparing bubble formation in Kraft paper and TUP solely based on BIT at corresponding moisture levels cannot yield an accurate and comprehensive assessment. Single bubbles that occasionally emerge on the surface of TUP are less likely to threaten the insulation system's integrity compared to the stream of bubbles. BITs for Kraft paper are similar to CBGT levels for TUP if the intensity of bubble generation is taken into account. Although lower BITs are detected for the tested TUP than the Kraft paper, bubbles are generated at a lower rate in the TUP. On the other hand, Kraft paper ages at a higher rate than TUP. Water, as a byproduct of paper insulation aging, is less generated in TUP due to the added neutralizing or stabilizing agents [80]. In this regard, it is necessary to consider aging in terms of elapsed time instead of increased moisture content when comparing bubble generation in transformers with TUP and Kraft paper.

4.6 Bubble Generation at High Temperate Rise Rates

In the previous sections, BIT in both Kraft paper and TUP are investigated at a 3 ºC/min temperature rise rate (TRR). This rate is reported in the literature to represent the overload conditions for power transformers. However, GICs cause the HST of the transformers to increase at a considerably higher rate. According to a study in [32], the TRR can reach up to 20 ºC/min during peak of a GMD event. BITs are reported in [27] to be affected by the TRR. In this regard, two BIT detection experiments are conducted at a 20 ºC/min TRR to investigate GIC effects on bubble formation in power transformers. The BIT tests are performed on pairs of Kraft paper-synthetic ester oil and TUP-synthetic ester oil insulations.

The differences between bubbling in Kraft paper and TUP at 20 ºC/min TRR are outlined in Table 4-4. First bubble emergence temperatures in this table represent the initial temperature of the oil-paper insulation system. Bubbles are seen once the cartridge heater is connected to the power source. In other words, actual BIT could be lower than the levels mentioned in Table 4-4. Therefore, first bubble emergence temperatures

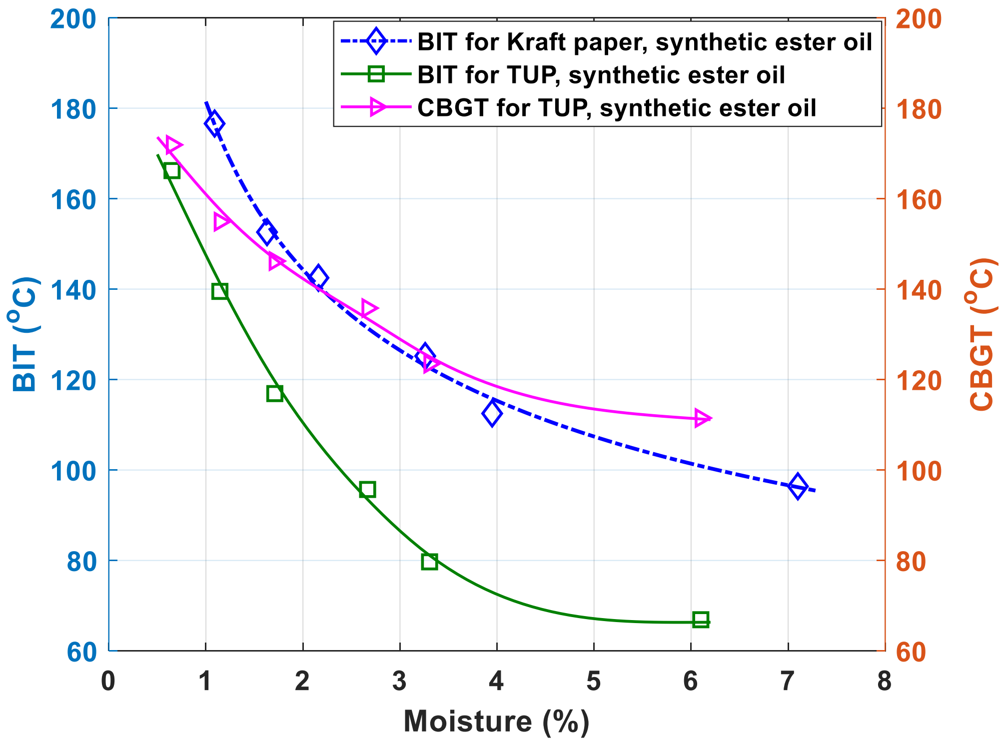

Figure 4-14: Comparing CBGT for TUP with BIT for Kraft paper and TUP; the data pertain to the experimental results from this research.

cannot be referred to as BITs.

A comparison between bubbling in Kraft paper and TUP reveals that even though TUP has less moisture content than Kraft paper, the rate of bubble release is higher in Kraft paper. As discussed earlier, first few bubbles emerge from under the paper, where it has a higher temperature due to direct contact with the heater's surface.

The temperature at which bubbles emerge from surface of the paper insulations is reported in Table 4-4. The higher surface bubble release temperature for Kraft paper can be correlated to its higher thickness. It is worth mentioning Kraft paper and TUP samples have a thickness of $0.2\,mm$ and $0.1\,mm$, respectively. A higher thickness imposes a higher resistance to thermal conductivity and therefore, causes a more significant temperature difference between upper and lower surfaces of the paper insulation.

The differences between bubbling at 3 ºC/min and 20 ºC/min TRRs are not limited to

Table 4-4: Comparing bubbling in Kraft paper and TUP at a 20 ºC/min TRR.

property	Type of paper	
	Kraft paper	TUP
Moisture content	3.3 %	2.7 %
First bubble emergence Temperature	31.7 ˚C	24.8 ˚C
Degree of bubbling	Stream of large bubbles	Few small bubbles
Bubble release temperature at paper's surface	65.9 ˚C	24.8 ˚C
Comparing bubbling with 3 ºC/min	Significantly more bubbles compared with 3 ˚C/min TRR	Only few more bubbles generated compared with 3 ˚C/min TRR

only BITs. The rate of bubble generation and bubble accumulation on paper insulation's surface are of significant importance to evaluate the dangers of bubbles to the integrity of the insulation system. As it is reported in Table 4-4, Kraft paper releases considerably more bubbles at 20 ºC/min than 3 ºC/min TRR. Nevertheless, rate of bubble generation in TUP is observed to be slightly affected by an increase in the TRR. Although TUP releases surface bubbles at lower temperatures than Kraft paper, rate of bubble generation and bubble concentration is less than that of in Kraft paper. Bubble accumulation is compared between Kraft paper and TUP at two different temperatures in Figure 4-15. The initial moisture content for Kraft paper and TUP at the beginning of the experiments are 3.3 % and 2.7 %, respectively. Accumulation of bubbles on the surface of Kraft paper is evident especially at high temperatures in Figure 4-15.

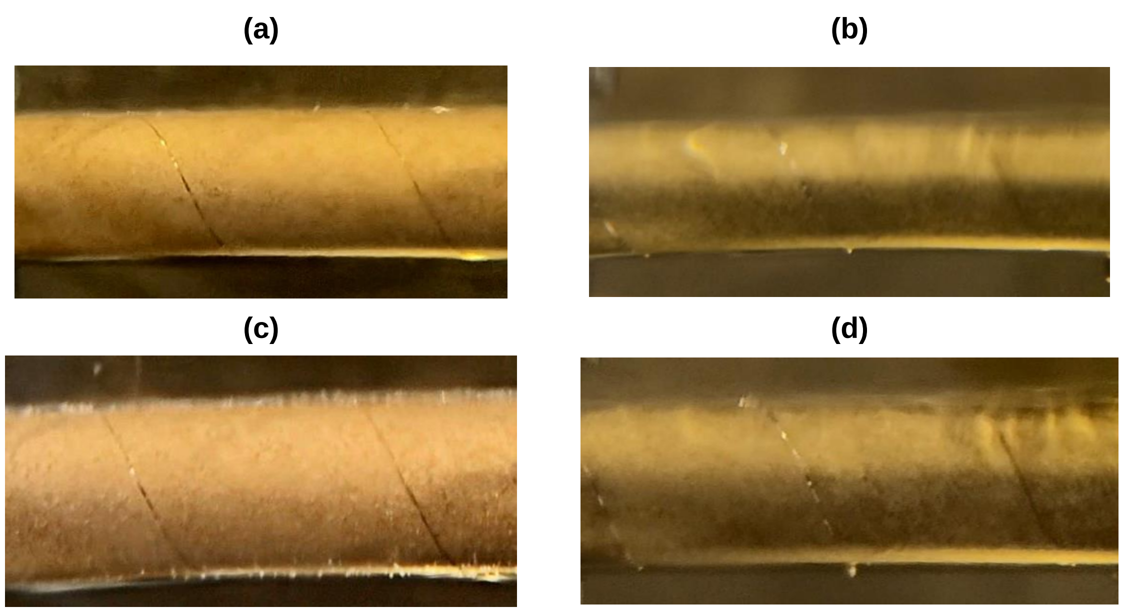

Figure 4-15: Bubble generation in Kraft paper and TUP at 20 ºC/min; (a) Kraft paper at 133 ºC, (b) TUP at 133 ºC, (c) kraft paper at 177 ºC, (d) TUP at 177 ºC.

4.7 Conclusion

The experiments aimed to detect BIT in oil-paper insulation systems are not standardized. The number of layers of paper insulation wrapped around the winding, depth of the winding in oil or oil pressure, and temperature rise rate are among the essential parameters required to be incorporated into a standard procedure for BIT detection experiments. The availability of various experimental results for BIT in the Kraft paper allows a comprehensive comparison among the results obtained by different test setups. Although synthetic ester oil is used in the experiments of this research, BITs in the single-layer Kraft paper insulation system are similar to BITs detected in other experiments with mineral oil.

However, only a few data sets are available for BIT in alternative paper insulations, and the data differ significantly from each other. Bubbling in TUP has a different behavior than in Kraft paper. Therefore, the difference in the bubble formation in these two types of paper insulations is not reflected only in the BITs. This implies the need for conducting more experiments on TUP, considering different procedures are adopted for manufacturing TUPs.

A high temperature rise rate is demonstrated to lower BIT significantly. In this regard, GICs during peak of a severe GMD event could cause a catastrophic failure in the power transformer's insulation system. BIT needs to be accompanied by further information regarding bubble release rate and bubble accumulation to provide a comprehensive assessment of the oil-paper insulation system in presence of the gaseous bubbles.

Chapter 5

Summary and Future Directions

5.1 Summary

In Chapter 2, an offline geomagnetic field monitoring system is established. Advantages of increasing signal quality outweigh processing time in the offline system. Several mathematical tools based on wavelet transforms are applied to extract most noise components from the magnetic field signals. In the first step, high frequency noises are detected and removed by decomposing the magnetic field signals down to four levels using sym4 wavelet. In the second step, spikes in the signals are detected by a stationary wavelet transform and replaced by a weighted average of nearby samples. These two steps ensure minimum noise amplification in taking time-derivative of the magnetic field signals. The best method to extract frequency ridges in the magnetic field signals is introduced and verified in this chapter. An approach based on continuous wavelet transform is introduced as to further damp noises in the derivative signal. Implementing the proposed signal processing methods is verified to significantly increase accuracy of the induced electric field and GIC calculations.

In Chapter 3, the offline geomagnetic field monitoring system that is developed in

Chapter 2 is shifted to an online platform basis. In this regard, computational burden and processing times become of significant importance. The other challenge is to overcome lack of successive data points at each time, since the magnetic field signal samples can only be compared to the previously recoded data points. The online processing of the magnetic field signals requires a sliding window. It is discovered that the optimum window width equals 128 as to reduce noises to an acceptable level without a considerable increase in the processing time. Although the offline monitoring system outperforms the online system, the difference in SNR of the denoised signals by these two systems is shown to be negligible in most cases.

Chapter 4 includes the empirical results of this research. In this chapter, effects of an elevated HST of power transformers due to GIC are evaluated. A test setup is developed to analyze bubble formation and detect BIT in oil-paper insulations. Two pairs of insulations including synthetic ester oil-Kraft paper and synthetic ester oil-TUP are used in the experiments. BITs are detected at two rates, 3 ºC/min and 20 ºC/min. Results of the experiments revealed that bubble formation and accumulation cannot be compared between Kraft paper and TUP only based on BITs. Rates of bubble generation and bubble accumulation are required to be taken into account as well.

5.2 Future Directions

Given the established geomagnetic field monitoring systems in this research, GIC flows can be estimated for severe historical GMD events on each bus of an actual or benchmark power systems. The road map for future works is discussed as follows.

Correlating GIC to power transformer HST: The loading guides for power transformers such as IEEE Standard C57.91 [70] and IEC 60076-7 [79] do not account for semi-dc GIC flows or half-cycle saturation in their HST calculation models. Although a method is presented in [32] to incorporate GIC in the HST calculations, thermal response of the transformer is required to determine HST. A generalized method for the HST calculation based on measured transformer parameters such as those in the above-mentioned standards is needed to be developed. This modified model could be applied to correlate GIC levels to HST of transformers that are currently operating in the power system.

Evaluating effects of GIC on lifetime reduction of power transformers: Bubble formation is one of the potential consequences of a temperature rise inside a transformer tank. Lifetime of transformers depends on the condition of their insulation system and paper insulation in particular. Degree of polymerization (DP) is a measure of evaluating remnant life of the paper insulations [101-103]. Temperature is among parameters that negatively affect DP values [88, 104, 105]. In this regard, lowest DP values are expected in the vicinity of HST, where the paper insulation ages at the highest temperature of transformer winding [80, 106].

GICs typically do not last for long periods. Nevertheless, they could significantly rise the HST. It is demonstrated in [89, 107] that a rise in HST causes an exponential decay in the DP. High amplitude GICs may not last for long, but the resultant reduction in the DP and remnant life of the paper insulation is substantial nonetheless. A DP analysis based on GIC flows in windings of a transformer provides valuable information on detrimental effects of the GIC on the insulation system.

References

[1] "Special reliability assessment interim report: Effects of geomagnetic disturbances on the bulk power system," North American Electric Reliability Corporation (NERC), Feb. 2012.

[2] G. S. Lakhina, S. Alex, B. T. Tsurutani, and W. D. Gonzalez, "Research on Historical Records of Geomagnetic Storms," *Proceedings of the International Astronomical Union,* vol. 2004, pp. 3-15, 2004.

[3] R. Acharya, B. Roy, M. R. Sivaraman, and A. Dasgupta, "An empirical relation of daytime equatorial total electron content with equatorial electrojet in the Indian zone," *Journal of Atmospheric and Solar-Terrestrial Physics,* vol. 72, pp. 774–780, 2010.

[4] R. J. Pirjola, "Modelling the electric and magnetic fields at the Earth's surface due to an auroral electrojet," *Journal of Atmospheric and Solar-Terrestrial Physics,* vol. 60, pp. 1139-1148, 1998.

[5] M. V. Klimenko, V. V. Klimenko, I. V. Despirak, I. E. Zakharenkova, B. V. Kozelov, S. M. Cherniakov*, et al.*, "Disturbances of the thermosphere-ionosphere-plasmasphere system and auroral electrojet at 30°E longitude during the St. Patrick's Day geomagnetic storm on 17–23 March 2015," *Journal of Atmospheric and Solar-Terrestrial Physics,* vol. 180, pp. 78–92, 2018.

[6] Y. I. Feldstein, L. I. Gromova, A. Grafe, C.-I. Meng, V. V. Kalegaev, I. I. Alexeev*, et al.*, "Dynamics of the auroral electrojets and their mapping to the magnetosphere," *Radiation Measurements,* vol. 30, pp. 579–587, 1999.

[7] Z. Zheng, H. Wang, L. Yu, Y. He, and K. Li, "Temporal and spatial variations of the equatorial electrojet during storm times from CHAMP observations," *Journal of Atmospheric and Solar-Terrestrial Physics,* vol. 179, pp. 307–315, 2018.

[8] P. Alken and S. Maus, "Relationship between the ionospheric eastward electric field and the equatorial electrojet," *Geophysical Research Letters,* vol. 37, 2010.

[9] J. Bulusu, A. R. K., K. Arora, N. P. Chandrasekhar, and N. Nagarajan, "Effect of Disturbance Electric Fields on Equatorial Electrojet Over Indian Longitudes," *Journal of Geophysical Research: Space Physics,* vol. 123, pp. 5894–5916, 2018.

[10] C.-M. Huang, "Theoretical effects of geomagnetic activity on low-latitude ionospheric electric fields," *Journal of Geophysical Research,* vol. 110, 2005.

[11] J. K. Sandhu, I. J. Rae, and M. T. Walach, "Challenging the Use of Ring Current Indices During Geomagnetic Storms," *Journal of Geophysical Research: Space Physics,* vol. 126, 2021.

[12] K. Zhang, H. Wang, Y. Yamazaki, and C. Xiong, "Effects of Subauroral Polarization Streams on the Equatorial Electrojet During the Geomagnetic Storm on June 1, 2013," *Journal of Geophysical Research: Space Physics,* vol. 126, 2021.

[13] J. G. Kappernman and v. d. Albertson, "Bracing for the geomagnetic storms," *IEEE Spectrum,* vol. 27, pp. 27–33, 1990.

[14] "Geo-Magnetic Disturbances (GMD): Monitoring, Mitigation, and Next Steps: A Literature Review and Summary of the April 2011 NERC GMD Workshop," North American Electric Reliability Corporation (NERC), , Atlanta, 2011.

[15] D. Chakrabarty, M. S. Bagiya, S. V. Thampi, B. M. Pathan, and R. Sekar, "Signatures of moderate (M-class) and low (C and B class) intensity solar flares on the equatorial electrojet current: Case studies," *Journal of Atmospheric and Solar-Terrestrial Physics,* vol. 105-106, pp. 170–180, 2013.

[16] *International Real-Time Magnetic Observatory Network*. Available: https://intermagnet.github.io/

[17] L. W. Pedersen and L. Merenyi, "The FGE Magnetometer and the Intermagnet 1 Second Standard," *J. Ind. Geophys. Union,* vol. 2, pp. 30-36, 2016.

[18] A. Rezaei-Zare, "Behavior of Single-Phase Transformers Under Geomagnetically Induced Current Conditions," *IEEE Trans. Power Del.,* vol. 29, pp. 916-925, 2014.

[19] P. R. Price, "Geomagnetically induced current effects on transformers," *IEEE Trans. Power Del.,* vol. 17, pp. 1002-1008, 2002.

[20] A. Rezaei-Zare and A. H. Etemadi, "Optimal Placement of GIC Blocking Devices Considering Equipment Thermal Limits and Power System Operation Constraints," *IEEE Trans. Power Del.,* vol. 33, pp. 200-208, 2018.

[21] D. H. Boteler and E. Bradley, "On the Interaction of Power Transformers and Geomagnetically Induced Currents," *IEEE Trans. Power Del.,* vol. 31, pp. 2188-2195, 2016.

[22] A. Rezaei-Zare, "Reactive Power Loss Versus GIC Characteristic of Single-Phase Transformers," *IEEE Trans. Power Del.,* vol. 30, pp. 1639-1640, 2015.

[23] "Geomagnetic Disturbance Monitoring Approach and Implementation Strategies," U.S. Department of Energy, Washington, D.C.2019.

[24] L. Marti, A. Rezaei-Zare, and D. Boteler, "Calculation of Induced Electric Field During a Geomagnetic Storm Using Recursive Convolution," *IEEE Trans. Power Del.,* vol. 29, pp. 802-807, 2014.

[25] R. Pirjola, "Review on the calculation of Surface Electric and Magnetic Fields and of Geomagnetically Induced Currents in Ground-Based Technological Systems," *Surveys in Geophysics,* vol. 23, pp. 71-90, 2002.

[26] A. Haddadi, A. Rezaei-Zare, L. Gerin-Lajoie, R. Hassani, and J. Mahseredjian, "A Modified IEEE 118-Bus Test Case for Geomagnetic Disturbance Studies–Part I: Model Data," *IEEE Transactions on Electromagnetic Compatibility,* pp. 1-11, 2019.

[27] M. Koch and S. Tenbohlen, "Evolution of bubbles in oil–paper insulation influenced by material quality and ageing," *IET Electric Power Applications,* vol. 5, pp. 168-174(6), 2011.

[28] T. V. Oommen and S. R. Lindgren, "Bubble evolution from transformer overload," in *2001 IEEEPES Transmission and Distribution Conference and Exposition*, ed Piscataway NJ: IEEE, 2001, pp. 137–142.

[29] N. Chao, T. Zhao, M. Fan, and Y. Liu, "Study on Bubble Formation of Different Moisture Content Oil-immersed Cardboards in Natural Ester Oil," in *2019 IEEE 20th International Conference on Dielectric Liquids (ICDL)*, ed [Piscataway, NJ]: IEEE, 2019, pp. 1–4.

[30] C. Qin, Y. He, B. Shi, T. Zhao, F. Lv, and X. Cheng, "Experimental Study on Breakdown Characteristics of Transformer Oil Influenced by Bubbles," *Energies,* vol. 11, p. 634, 2018.

[31] A. Pulkkinen, E. Bernabeu, A. Thomson, A. Viljanen, R. Pirjola, D. Boteler*, et al.*, "Geomagnetically induced currents: Science, engineering, and applications readiness," *Space Weather,* vol. 15, pp. 828-856, 2017.

[32] L. Marti, A. Rezaei-Zare, and A. Narang, "Simulation of Transformer Hotspot Heating due to Geomagnetically Induced Currents," *IEEE Trans. Power Del.,* vol. 28, pp. 320-327, 2013.

[33] R. Pirjola, "Geomagnetically induced currents during magnetic storms," *IEEE Transactions on Plasma Science,* vol. 28, pp. 1867-1873, 2000.

[34] C. Chen, J. Wang, and D. Ton, "Modernizing Distribution System Restoration to Achieve Grid Resiliency Against Extreme Weather Events: An Integrated Solution," *Proceedings of the IEEE,* vol. 105, pp. 1267-1288, 2017.

[35] L. Marti, C. Yiu, A. Rezaei-Zare, and D. Boteler, "Simulation of Geomagnetically Induced Currents With Piecewise Layered-Earth Models," *IEEE Trans. Power Del.,* vol. 29, pp. 1886-1893, 2014.

[36] H. Karami, K. Sheshyekani, A. Rezaei-Zare, and J. Mahseredjian, "Effect of Mixed Propagation Path on Electromagnetic Fields at Ground Surface Produced by Electrojet," *IEEE Transactions on Electromagnetic Compatibility,* vol. 60, pp. 2019-2024, 2018.

[37] R. Horton, D. Boteler, T. J. Overbye, R. Pirjola, and R. C. Dugan, "A Test Case for the Calculation of Geomagnetically Induced Currents," *IEEE Transactions on Power Delivery,* vol. 27, pp. 2368-2373, 2012.

[38] A. Haddadi, L. Gerin-Lajoie, A. Rezaei-Zare, R. Hassani, and J. Mahseredjian, "A Modified IEEE 118-Bus Test Case for Geomagnetic Disturbance Studies—Part II:

Simulation Results," *IEEE Transactions on Electromagnetic Compatibility,* pp. 1-10, 2019.

[39] D. Cilden-Guler, Z. Kaymaz, and C. Hajiyev, "Assessment of Magnetic Storm Effects under Various Magnetometer Noise Levels for Satellite Attitude Estimation," presented at the 2019 9th International Conference on Recent Advances in Space Technologies (RAST), [Piscataway, New Jersey], 2019.

[40] B. Dufay, E. Portalier, S. Saez, C. Dolabdjian, D. Seddaoui, A. Yelon*, et al.*, "Low Frequency Excess Noise Source Investigation of Off-Diagonal GMI-Based Magnetometers," *IEEE Transactions on Magnetics,* vol. 53, pp. 1-6, 2017.

[41] M. Janosek, M. Butta, M. Dressler, E. Saunderson, D. Novotny, and C. Fourie, "1-pT Noise Fluxgate Magnetometer for Geomagnetic Measurements and Unshielded Magnetocardiography," *IEEE Transactions on Instrumentation and Measurement,* vol. 69, pp. 2552-2560, 2020.

[42] M. Butta and I. Sasada, "Sources of Noise in a Magnetometer Based on Orthogonal Fluxgate Operated in Fundamental Mode," *IEEE Transactions on Magnetics,* vol. 48, pp. 1508-1511, 2012.

[43] J. Ma and T. Uchiyama, "High Performance Single Element MI Magnetometer With Peak-to-Peak Voltage Detector by Synchronized Switching," *IEEE Transactions on Magnetics,* vol. 53, pp. 1-4, 2017.

[44] A. Sheinker, A. Shkalim, N. Salomonski, B. Ginzburg, L. Frumkis, and B.-Z. Kaplan, "Processing of a scalar magnetometer signal contaminated by 1/fα noise," *Sensors and Actuators A: Physical,* vol. 138, pp. 105-111, 2007.

[45] T. Wang, C. Kang, and G. Chai, "Low-Frequency Noise Evaluation on a Commercial Magnetoimpedance Sensor at Submillihertz Frequencies for Space Magnetic Field Detection," *Sensors,* vol. 19, p. p. 4888, 2019.

[46] R. Chartrand, "Numerical differentiation of noisy, nonsmooth, multidimensional data," presented at the IEEE Global Conf. on Signal and Information Processing, Piscataway, NJ, 2017.

[47] M. Rezaei-Zare, M. Ariannik, and A. Rezaei-Zare, "Real-time detection of vulnerable power system areas to geomagnetic disturbance," *IET Generation, Transmission & Distribution,* vol. 14, pp. 3838-3845, 2020.

[48] W. K. Pratt, *Digital image processing*, 3. ed. New York: Wiley, 2001, pp. 271–276.

[49] R. Pirjola and A. Viljanen, "Complex image method for calculating electric and magnetic fields produced by an auroral electrojet of finite length," *Annales Geophysicae,* vol. 16, pp. 1434-1444, 1998.

[50] S. G. Mallat, *A wavelet tour of signal processing: The Sparse way*, Sparse ed. ed. Amsterdam; Boston: Elsevier /Academic Press, 2009, pp. 11–14, 17, 113, 208–210.

[51] A. Taebi and H. A. Mansy, "Time-Frequency Distribution of Seismocardiographic Signals: A Comparative Study," *Bioengineering (Basel, Switzerland),* vol. 4, 2017.

[52] F. Auger, P. Flandrin, Y.-T. Lin, S. McLaughlin, S. Meignen, T. Oberlin*, et al.*, "Time-Frequency Reassignment and Synchrosqueezing: An Overview," *IEEE Signal Processing Magazine,* vol. 30, pp. 32–41, 2013.

[53] I. Daubechies, J. Lu, and H.-T. Wu, "Synchrosqueezed wavelet transforms: An empirical mode decomposition-like tool," *Applied and Computational Harmonic Analysis,* vol. 30, pp. 243–261, 2011.

[54] R. Schafer, "What Is a Savitzky-Golay Filter? [Lecture Notes]," *IEEE Signal Processing Magazine,* vol. 28, pp. 111–117, 2011.

[55] M. A. Sharifi, M. R. Seif, and M. A. Hadi, "A Comparison Between Numerical Differentiation and Kalman Filtering for a Leo Satellite Velocity Determination," *Artificial Satellites,* vol. 48, pp. 103-110, 2013.

[56] N. Orani, A. Pisano, and E. Usai, "On a new sliding-mode differentiation scheme," presented at the IEEE Int. Conf. on Industrial Technology, [Piscataway, N.J.].

[57] A. Levant, "Robust exact differentiation via sliding mode technique," *Automatica,* vol. 34, pp. 379-384, 1998.

[58] D. H. Boteler and R. J. Pirjola, "The complex-image method for calculating the magnetic and electric fields produced at the surface of the Earth by the auroral electrojet," *Geophysical Journal International,* vol. 132, pp. 31-40, 1998.

[59] X. Shao and C. Ma, "A general approach to derivative calculation using wavelet transform," *Chemometrics and Intelligent Laboratory Systems,* vol. 69, pp. 157-165, 2003.

[60] R. Garcia-Bermudez, F. Rojas, G. Demera, C. Torres, D. Zambrano, G. Joya*, et al.*, "Evaluation of the Differentiation of Noisy Electrooculographic Records Using Continuous Wavelet Transform," presented at the Bioinformatics and Biomedical Engineering, Cham, 2017.

[61] Z. Wang, Y. Shen, X. Zhang, and Q. Wang, "Fault diagnosis based on numerical differentiation using wavelet transform," presented at the IEEE Int. Instrumentation and Measurement Technology Conf, Piscataway, NJ, 2012.

[62] S. G. Mallat, *A wavelet tour of signal processing*, Sparse ed. ed. Amsterdam; Boston: Elsevier /Academic Press, 2009.

[63] P. Werle, A. Akbari, H. Borsi, and E. Gockenbach, "Enhanced online PD evaluation on power transformers using wavelet techniques and frequency rejection filter for noise suppression," presented at the IEEE int. symposium on electrical insulation, 2002.

[64] M. Ariannik and A. Rezaei-Zare, "Online Monitoring of Magnetometer Signals for Estimating Induced Electric Fields in Power Systems," *IEEE Transactions on Power Delivery,* vol. 37, pp. 5454–5460, 2022.

[65] K. S. Shetye, R. R. Kumar, C. Klauber, Z. Mao, T. J. Overbye, J. Gannon*, et al.*, "Development and Electric Grid Applications of a Magnetometer Network," *IEEE Open Access Journal of Power and Energy,* vol. 8, pp. 77-84, 2021.

[66] E. Weiss, R. Alimi, A. Ivry, and E. Fisher, "Investigation and Modeling of Large Barkhausen Jumps Dynamics in Low-Power Fluxgate Magnetometers," *IEEE Sensors Journal,* vol. 19, pp. 2105-2112, 2019.

[67] E. Paperno, "Suppression of magnetic noise in the fundamental-mode orthogonal fluxgate," *Sensors and Actuators A: Physical,* vol. 116, pp. 405-409, 2004.

[68] M. Ariannik, A. Rezaei-Zare, and P. Werle, "Processing Magnetometer Signals for Accurate Wide-Area Geomagnetic Disturbance Monitoring and Resilience Analysis," *IEEE Trans. Power Del.,* vol. 36, pp. 2550-2558, 2020.

[69] S. Sagareli, M. Koenig, H. Camara, V. Panuccio, S. Sambasivan, A. O'Malley*, et al.*, "Geomagnetic Disturbances Monitoring, Modelling and Mitigation," *CIGRE,* vol. C2-202, pp. 1-9, 2016.

[70] "IEEE Guide for Loading Mineral-Oil-Immersed Transformers and Step-Voltage Regulators," *IEEE Std C57.91-2011 (Revision of IEEE Std C57.91-1995),* pp. 1-123, 2012.

[71] J. P. Hill, Z. Wang, Q. Liu, S. Matharage, A. Hilker, and D. Walker, "Improvements to the Construction of Bubble Inception Formulae for Use With Transformer Insulation," *IEEE Access,* vol. 7, pp. 171673-171683, 2019.

[72] A. Esper, B. Dufay, S. Saez, and C. Dolabdjian, "Theoretical and Experimental Investigation of Temperature-Compensated off-diagonal GMI Magnetometer and its long-term Stability," *IEEE Sensors Journal,* vol. 20, pp. 9046-9055, 2020.

[73] Y. Wu, D. Zou, P. Liu, and W. Yu, "Dynamic Magnetometer Calibration and Alignment to Inertial Sensors by Kalman Filtering," *IEEE Transactions on Control Systems Technology,* vol. 26, pp. 716-723, 2018.

[74] M. Misiti, *Wavelets and their applications*. London: ISTE, 2007.

[75] R. Pirjola and D. Boteler, "Calculation methods of the electric and magnetic fields at the Earth's surface produced by a line current," *Radio Science,* vol. 37, pp. pp. 1-9, 2002.

[76] A. Viljanen, A. Pulkkinen, O. Amm, R. Pirjola, T. Korja, and B. W. Group, "Fast computation of the geoelectric field using the method of elementary current systems and planar Earth models," *Annales Geophysicae,* vol. 22, pp. 101-113, 2004.

[77] G. W. Collins, *Fundamental Numerical Methods and Data Analysis*: NASA ADS, 2003.

[78] F. Han, S. Harada, and I. Sasada, "Fluxgate and Search Coil Hybrid: A Low-Noise Wide-Band Magnetometer," *IEEE Transactions on Magnetics,* vol. 48, pp. 3700-3703, 2012.

[79] "Power transformers - Part 7: Loading guide for mineral-oil-immersed power transformers," *IEC 60076-7 Standard,* 2018.

[80] D. A. L. E. Lundgaard, I. A. Höhlein, R. Clavreul, M. O. Dahlund, H. Gasser, R. Heywood, C. Krause, M. Lessard, T. K. Saha, V. Sokolov, A. Pablo, "Ageing of cellulose in mineral-oil insulated transformers," *CIGRE Technical Brochure,* vol. 323, pp. pp. 19-20, 2007.

[81] Y. Zhang, X. Tao, C. Pan, and J. Tang, "Role of air bubbles in the breakdown of flowing transformer oil," *IEEE Transactions on Dielectrics and Electrical Insulation,* vol. 27, pp. 1752–1760, 2020.

[82] P. Przybylek, "The influence of cellulose insulation aging degree on its water sorption properties and bubble evolution," *IEEE Transactions on Dielectrics and Electrical Insulation,* vol. 17, pp. 906–912, 2010.

[83] C. Y. Perkasa, N. Lelekakis, T. Czaszejko, J. Wijaya, and D. Martin, "A comparison of the formation of bubbles and water droplets in vegetable and mineral oil impregnated transformer paper," *IEEE Transactions on Dielectrics and Electrical Insulation,* vol. 21, pp. 2111–2118, 2014.

[84] M. Gao, Q. Zhang, Y. Ding, T. Wang, H. Ni, and W. Yuan, "Investigation on bubbling phenomenon in oil-paper insulation," *IEEE Transactions on Dielectrics and Electrical Insulation,* vol. 24, pp. 2362–2370, 2017.

[85] P. Przybylek, "A comparison of bubble evolution temperature in aramid and cellulose paper," in *2013 IEEE International Conference on Solid Dielectrics (ICSD)*, ed Piscataway, NJ: IEEE, 2013, pp. 983–986.

[86] J. Hill, Z. Wang, Q. Liu, C. Krause, and G. Wilson, "Analysing the power transformer temperature limitation for avoidance of bubble formation," *High Voltage,* vol. 4, pp. 210–216, 2019.

[87] L. E. Lundgaard, W. Hansen, D. Linhjell, and T. J. Painter, "Aging of Oil-Impregnated Paper in Power Transformers," *IEEE Transactions on Power Delivery,* vol. 19, pp. 230–239, 2004.

[88] N. Lelekakis, D. Martin, and J. Wijaya, "Ageing rate of paper insulation used in power transformers Part 1: Oil/paper system with low oxygen concentration," *IEEE Transactions on Dielectrics and Electrical Insulation,* vol. 19, pp. 1999–2008, 2012.

[89] M. Ariannik, A. A. Razi-Kazemi, and M. Lehtonen, "Effect of cumulative moisture content on degradation of transformer paper insulation," *IEEE Transactions on Dielectrics and Electrical Insulation,* vol. 24, pp. 611–618, 2017.

[90] T. V. Oommen and T. A. Prevost, "Cellulose insulation in oil-filled power transformers: part II maintaining insulation integrity and life," *IEEE Electrical Insulation Magazine,* vol. 22, pp. 5–14, 2006.

[91] C. E. Brennen, *Cavitation and bubble dynamics*, First published. ed. New York, NY: Oxford University Press, 1995.

[92] A. Zou, A. Chanana, A. Agrawal, P. C. Wayner, and S. C. Maroo, "Steady State Vapor Bubble in Pool Boiling," *Scientific reports,* vol. 6, p. 20240, 2016.

[93] "Shell Diala Transformer Oil Handbook," in *1st. ed, Shell*, ed.

[94] T. Koffi, K. S. Kassi, G. Kone, J. S. N'Cho, M. Edoé, J. Bosson*, et al.*, "Using structured laser illumination planar imaging (SLIPI) as a new technique to monitor the degradation of biodegradable oils in electrical power transformers," *IET Generation, Transmission & Distribution,* 2022.

[95] I. Fofana, A. Bouaicha, M. Farzaneh, and J. Sabau, "Ageing Behaviour of Mineral Oil and Ester Liquids: a Comparative Study," in *Electrical Insulation and Dielectric*

Phenomena, 2008. CEIDP 2008. Annual Report Conference on, ed Los Alamitos: IEEE Computer Society, 2008, pp. 87–90.

[96] "MIDEL 7131 Synthetic Ester Transformer Fluid Fire safe and Biodegradable," Product Brochure, Jun. 2019.

[97] "Insulating liquids - Specifications for unused synthetic organic esters for electrical purposes," *IEC 61099 Standard,* 2010.

[98] M. Koch, S. Tenbohlen, and T. Stirl, "Diagnostic Application of Moisture Equilibrium for Power Transformers," *IEEE Transactions on Power Delivery,* vol. 25, pp. 2574–2581, 2010.

[99] C. Tang, X. Li, F. Yin, and J. Hao, "The performance improvement of aramid insulation paper by nano-SiO2 modification," *IEEE Transactions on Dielectrics and Electrical Insulation,* vol. 24, pp. 2400–2409, 2017.

[100] T. A. Prevost, "Thermally upgraded insulation in transformers," in *Electrical insulation conference and electrical manufacturing conference*, ed: IEEE, 2005, pp. 120–125.

[101] S. Chakravorti, D. Dey, and B. Chatterjee, "Remaining Life Analysis," in *Recent trends in the condition monitoring of transformers*, S. Chakravorti, D. Dey, and B. Chatterjee, Eds., ed London: Springer, 2013, pp. 261–275.

[102] S. Chakravorti, D. Dey, and B. Chatterjee, Eds., *Recent trends in the condition monitoring of transformers: Theory, implementation and analysis / Sivaji Chakravorti, Debangshu Dey, Biswendu Chatterjee* (Power systems, 1612-1287. London: Springer, 2013, p.^pp. Pages.

[103] C. Krause, L. Dreier, A. Fehlmann, and J. Cross, "The degree of polymerization of cellulosic insulation: Review of measuring technologies and its significance on

equipment," in *2014 IEEE Electrical Insulation Conference (EIC 2014)*, ed Piscataway, NJ: IEEE, 2014, pp. 267–271.

[104] N. Lelekakis, D. Martin, and J. Wijaya, "Ageing rate of paper insulation used in power transformers Part 2: Oil/paper system with medium and high oxygen concentration," *IEEE Transactions on Dielectrics and Electrical Insulation,* vol. 19, pp. 2009–2018, 2012.

[105] W. J. McNutt, "Insulation thermal life considerations for transformer loading guides," *IEEE Transactions on Power Delivery,* vol. 7, pp. 392–401, 1992.

[106] L. Lundgaard, W. Hansen, and S. Ingebrigtsen, "Ageing of Mineral Oil Impregnated Cellulose by Acid Catalysis," *IEEE Transactions on Dielectrics and Electrical Insulation,* vol. 15, pp. 540–546, 2008.

[107] M. Ariannik, A. A. Razi-Kazemi, and M. Lehtonen, "An approach on lifetime estimation of distribution transformers based on degree of polymerization," *Reliability Engineering & System Safety,* vol. 198, p. 106881, 2020.